

Numerical Analysis of complex dental implants behaviour using a meshless method

Francisco José Rocha Barros Castro

Supervisor:

Professor Jorge Américo Oliveira Pinto Belinha

Co-Supervisors:

Professor Renato Manuel Natal Jorge

Professor Lúcia Maria de Jesus Simas Dinis

Thesis submitted to Faculdade de Engenharia da Universidade do Porto as a
requirement to obtain the Master Degree in Mechanical Engineering

Porto, June 2017

“I’ve been impressed with the urgency of doing.
Knowing it’s not enough, we must apply.
Willing is not enough, we must do”
Leonardo da Vinci

Acknowledgements/Agradecimentos

Ao professor Jorge Belinha, o meu muito obrigado por todo o apoio incondicional ao longo deste semestre. Por toda a paciência e tempo despendido, tentando sempre ajudar-me nas mais ínfimas coisas. Pelos seus conselhos e orientação sempre cuidada a cada passo que percorria na realização da dissertação.

Aos meus pais, Paulo e Dores, por tudo o que são e que fizeram por mim. Ao meu irmão, Edu, por me chatear sempre a cabeça ao fim de semana e nas férias com assuntos que não importam a ninguém. Aos meus avós, tios, padrinhos e primos pelo interesse e apoio constante. E, também, pelos maravilhosos jantares aos sábados à noite em casa dos avós.

Ao Ribeiro e à Anita por serem os melhores amigos que alguém pode ter e que apesar da distância e do longo tempo sem os ver, tudo se mantém sempre igual apesar de tudo. Ao resto dos bandidos todos de Fafe por tornarem a vida uma alegria: Electro, Tiago, Vasco, Cris, Tiga, Miga, José Pedro, Renato, Espanhol, Miccoli, Pica, Chico Cunha.

Aos meus amigos da faculdade que me acompanharam ao longo destes cinco anos e tornaram este percurso mais fácil e divertido do que seria sem eles: Vasco, Tiago, Hugo, Telo, Edu, BigShow, Cortez, Renata, Rita, Sara, Graça, Poupas, Catarina, Marco e David. Ao meu padrinho e afilhados e resto do pessoal por quem tenho também muito carinho e amizade.

À Téé ☺.

Institutional Acknowledgments

The author truly acknowledges the work conditions provided by the Applied Mechanics Division (SMAp) of the department of mechanical engineering (DEMec) of FEUP and by the inter-institutional project “BoneSys – Bone biochemical and biomechanic integrated modeling: addressing remodeling, disease and therapy dynamics” funded by the “Laboratório Associado de Energia Transportes e Aeronáutica” (UID/EMS/50022/2013) and by the project NORTE-01-0145-FEDER-000022 – SciTech – Science and Technology for Competitive and Sustainable Industries, co-financed by Programa Operacional Regional do Norte (NORTE2020), through Fundo Europeu de Desenvolvimento Regional (FEDER).

The author truly acknowledge the provided design of the implants under patent number 10201700017985, belonging to Pietro Gobbo. Implant’s brand is “Simplified”, possessing the register number: 302012902106491.

Abstract

Nowadays, dental implants are the best way to replace missing teeth. A dental implant is a biocompatible screw that is surgically placed into the jawbone which permits to the patient to have an improved appearance, comfort, speech and self-esteem.

Due to its dimensions, the direct measuring of the geometry of teeth, implants and bone structures is a challenging task. Nevertheless, today, there are several CAD and medical image softwares capable to reproduce the computational geometry of such entities, allowing the application of discretization techniques to obtain relevant variable fields, such as displacement, strain and stress fields. Thus, nowadays, computational techniques are low-cost and effective alternatives to analyse the mechanical performance of the dental implants.

The main goal of this thesis is to perform a numerical analysis of a complex dental implant using a new advanced discretization technique, the meshless methods. A 3D analysis was performed for the first time to dental implants using one of these techniques, more specifically the Radial Point Interpolation Method (RPIM). In the RPIM, the nodal connectivity is imposed using the concept of influence domain, which radially searches around an interest point for neighbour nodes. This creates variable sized influence domains that contain the neighbour nodes of the interest node, and that are used to create the interpolation functions.

During many years, the analysis to dental implants were performed using the Finite Element Method (FEM). So, a comparison between the both methods will be studied and analyzed. It is known that the meshless methods possess some advantages relative to FEM, such as the production of smoother stress fields and a much more flexible discretization technique.

The results revealed that the differences obtained for the two numerical methods are around 10%-40%. Additionally, it was found that this difference increases with the approximation of the points near the zones where the boundary condition is applied.

Resumo

Hoje em dia, os implantes dentários são a melhor opção para substituir dentes. O implante dentário é um parafuso biocompatível que é colocado cirurgicamente no maxilar que permite ao paciente ter uma melhor aparência, conforto e autoestima.

Devido às suas dimensões, a medição direta da geometria dos dentes, implantes e estruturas ósseas é uma tarefa desafiante. No entanto, hoje, existem vários softwares CAD e de imagens médicas capazes de reproduzir a geometria computacional de tais entidades, permitindo de seguida a aplicação de técnicas de discretização para obter campos variáveis relevantes, como campos de deslocamento, tensão e deformação. Assim, hoje em dia, as técnicas computacionais são alternativas efetivas de baixo custo capazes de analisar o desempenho mecânico dos implantes dentários.

O principal objetivo da dissertação é realizar análises numéricas a um implante dentário usando um novo método de discretização, os métodos sem malha. Assim, uma análise 3D foi realizada pela primeira vez em implantes dentários usando este novo método, mais concretamente o “Radial Point Interpolation Method” (RPIM). No RPIM, a conectividade nodal é imposta usando o conceito de domínio de influência, que busca radialmente nós vizinhos em torno de um ponto de interesse. São criados domínios de influência de tamanho variável que contêm todos os vizinhos do nó de interesse, usados para a criação das funções de forma.

Durante muitos anos, a análise dos implantes foi efetuada usando o Método dos Elementos Finitos (FEM). Assim sendo, uma comparação entre estes dois métodos numéricos irá ser realizada. É sabido que os métodos sem malha, possuem algumas vantagens em relação ao FEM nomeadamente campos de tensão mais suaves e possibilitam uma discretização mais flexível.

Os resultados mostraram que as diferenças de valores obtidos entre os dois métodos estão entre os 10%-40%. Adicionalmente, foi verificado que esta diferença aumenta junto a zonas onde estão aplicadas as condições de fronteira.

Contents

1.	Introduction.....	1
1.1	Meshless Methods.....	1
1.1.1	Radial Point Interpolation Method.....	4
1.1.2	Meshless methods in biomechanics.....	4
1.2	Objectives.....	5
1.3	Document Structure.....	6
2.	Dental implants – an overview.....	7
2.1.1	Brief History.....	8
2.1.2	Description, materials and types of implants.....	9
2.1.3	Biomechanical considerations.....	10
3.	Meshless Methods.....	13
3.1	General Meshless Method Procedure.....	13
3.2	RPIM Formulation.....	15
3.2.1	Influence-domains and nodal connectivity.....	15
3.2.2	Numerical integration.....	16
3.3	Shape Functions.....	21
4.	Solid Mechanics Fundamentals.....	25
4.1	Stress components.....	25
4.2	Equilibrium equations.....	26
4.3	Components of strain.....	27
4.4	Constitutive equations.....	29
4.5	Strong form and weak formulation.....	30
4.5.1	Galerkin weak form.....	30
4.6	Discrete Systems Equations.....	34
5.	3D Model Construction.....	37
5.1	Programs.....	38
5.2	Materials.....	41

5.2.1	Nylon sleeve.....	41
5.2.2	Titanium sleeve and abutment.....	43
5.3	Loads	44
5.4	Essential boundaries conditions.....	46
6.	Numerical Analysis	47
6.1	Mechanical Case A.....	47
6.2	Mechanical Case B.....	61
6.3	Mechanical Case C	74
6.4	Mechanical Case D.....	91
6.5	Study on Distinct Materials.....	95
6.5.1	Mechanical Case C.....	96
6.5.2	Mechanical Case D.....	107
7.	Conclusions.....	121
7.1	Conclusions	121
7.2	Future works.....	122
7.3	Computacional time.....	123
8.	References.....	125

List of Figures

Figure 1: Mayan dental implant from 600 AD	8
Figure 2: Dental implant.....	9
Figure 3: a) Problem domain with the essential and natural boundaries applied. b) Regular mesh. c) Irregular mesh.....	13
Figure 4: Influence-domains with different sizes and shapes [5]	15
Figure 5: a) Fixed size circular influence-domain; b) Variable size circular influence-domain [5]	16
Figure 6: a) Quadrilateral cell background. b) Triangular cell background. c) Quadrilateral grid background [53]	17
Figure 7: a) Initial quadrilateral from the grid cell; b) Transformation of the initial quadrilateral into an isoparametric square shape and application of the 2x2 quadrature point rule; c) Return to the initial quadrilateral shape. [5]	17
Figure 8: Six independent stress components at a point in a solid viewed on the surfaces of an infinitely small cubic block [50]	26
Figure 9: 3D solid mechanics problem	31
Figure 10: Detailed scheme of the parts belonged to the dental implant on study	37
Figure 11: Images of titanium sleeve and abutment, respectively [1]	38
Figure 12: FEMAS initial presentation and GUI interface	39
Figure 13: Example of a 3D model of a complex dental implant on FEMAS and its natural and essential boundaries; Example of a stress field of the dental implant obtained with FEMAS	40
Figure 14: Schematic representation of the load cases.....	44
Figure 15: Representative scheme of the forces for torsion	45
Figure 16: Different types of essential boundaries conditions.	46
Figure 17: Interest Point for analyses on MCA.....	48
Figure 18: Principal Stress σ_{11} , Principal Stress σ_{33} and Effective Stress (Von Mises), respectively for MCA obtained with both numerical methods for distinct load angles	51

Figure 19: Principal Strain ϵ_{11} , Principal Strain ϵ_{33} and Effective Strain (Von Mises), respectively for MCA obtained with both numerical methods for distinct load angles	52
Figure 20: Interest points for analysis on MCB	61
Figure 21: Principal Stress σ_{11} , Principal Stress σ_{33} and Effective Stress (von Mises), respectively for MCB obtained with both numerical methods for distinct load angles	64
Figure 22: Principal Strain ϵ_{11} , Principal Strain ϵ_{33} and Effective Strain (von Mises), respectively for MCB obtained with both numerical methods for distinct load angles	65
Figure 23: Interest points for analysis on MCC	74
Figure 24: Principal Stress σ_{11} , Principal Stress σ_{33} and Effective Stress (Von Mises), respectively for MCC to interest points P1, P2 and P3 obtained with both numerical methods for distinct load angles	79
Figure 25: Principal Strain ϵ_{11} , Principal Strain ϵ_{33} and Effective Strain (Von Mises), respectively for MCC to interest points P1, P2 and P3 obtained with both numerical methods for distinct load angles	80
Figure 26: Principal Stress σ_{11} , Principal Stress σ_{33} and Effective Stress (Von Mises), respectively for MCC to interest points P7, P8 and P9 obtained with both numerical methods for distinct load angles	81
Figure 27: Principal Strain ϵ_{11} , Principal Strain ϵ_{33} and Effective Strain (Von Mises), respectively for MCC to interest points P7, P8 and P9 obtained with both numerical methods for distinct load angles	82
Figure 28: Line of interest point for analysis on MCD	91
Figure 29: Principal Stress σ_{11} , Principal Stress σ_{33} and Effective Stress (Von Mises), respectively for MCD obtained with both numerical methods along the interest points line.....	93
Figure 30: Principal Strain ϵ_{11} , Principal Strain ϵ_{33} and Effective Strain (Von Mises), respectively for MCD obtained with both numerical methods along the interest points line.....	94
Figure 31: Interest point for analysis on nylon sleeve	95
Figure 32: Effective Strain Von Mises trend, using different types of nylons.....	106

Figure 33: Principal Stress σ_{11} , Principal Stress σ_{33} and Effective Stress (Von Mises), respectively for MCD obtained with both numerical methods along the interest points line for the different nylon materials. 112

Figure 34: Principal Strain ϵ_{11} , Principal Strain ϵ_{33} and Effective Strain (Von Mises), respectively for MCD obtained with both numerical methods along the interest points line for the different nylon materials 113

Figure 35: Computational time for both phase (pre-process and process) for each analysis..... 123

List of Tables

Table 1: Integration points and correspondent weights for quadrilateral isoparametric cells	18
Table 2: Integration points and correspondent weights for triangular isoparametric cells	19
Table 3: Phases description [53].....	41
Table 4: Mechanical properties of the several polymers for the nylon sleeve used on the analysis.....	43
Table 5: Mechanical properties of the titanium used on the analysis	43
Table 6: Force angles and consequent Cartesian components (N).....	44
Table 7: Obtained values for point 1 with both numerical methods, with respect to the angle of the applied load.....	49
Table 8: Obtained values for point 2 with both numerical methods, with respect to the angle of the applied load.....	49
Table 9: Obtained values for point 3 with both numerical methods, with respect to the angle of the applied load.....	50
Table 10: Stress distribution map on abutment for MCA. Effective stress (von Mises), principal stress σ_{11} and principal stress σ_{33} , respectively. [MPa]	54
Table 11: Strain distribution map on abutment for MCA. Effective strain (von Mises), principal strain ϵ_{11} and principal strain ϵ_{33} , respectively.....	55
Table 12: Stress distribution map on nylon sleeve for MCA. Effective stress (von Mises), principal stress σ_{11} and principal stress σ_{33} , respectively. [MPa]	56
Table 13: Strain distribution map on nylon sleeve for MCA. Effective strain (von Mises), principal strain ϵ_{11} and principal strain ϵ_{33} , respectively.....	57
Table 14: Stress distribution map on titanium sleeve for MCA. Effective stress (von Mises), principal stress σ_{11} and principal stress σ_{33} , respectively. [MPa].....	58
Table 15: Strain distribution map on titanium sleeve for MCA. Effective strain (von Mises), principal strain ϵ_{11} and principal strain ϵ_{33} , respectively	59
Table 16: Obtained values for point 4 with both numerical methods, with respect to the angle of the applied load.....	62

Table 17: Obtained values for point 5 with both numerical methods, with respect to the angle of the applied load.....	62
Table 18: Obtained values for point 6 with both numerical methods, with respect to the angle of the applied load.....	63
Table 19: Stress distribution map on abutment for MCB. Effective stress (Von Mises), principal stress σ_{11} and principal stress σ_{33} , respectively. [MPa]	67
Table 20: Strain distribution map on abutment for MCB. Effective strain (Von Mises), principal strain ϵ_{11} and principal strain ϵ_{33} , respectively.....	68
Table 21: Stress distribution map on nylon sleeve for MCB. Effective stress (Von Mises), principal stress σ_{11} and principal stress σ_{33} , respectively. [MPa]	69
Table 22: Strain distribution map on nylon sleeve for MCB. Effective strain (Von Mises), principal strain ϵ_{11} and principal strain ϵ_{33} , respectively.....	70
Table 23: Stress distribution map on titanium sleeve for MCB. Effective stress (Von Mises), principal stress σ_{11} and principal stress σ_{33} , respectively. [MPa].....	71
Table 24: Strain distribution map on titanium sleeve for MCB. Effective strain (Von Mises), principal strain ϵ_{11} and principal strain ϵ_{33} , respectively.....	72
Table 25: Obtained values for point 1 with both numerical methods, with respect to the angle of the applied load.....	75
Table 26: Obtained values for point 2 with both numerical methods, with respect to the angle of the applied load.....	75
Table 27: Obtained values for point 3 with both numerical methods, with respect to the angle of the applied load.....	76
Table 28: Obtained values for point 7 with both numerical methods, with respect to the angle of the applied load.....	76
Table 29: Obtained values for point 8 with both numerical methods, with respect to the angle of the applied load.....	77
Table 30: Obtained values for point 9 with both numerical methods, with respect to the angle of the applied load.....	77
Table 31: Stress distribution map on abutment for MCC. Effective stress (von Mises), principal stress σ_{11} and principal stress σ_{33} , respectively. [MPa]	84
Table 32: Strain distribution map on abutment for MCC. Effective strain (von Mises), principal strain ϵ_{11} and principal strain ϵ_{33} , respectively.....	85

Table 33: Stress distribution map on nylon sleeve for MCC. Effective stress (von Mises), principal stress σ_{11} and principal stress σ_{33} , respectively. [MPa].....	86
Table 34: Strain distribution map on nylon sleeve for MCC. Effective strain (Von Mises), principal strain ϵ_{11} and principal strain ϵ_{33} , respectively.....	87
Table 35: Stress distribution map on titanium sleeve for MCC. Effective stress (von Mises), principal stress σ_{11} and principal stress σ_{33} , respectively. [MPa].....	88
Table 36: Strain distribution map on titanium sleeve for MCC. Effective strain (Von Mises), principal strain ϵ_{11} and principal strain ϵ_{33} , respectively.....	89
Table 37: Obtained local values for the MMD at the interest points line for distinct nylon materials	92
Table 38: Obtained local values for the MMC at point 1 for distinct nylon materials.	96
Table 39: Obtained local values for the MMC at point 2 for distinct nylon materials.	97
Table 40: Obtained local values for the MMC at point 3 for distinct nylon materials.	97
Table 41: Obtained local values for the MMC at point 7 for distinct nylon materials.	97
Table 42: Obtained local values for the MMC at point 8 for distinct nylon materials.	98
Table 43: Obtained local values for the MMC at point 9 for distinct nylon materials.	98
Table 44: Obtained local values for the MMC at point 10 for distinct nylon materials	98
Table 45: Stress distribution map on abutment for MCC regarding the distinct nylon materials. Effective stress (Von Mises), principal stress σ_{11} and principal stress σ_{33} , respectively. [MPa].....	100
Table 46: Strain distribution map on abutment for MCC regarding the distinct nylon materials. Effective strain (Von Mises), principal strain ϵ_{11} and principal strain ϵ_{33} , respectively.....	101
Table 47: Stress distribution map on nylon sleeve for MCC regarding the distinct nylon materials. Effective stress (Von Mises), principal stress σ_{11} and principal stress σ_{33} , respectively. [MPa].....	102

Table 48: Strain distribution map on nylon sleeve for MCC regarding the distinct nylon materials. Effective strain (Von Mises), principal strain ϵ_{11} and principal strain ϵ_{33} , respectively.....	103
Table 49: Stress distribution map on titanium sleeve for MCC regarding the distinct nylon materials. Effective stress (Von Mises), principal stress σ_{11} and principal stress σ_{33} , respectively. [MPa].....	104
Table 50: Strain distribution map on titanium sleeve for MCC regarding the distinct nylon materials. Effective strain (Von Mises), principal strain ϵ_{11} and principal strain ϵ_{33} , respectively.....	105
Table 51: Obtained local values for the MCD at the interest points line for nylon GV5.....	108
Table 52: Obtained local values for the MCD at the interest points line for nylon LV3H.....	109
Table 53: Obtained local values for the MCD at the interest points line for nylon LKN	110
Table 54: Obtained local values for the MMD at point 10 for distinct nylon materials	114
Table 55: Stress distribution map on abutment for MCD regarding the distinct nylon materials. Effective stress (Von Mises), principal stress σ_{11} and principal stress σ_{33} , respectively. [MPa].....	115
Table 56: Strain distribution map on abutment for MCD regarding the distinct nylon materials. Effective strain (Von Mises), principal strain ϵ_{11} and principal strain ϵ_{33} , respectively.....	116
Table 57: Stress distribution map on nylon sleeve for MCD regarding the distinct nylon materials. Effective stress (Von Mises), principal stress σ_{11} and principal stress σ_{33} , respectively. [MPa].....	117
Table 58: Strain distribution map on nylon sleeve for MCD regarding the distinct nylon materials. Effective strain (Von Mises), principal strain ϵ_{11} and principal strain ϵ_{33} , respectively.....	118
Table 59: Stress distribution map on titanium sleeve for MCD regarding the distinct nylon materials. Effective stress (Von Mises), principal stress σ_{11} and principal stress σ_{33} , respectively. [MPa].....	119

Table 60: Strain distribution map on titanium sleeve for MCD regarding the distinct nylon materials. Effective strain (Von Mises), principal strain ϵ_{11} and principal strain ϵ_{33} , respectively..... 120

1. Introduction

Nowadays, dental implants are the best way to replace missing teeth. A dental implant is a biocompatible screw that is surgically placed into the jawbone, permitting to the patient to have an improved appearance, comfort, speech and self-esteem.

Due to its importance, studying it has been one of the aims for many researchers. Because of the geometry, dimensions, and position, the direct measuring of the teeth-implant-bone displacements, strains and stresses is a very difficult task. So, the classical methods for measuring the state of stress in a structure, such as the use of strain gauges is almost impossible [2]. Therefore, discretization techniques are adequate to predict the required variable fields. Currently, the most popular numerical technique used for the analysis for dental implant analysis is the Finite Element Method. Recently, a new class of numerical methods was created and developed to surpass some disadvantages of the FEM, the meshless methods [3].

1.1 Meshless Methods

Numerical simulation plays a fundamental role in many branches of science and biomechanics is one of them [4]. It is possible to define and classify a numerical method by three fundamental modules: the field approximation function, the used formulation and the integration [5]. On the other hand, there are also three phases in computational biomechanics: the modulation, the simulation and the analysis. It is necessary to use a discretization technique to perform them. This process is naturally recurrent and strongly depends on the selected numerical technology. Nowadays, there are many numerical methods available and capable to handle the mentioned phases of the bioengineering design before mentioned. Although, the different numerical methods described in the literature present some differences, which leads to distinct numerical performances [6].

The **Finite Element Method** (FEM) was firstly developed, in the 1960's, to solve structural problems in the aerospace industry. Since then, and with the development of more efficient ways to solve complex structural analysis problems, the FEM has become the most popular and successful engineering computational method and the most useful analysis tool [7]. It is a powerful method for computing the displacements, stresses and strains in a structure under a set of loads [8].

The FEM offers an approximate solution to complex continuum systems, assuming a discretized numerical model with finite degrees of freedom. The approximated solution obtained using the finite element formulation is mesh dependent. The accuracy of the final solution relies strongly on the mesh quality and on the mesh refinement. Denser and well balanced finite element meshes generally lead to more accurate results. However, the computational cost of the analysis increases with the number of elements discretizing the analysis domain, which is a drawback in biomechanics [3]. Moreover, there are still more limitations, such as the inaccuracy due to highly distorted meshes in large deformations problems. Therefore, re-meshing can be a solution to this problem, but the time consumption and the high computational costs could be dissuasive factors. On the other hand, for 3D problems the cost of creating good quality meshes can be high.

Meshless methods were created recently to be an alternative to FEM and to surpass some disadvantages and limitations of it. These methods have evolved rapidly, solving many of their initial problems such as accuracy, imposition of essential boundary conditions, numerical integration and stability. In the meshless methods, there are no mesh or elements. In opposition to the FEM (where the elements cannot overlap), in meshless methods the nodal connectivity is imposed by the overlap of the "influence domains" [3]. In these methods, the nodes can be randomly distributed and the field functions are approximated within an influence domain rather than an element. The influence domain is an area or volume that can be concentric with an interesting point (an integration point if it is used the Gauss-Legendre Integration Method).

Meshless methods can be divided in two groups, depending on how the numerical integration is done. The first ones, the "truly" meshless methods, only requires the information regarding the nodal distribution [3] and the second ones,

the “not truly” meshless methods, use a background integration mesh (with Gauss-Legendre integration points) to perform the numerical integration, which eliminates the mesh-free characteristics of these methods [9].

Meshless methods first appeared in 1977, with the introduction of the Smooth Particle Hydrodynamics Method (SPH) [10]. Based on a strong form and being one of the oldest meshless methods in existence, was originally developed due to the desire to simulate the formation of binary star systems. This method was only extended to solid mechanics in 1990 [11]. Although, the first global weak form based on meshless methods was only presented in 1994 (the Element Free Galerkin Method (EFGM)) [12], which remains as one of the most popular meshless methods until these days. The EFGM was developed using the Diffuse Element Method (DEM) [13] as base, which by its turn was the first meshless method using the Moving Least Square (MLS) [14, 15] approximants in the construction of the shape functions. Other important methods that appeared in the same period were the Reproducing Kernel Particle Method (RKPM) [16], which was based on the SHP, and the Meshless Local Petrov-Galerkin (MLPG) [17, 18]. However, all the previously mentioned methods use the approximation shape functions, which means they lack the Kronecker delta function property, which hinders the imposition of the essential and natural boundary conditions.

This was solved with the recent development of several interpolation meshless methods. In 2001, the Point Interpolation Method (PIM) was created [19, 20]. A year later, to simplify the computation of the shape functions, and to eliminate some singularities that occurred in the PIM, the Radial Point Interpolation Method (RPIM) [21, 22] was developed. The RPIM uses radial basis functions (RBF) combined with polynomial basis functions to construct the shape functions used in the integration of the partial differential equations. The Natural Element Method (NEM) is the meshless method that use the Sibson interpolation functions. More recently, combining the NEM and the RPIM, the Natural Neighbour Radial Point Interpolation Method (NNRPIM) was developed [23].

1.1.1 Radial Point Interpolation Method

The RPIM was developed from the PIM [19, 20]. The PIM uses the influence-domain concept to establish the nodal connectivity, instead of the global domain of the problem, which improves nodal connectivity. Furthermore, its shape functions possess the Kronecker delta property, which means that they pass through every single node, making them interpolation shape functions, which fixes the issue of the essential and natural imposition. Another advantage is that its shape functions are much simpler and easier to obtain, which leads to higher computer efficiency. However, the PIM only employed polynomials as its basis functions and because of that some singularities could occur, as for example, the perfect alignment of the nodes would produce solutions in the shape function construction process which causes too many numerical problems [21, 22].

In 2002, a new method was proposed: The Radial Point Interpolation Method (RPIM) [21, 22]. For stabilizing the method, the Radial Basis Function (RBF) was combined with the polynomial basis function. The addition of RBF removed the issue of possible singularities with meshless methods based on polynomial basis functions alone. Moreover, since the RPIM uses the concept of “influence-domain”, it creates sparse and banded stiffness matrices, which are more adequate to complex geometries problems. Therefore, due to its convergence rate and accuracy, the RPIM is still used nowadays.

1.1.2 Meshless methods in biomechanics

Meshless methods possess many advantages in comparison with Finite Element Methods, such as the re-meshing efficiency, which is good to deal with large deformations of soft materials as muscles, internal organs and skin. Another application in which meshless methods show superior performance is the simulation of biofluid flow, such as hemodynamics, the swallow or the respiration. Moreover, the smoothness and the accuracy of the solution fields (displacements, stresses and strains) obtained with meshless methods are very useful to predict the remodelling process of biological tissues and the rupture or damage of such

biomaterials. Also, recent works show that combining medical imaging techniques (CAT and MRI) with meshless methods is much more viable than using FEM [24-26].

1.1.2.1 Meshless methods and dental implants

A few studies [3, 27] have been performed with meshless methods with dental implants and in both cases it was used a 2D geometry for the analyses. In the author best knowledge, this work is the first one that simulates 3D implants using meshless methods.

In general, mesh generation for a three-dimensional (3D) problem is far from being completely automatized and developed with finite element methods for living organs. Mesh generation usually relies in a large amount of user time and when the modelled organ suffers large deformations, a frequent re-meshing strategy is needed to avoid numerical errors that can break out the simulation [28]. Subsequently, meshless methods are the best option to deal with 3D problems for biomechanics analyses due to all the advantages mentioned before.

1.2 Objectives

The main goals of this project are:

- Perform an elasto-static analysis of a dental implant, applying several concentrated loadings, varying the angles of this loadings and using two numerical methods: FEM and RPIM;
- Draw further comparisons between the results obtained with FEM and RPIM;
- Extend the use of meshless methods to 3D dental implants for the first time;
- Understand the mechanical behaviour of all the parts that constitute the dental implant on study.

1.3 Document Structure

Seven major chapters compose this thesis: Introduction, Dental Implants, Meshless Methods, Solid Mechanics Fundamentals, 3D Model Construction, Numerical Analysis and Conclusions.

In the first chapter, **Introduction**, a general overview of the meshless method is presented and the main goals of this work are proposed.

In chapter 2, **Dental Implants**, a description about its history, constitution, types and some biomechanical considerations of dental implants are presented.

In chapter3, **Meshless Methods**, a detailed description of the meshless method used in this work, the RPIM, is presented and its formulation.

In chapter 4, **Solid Mechanics Fundamentals**, the concepts of solid mechanics are developed. The weak formulation is presented and the discrete system equations are obtained.

In chapter 5, **3D Model Construction**, it is described the program used to run the analysis and all the materials, natural and essential boundaries used for the several cases studied.

In chapter 6, **Numerical Analysis**, several analyses to the implants are performed. All the results are presented, following some discussions regarding to these analyses.

In chapter 7, **Conclusions**, the main conclusions of this work are done and finally some suggestions for future works are presented.

2. Dental implants – an overview

Dental implants are considered a good solution for the lack of dentition, being considered the best alternative after natural teeth [29]. They are an efficient therapy usually prescribed to partial edentulous or total edentulous people [5], however, implants are the most expensive method of tooth replacement [30].

Despite of being used for many decades, this therapy hasn't always enjoyed a favourable reputation. This situation has changed dramatically with the development of endosseous osseointegrated dental implants [31].

The main purpose of tooth replacement with dental implants is to restore adequate function and esthetics without affecting adjacent hard and/or soft tissue structures.

One of the most important factors in determining implant success is proper treatment planning. In the past, periapical radiographs along with panoramic images were used as the sole determinants of implant diagnosis and treatment planning. With the advancement of radiographic technology, Computed Tomography (CT), as well as Cone-Beam Computed Tomography (CBCT) are increasingly considered essential for optimal implant placement, especially in the case of complex reconstructions [32].

In general, implant treatment is highly reliable and safe. The benefits of such treatment are:

- Cost effective and long lasting solution to tooth loss;
- Significant benefits in improving quality of life and well-being of patients;
- Prevention of disuse atrophy and deterioration of the jaw bone support.

On the other hand, complications with dental implants can also occur and failures can happen. Long-term success and prognosis often depends on successful management of variety of risks factors both biological such as gingival recession or inflammation or mechanical such as screw and restoration fractures [7, 33].

Success rates for partially dentate patients treated with implants are around 90% over 10-15 years [30,33,34].

2.1.1 Brief History

Development of an ideal substitute for missing teeth has been one of the long term aims of dentistry since many years ago [7].

Dental implants history goes back to centuries ago. Since the beginning of mankind, humans have used dental implants in one form or another to replace the missing teeth, examples of it are the ancient cultures of the world (Egypt, Honduras, China, Turkey, among others). In approximately 2500 BC, the ancient Egyptians tried to stabilize teeth that were periodontally involved with the use of ligature wire made of gold [35, 36].

The Mayan civilization is one of the many examples that have used dental implants. About 600 AD, archaeologists found a part of a mandible of Mayan origin which had three tooth-shaped pieces of shell placed into the sockets of three missing lower incisor teeth [33].



Figure 1: Mayan dental implant from 600 AD

More recently, an important advance was the introduction of the concept of **osseointegration** by Branemark in 1952 who defined it as “a direct structural functional connection between ordered living bone and the surface of a load-carrying implant”. The Branemark technique utilized biocompatible titanium-alloy implants that were automatically inserted into the alveolar process. This concept grew in the 1980’s which brought a defining moment in the clinical field of implants [35, 37].

As time marches on, the implant's materials, forms and surface coatings have been improved and restructured to permit the consumer the very best in tooth replacement choices for their present and future needs [35].

The replacement for lost teeth by dental implants became a common technique to this esthetical and healthy problem, being nowadays considered the best alternative after natural teeth.

2.1.2 Description, materials and types of implants

Therefore, the implants consist in tiny metal posts which are inserted into the jawbone where teeth are missing [2].

Modern implants consist of an osseous part that interacts with the bone, a transmucosal component that interacts with the mucosa and then the restoration, which can be a crown, a bridge abutment, or anchors for dentures.

In the Figure 2, it is represented the constitution of a dental implant:

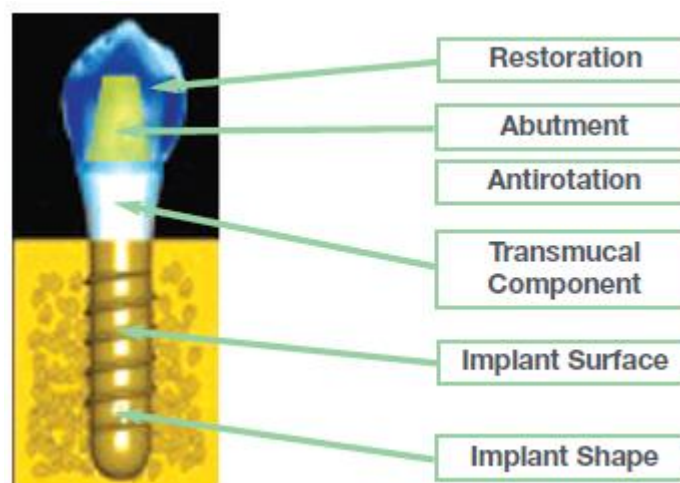


Figure 2: Dental implant

Dental implants are in general made of commercially pure titanium, since this **material** promotes a stable and functional connection between the bone and the surface of the implant [38]. Another possible materials can be titanium alloys or ceramic materials such as zirconium dioxide or aluminium oxide [39].

During the last two decades, many modifications have been developed to improve the long-term success of implants. Nowadays, there are available in the market around 1300 different **types of dental** implants, in many different materials, shapes, sizes, lengths and with different surface characteristics or coatings.

Most of the implants are endosteal (i.e. placed with alveolar bone) in design. Endosteal implants are subdivided into several different types characterised by their geometry, shape, surfaces, function and materials [33].

Dental restorations can be fixed or removable (removable dental prosthesis - RDP). The removable restoration can be partial (removable partial denture - RPD) or complete (complete denture - CD) [40].

2.1.3 Biomechanical considerations

The wide range of implant applications, as well the continuous evolution of clinical indications and protocols in prosthetic dentistry make the stress analysis of the bone-implant structural system an actual, open and important issue. Controlling the biomechanical factors is possible to prevent mechanical complications, which includes fracture of screws, components or veneering materials [41, 42].

In order to achieve optimal biomechanical implant design, the following main objectives should be attained:

- To minimize stress concentration at the bone-implant interface;
- To improve primary and secondary implant stability within the bone;
- To reduce and distribute occlusal forces transmitted to the bone-implant interface through optimization of implant design and surface characteristics.

2.1.3.1 Bone-implant interface

The placement of implants is limited by the availability (quantity) and density of alveolar bone (cortical and trabecular) [29, 30]. If there is not enough bone, more bone can be added with a procedure called “bone augmentation”. Nonetheless, natural teeth and supporting tissues near the place where implant will be, must be in good condition [43].

Mechanically, the **bone** is assumed to be isotropic, linear and a homogenous material. The ratio between trabecular and cortical bone thickness is around 10. It is recognized that cortical bone has better load bearing capabilities than trabecular bone.

However, the application of dental implants in the anterior part of the mandible remains a challenging task. This is because massive atrophic changes often occur after teeth removal and due to aging, which results in significant reduction of the critical and horizontal dimensions of the mandible as well as in the loss of bone density. The level of atrophy is classified based on the size changes. Different ways to classify the atrophy are based on the absolute bone volume index (ABV), which is a ratio of the trabecular bone volume to total bone volume. ABV ratio in the healthy mandible is $50.2 \pm 11.8\%$. It decreases with age to 30%-50% in the male population and to 22%-30% in the female population [44].

Generally, the stresses generated by the vertical occlusal forces are concentrated in the neck of the implant and in the surrounding cortical bone and the stresses in the cortical bone are bigger than in the trabecular bone [41, 44].

2.1.3.2 Primary and secondary implant stability

There are two types of stability: primary and secondary.

Firstly, **primary stability** is the absence or the high resistance to micromovements, being an important factor for osseointegration. In fact, the dental micromovements must be less than $150\mu\text{m}$ to prevent implant failure. The most relevant reasons, which influence the primary stability, are surface properties; surgical techniques implant design or bone quality. [29, 38]

The **secondary stability** is associated to bone generation and remodeling, despite of bone presenting an adaptive behavior due to loading stimulus that consists in sequences of bone formation and resorption.

2.1.3.3 Dental design and surface characteristics

A **threaded** geometry provides a reduction of the stresses in the implant, the zone with the highest compressive stresses is located at the neck of the implant and not at the root [29].

Numerical studies showed that the effect of **diameter** and **length** of the implants has an influence on stress distribution at the bone-implant interface. Increasing the implant diameter promotes a reduction in the normal and shear stresses along the bone-implant interface, promoting a better distribution of loads to the tissue. In other words, the increase of the lateral area and the implant section reduces the stresses generated in the cortical bone, stresses arising from compressive forces, tensile, bending and torsion [38].

The **veneering material** does not influence stress distribution in the supporting tissues of the single-implant-supported prosthesis. Increasing the implant diameter is more important than the veneering material of the crown for distribution of occlusal loads to the supporting bone. Porcelain is widely indicated for occlusal veneering and presents excellent esthetics. It is an example of a veneering material for a 100% osseointegrated implant since the rigidity of this material do not influence the results. However, the higher resistance of the porcelain (higher Young's modulus) dictates an accurate occlusal adjustment to avoid premature overload on the implants. Acrylic resin seems to be more efficient than porcelain at reducing impact forces due to its lower Young's modulus (the more resilient the material, the higher the stress distribution). Finally, the influence of the veneering material on stress distribution is important, considering that peri-implant bone performance depends on the magnitude and concentration of stress transferred to the implants [41].

3. Meshless Methods

This work was developed using one of the most recent meshless method: the RPIM. After the previous brief description of the general meshless method procedure, in this chapter this method will be presented and carefully explained. The chapter ends with the presentation of the RPI shape functions.

3.1 General Meshless Method Procedure

The RPIM, as almost all meshless methods, presents a standard procedure. Firstly, the geometry of the problem is studied and the solid domain and contour is established, then it is possible to identify both the essential and natural boundaries applied, as seen in Figure 3a. Afterwards, as it is shown in Figure 3b and Figure 3c, the problem domain and boundary is numerically discretized by a nodal set following a regular or irregular distribution [5].

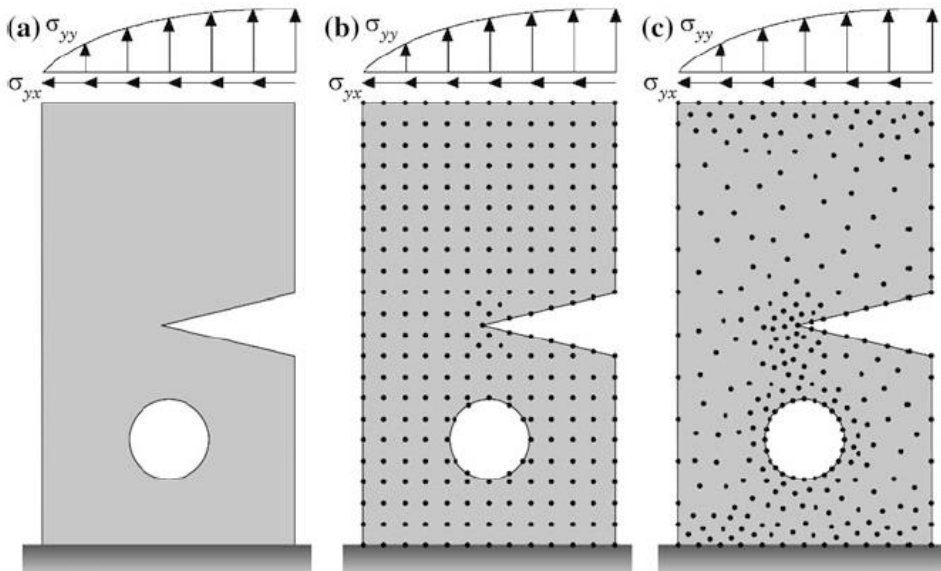


Figure 3: a) Problem domain with the essential and natural boundaries applied. b) Regular mesh. c) Irregular mesh

As Figure 3c shows, the nodal density of the discretization has a direct effect on the numerical analysis outcome. A dense nodal distribution leads generally to more accurate results, however the computational cost grows with the increase of the total number of nodes. Interestingly, the irregular discretization presents a lower accuracy. On the other hand, locations with predictable stress concentrations, such as: domain discontinuities, convex boundaries, crack tips (as shown in the previous figure), essential boundaries, and natural boundaries should have a higher local nodal density. The method to have both regular mesh and higher nodal density is to add extra nodes. These extra nodes will be added only on those specific locals before mentioned, while maintaining a regular mesh on the rest of the problem domain. This procedure allows to maintain the computational cost at acceptable values.

Afterwards, a background integration mesh is created, which can be nodal dependent or nodal independent, the later having a higher accuracy. It's necessary to implement a stabilization method on nodal dependent meshes, to reach better results, although this increases the computational costs. Meaning that the only information required by methods that use this integration scheme is the spatial location of the nodes, which makes the methods, truly meshless methods. The integration mesh can have the size of the problem domain or even a big one, without affecting too much the results.

With the nodal distribution defined and the integration mesh constructed, it is possible to obtain the nodal connectivity. While in the FEM this is done using a predefined finite element mesh, in which the nodes belonging to the same element interact directly between themselves and the boundary nodes interact with boundary nodes of nearby elements, in meshless methods there are no elements, thus, the connectivity can be assured by the overlapping of influence-domains.

Then, it is possible to obtain the field variables under study by using either approximation or interpolation shape functions. The shape functions used in this work are interpolation shape functions combining the Radial Basis Functions (RBF) with polynomial basis functions.

3.2 RPIM Formulation

3.2.1 Influence-domains and nodal connectivity

After the initial nodal discretization of the problem domain, it is needed to impose the nodal connectivity between all nodes.

Therefore, to find the nodal connectivity it is necessary to overlap the influence-domain of each node. The influence-domains are obtained through a process in which, firstly, it is settled an area (2D) or a volume (3D). Then, is it necessary to look for a specified number of nodes inside the previously established zone. In the Figure 4, we can observe that there are influence-domains with different sizes and shapes.

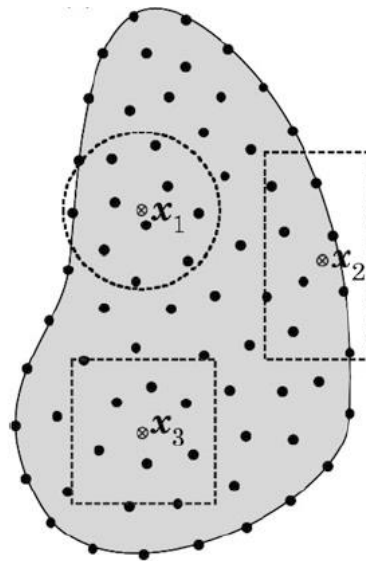


Figure 4: Influence-domains with different sizes and shapes [5]

It is important to mention that fixed and regular shaped influence-domains leads to lower accuracy results in the numerical analysis. So, to maintain a constant degree of connectivity along the solid domain, variable influence-domains are a better solution.

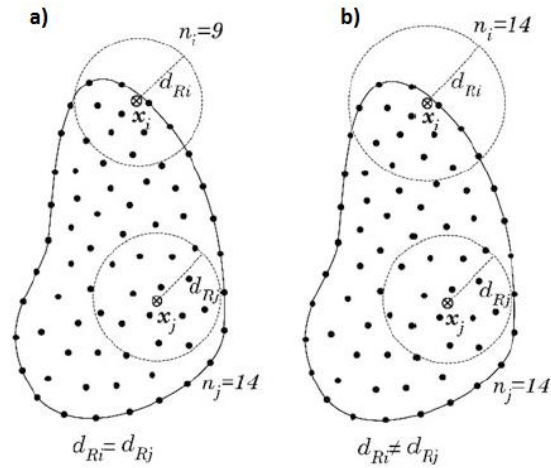


Figure 5: a) Fixed size circular influence-domain; b) Variable size circular influence-domain [5]

By using variable sized influence domains, it is possible to assure that every node's influence-domain contains the same number of nodes, allowing the construction of shape functions with the same degree of complexity. Regardless the used meshless technique, it is recommended using between $n = [9,16]$ nodes for 2D problems and $n = [27,70]$ nodes for 3D problems, according to the literature [12, 17, 19, 21]. The number of nodes inside the influence-domain does not depend on the density of the nodal discretizations and once selected, the value is valid for all domain discretizations within the same analysis.

3.2.2 Numerical integration

In the RPIM, the differential equations of the Galerkin weak form are integrated using the Gauss-Legendre quadrature. To do this, first a background mesh must be created. This background mesh can be composed of the cells created by connecting the nodes discretizing the problem domain. In the case presented in Figure 6c, the integration points outside the problem domain should be eliminated from the computation.

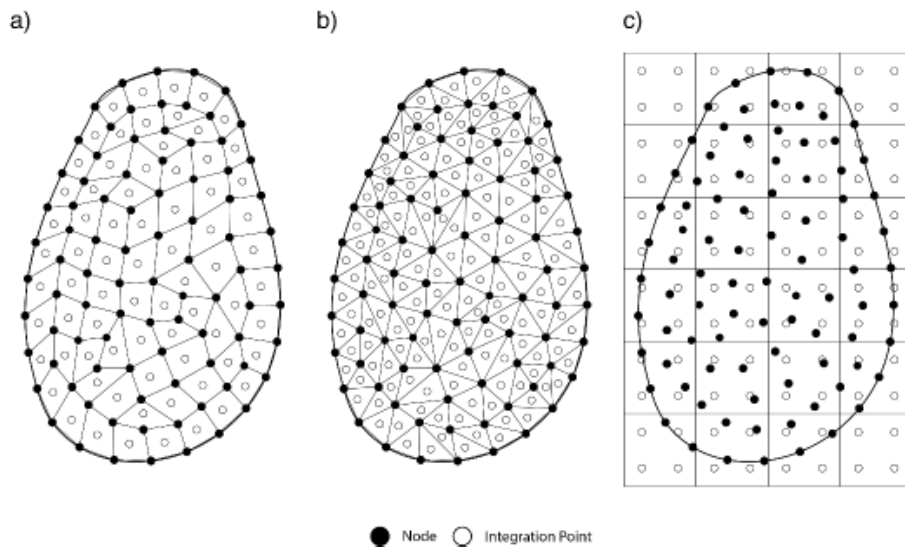


Figure 6: a) Quadrilateral cell background. b) Triangular cell background. c) Quadrilateral grid background [53]

The cells of the background mesh can be triangular or quadrilateral as seen in the Figure 6a and in the Figure 6b, respectively. Inside each one, it is possible to distribute integration points.

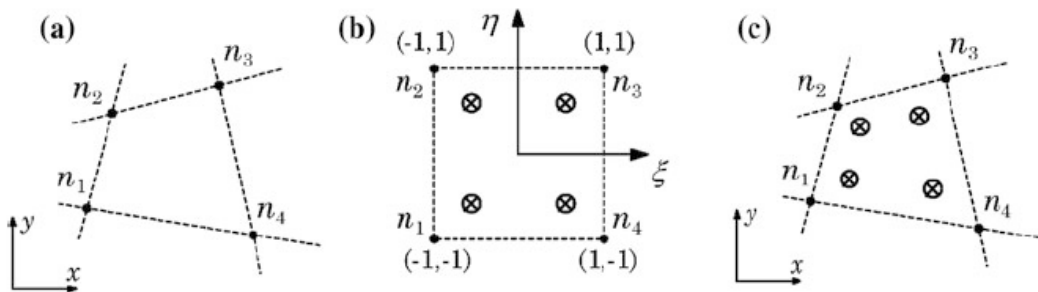


Figure 7: a) Initial quadrilateral from the grid cell; b) Transformation of the initial quadrilateral into an isoparametric square shape and application of the 2x2 quadrature point rule; c) Return to the initial quadrilateral shape. [5]

Next, in the Table 1 and in the Table 2, it is presented the location and weights of the isoparametric integration points for quadrilateral and triangular elements background meshes.

Table 1: Integration points and correspondent weights for quadrilateral isoparametric cells

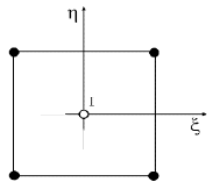
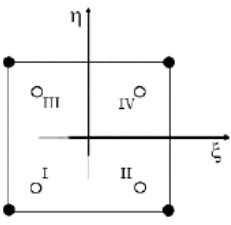
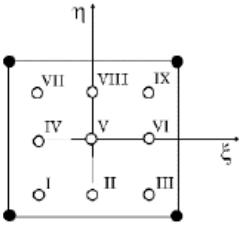
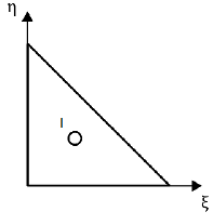
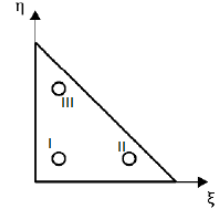
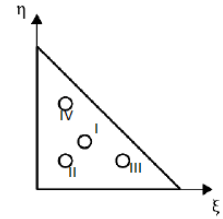
Gauss-Legendre Points	ξ	η	Weight	
I	0	0	4	
I	$-\frac{1}{\sqrt{3}}$	$-\frac{1}{\sqrt{3}}$	1	
II	$+\frac{1}{\sqrt{3}}$	$-\frac{1}{\sqrt{3}}$	1	
III	$-\frac{1}{\sqrt{3}}$	$+\frac{1}{\sqrt{3}}$	1	
IV	$+\frac{1}{\sqrt{3}}$	$+\frac{1}{\sqrt{3}}$	1	
I	$-\sqrt{\frac{3}{5}}$	$-\sqrt{\frac{3}{5}}$	$\frac{25}{81}$	
II	0	$-\sqrt{\frac{3}{5}}$	$\frac{40}{81}$	
III	$+\sqrt{\frac{3}{5}}$	$-\sqrt{\frac{3}{5}}$	$\frac{25}{81}$	
IV	$-\sqrt{\frac{3}{5}}$	0	$\frac{40}{81}$	
V	0	0	$\frac{25}{81}$	
VI	$+\sqrt{\frac{3}{5}}$	0	$\frac{40}{81}$	
VII	$-\sqrt{\frac{3}{5}}$	$+\sqrt{\frac{3}{5}}$	$\frac{25}{81}$	
VIII	0	$+\sqrt{\frac{3}{5}}$	$\frac{40}{81}$	
IX	$+\sqrt{\frac{3}{5}}$	$+\sqrt{\frac{3}{5}}$	$\frac{25}{81}$	

Table 2: Integration points and correspondent weights for triangular isoparametric cells

Gauss-Legendre Points	ξ	η	Weight	
I	$\frac{1}{3}$	$\frac{1}{3}$	$\frac{1}{2}$	
I	$\frac{1}{6}$	$\frac{1}{6}$	$\frac{1}{6}$	
II	$\frac{2}{3}$	$\frac{1}{6}$	$\frac{1}{6}$	
III	$\frac{1}{6}$	$\frac{2}{3}$	$\frac{1}{6}$	
I	$\frac{1}{3}$	$\frac{1}{3}$	$-\frac{27}{96}$	
II	$\frac{1}{5}$	$\frac{1}{5}$	$\frac{25}{96}$	
III	$\frac{3}{5}$	$\frac{1}{5}$	$\frac{25}{96}$	
IV	$\frac{1}{5}$	$\frac{3}{5}$	$\frac{25}{96}$	

After the distribution of the integration points in the isoparametric shape, the Cartesian coordinate's points are obtained using known isoparametric interpolation functions.

$$x = \sum_{i=1}^m N_i(\xi, \eta) \cdot x_i \quad (1)$$

$$y = \sum_{i=1}^m N_i(\xi, \eta) \cdot y_i \quad (2)$$

Where $N_i(\xi, \eta)$ is the isoparametric shape function, m is the number of nodes defining the cell and x_i and y_i the Cartesian coordinates of the node i .

For quadrilaterals,

$$\begin{aligned}
 N_1(\xi, \eta) &= \frac{1}{4}(1 - \xi)(1 - \eta) \\
 N_2(\xi, \eta) &= \frac{1}{4}(1 - \xi)(1 + \eta) \\
 N_3(\xi, \eta) &= \frac{1}{4}(1 + \xi)(1 + \eta) \\
 N_4(\xi, \eta) &= \frac{1}{4}(1 + \xi)(1 - \eta)
 \end{aligned} \tag{3}$$

For triangles,

$$\begin{aligned}
 N_1(\xi, \eta) &= 1 - \xi - \eta \\
 N_2(\xi, \eta) &= \eta \\
 N_3(\xi, \eta) &= \xi
 \end{aligned} \tag{4}$$

The integration weight is obtained by multiplying the isoparametric weight of the integration point with the inverse of the Jacobian matrix determinant.

$$[J] = \begin{bmatrix} \frac{\partial x}{\partial \xi} & \frac{\partial x}{\partial \eta} \\ \frac{\partial y}{\partial \xi} & \frac{\partial y}{\partial \eta} \end{bmatrix} \tag{5}$$

The differential equation integration is,

$$\int_{-1}^1 \int_{-1}^1 f(\mathbf{x}) \, dx \, dy = \sum_{i=1}^m \sum_{j=1}^n \omega_i \omega_j f(\mathbf{x}) \tag{6}$$

In which ω_i is the weight of the integration point \mathbf{x} .

3.3 Shape Functions

In meshless methods, the problem domain is not discretized with elements. It is discretized in a nodal mesh, which can follow a regular or irregular distribution. The absence of elements requires the application of an interpolation or approximation technique, based on a moving local nodal domain, to permit the construction of the meshless shape functions for the approximation of the field variable [5].

The shape functions used for the RPIM are based on a combination of radial basis functions with polynomial functions. A meshless method using only polynomial functions possess possible singularities and the combination of other kind of basis functions (besides the polynomial basis function) eliminates this issue [4, 21]. The most significant advantage of these shape functions is that they possess the Kronecker delta property, so they are interpolating shape functions.

Considering a function $u(\mathbf{x}_I)$, defined in a domain discretized with arbitrary distributed nodes. Consider now an interest point \mathbf{x}_I belonging to the discretized domain. The mentioned interest point \mathbf{x}_I possesses n nodes inside its influence domain. It is assumed that only the nodes inside the influence domain of the interest point \mathbf{x}_I have effect on the interpolated value $u(\mathbf{x}_I)$. Radial PIM constructs the approximation function $u(\mathbf{x}_I)$ to pass through all these node points using radial basis function $B_i(\mathbf{x}_I)$ and polynomial basis function $P_j(\mathbf{x}_I)$.

$$u(\mathbf{x}_I) = \sum_{i=1}^n B_i(\mathbf{x}_I) a_i(\mathbf{x}_I) + \sum_{j=1}^m P_j(\mathbf{x}_I) b_j(\mathbf{x}_I) = \mathbf{B}^T(\mathbf{x}_I) \mathbf{a} + \mathbf{P}^T(\mathbf{x}_I) \mathbf{b} \quad (7)$$

Where a_i is the coefficient for $B_i(\mathbf{x}_I)$ and b_j for $P_j(\mathbf{x}_I)$ (usually, $m < n$).

The vectors of the equation (7) are defined as,

$$\begin{aligned}
 \mathbf{a}^T(\mathbf{x}_I) &= [a_1(\mathbf{x}_I), a_2(\mathbf{x}_I), a_3(\mathbf{x}_I), \dots, a_n(\mathbf{x}_I)] \\
 \mathbf{b}^T(\mathbf{x}_I) &= [b_1(\mathbf{x}_I), b_2(\mathbf{x}_I), \dots, b_n(\mathbf{x}_I)] \\
 \mathbf{B}^T(\mathbf{x}_I) &= [B_1(\mathbf{x}_I), B_2(\mathbf{x}_I), B_3(\mathbf{x}_I), \dots, B_n(\mathbf{x}_I)] \\
 \mathbf{P}^T(\mathbf{x}_I) &= [p_1(\mathbf{x}_I), p_2(\mathbf{x}_I), \dots, p_m(\mathbf{x}_I)]
 \end{aligned} \tag{8}$$

Several known Radial Basis Function's (RBF) are well studied and developed [21, 45, 46]. In this thesis, the Multiquadric function is used, initially proposed by Hardy [45].

Therefore, the RBF used, for a general 2D problem has the following general form,

$$B_{ij} = (r_{ij}^2 + c^2)^p \tag{9}$$

Where c and p are the two shape parameters which should be considered as $c=0.0001$ and $p=0.9999$ in order to maximize the method's performance [5, 47]. The variation of these parameters greatly affect the performance of the RBF.

The variable of the RBF is the Euclidian norm r_{ij} , which defines the distance between the interest point \mathbf{x}_I and the neighbour node \mathbf{x}_i ,

$$r_{ij} = [(x_I - x_i)^2 + (y_I - y_i)^2]^{1/2} \tag{10}$$

The polynomial basis functions have the following monomial terms as,

$$\mathbf{P}^T(\mathbf{x}_I) = [1, x, y, x^2, xy, y^2, \dots] \tag{11}$$

The polynomial basis function used for 2D analysis are.

$$\text{Null basis} - \mathbf{x}^T = \{x, y\}; \mathbf{p}^T(\mathbf{x}) = \{0\}; m = 0$$

$$\text{Constant basis} - \mathbf{x}^T = \{x, y\}; \mathbf{p}^T(\mathbf{x}) = \{1\}; m = 1$$

$$\text{Linear basis} - \mathbf{x}^T = \{x, y\}; \mathbf{p}^T(\mathbf{x}) = \{1, x, y\}; m = 3$$

$$\text{Quadratic basis} - \mathbf{x}^T = \{x, y\}; \mathbf{p}^T(\mathbf{x}) = \{1, x, y, x^2, xy, y^2\}; m = 6$$

The same process can be applied for a 3D problem.

The polynomial term is an extra-requirement that guarantees unique approximation. Following constraints are usually imposed,

$$\sum_{i=1}^n P_j(x_k, y_i) a_i = 0, \quad j = 1, 2, \dots, m \quad (12)$$

It can be expressed in a matrix form, as follows:

$$\begin{bmatrix} \mathbf{B}_0 & \mathbf{P}_0 \\ \mathbf{P}_0^T & \mathbf{0} \end{bmatrix} \begin{Bmatrix} \mathbf{a} \\ \mathbf{b} \end{Bmatrix} = \begin{Bmatrix} \mathbf{u}^e \\ \mathbf{0} \end{Bmatrix} \quad \text{or} \quad \mathbf{G} \begin{Bmatrix} \mathbf{a} \\ \mathbf{b} \end{Bmatrix} = \begin{Bmatrix} \mathbf{u}^e \\ \mathbf{0} \end{Bmatrix} \quad (13)$$

The vector for function values is defined as

$$\mathbf{u}^e = [u_1, u_2, u_3, \dots, u_n]^T \quad (14)$$

The coefficient matrix \mathbf{B}_0 on unknowns a is,

$$\mathbf{B}_0 = \begin{bmatrix} B_1(x_1, y_1) & B_2(x_1, y_1) & \dots & B_n(x_1, y_1) \\ B_1(x_2, y_2) & B_2(x_2, y_2) & \dots & B_n(x_2, y_2) \\ \vdots & \vdots & \ddots & \vdots \\ B_1(x_n, y_n) & B_2(x_n, y_n) & \dots & B_n(x_n, y_n) \end{bmatrix} \quad (15)$$

The coefficient matrix \mathbf{P}_0 on unknowns b is

$$\mathbf{P}_0 = \begin{bmatrix} P_1(x_1, y_1) & P_2(x_1, y_1) & \cdots & P_m(x_1, y_1) \\ P_1(x_2, y_2) & P_2(x_2, y_2) & \cdots & P_m(x_2, y_2) \\ \vdots & \vdots & \ddots & \vdots \\ P_1(x_n, y_n) & P_2(x_n, y_n) & \cdots & P_m(x_n, y_n) \end{bmatrix} \quad (16)$$

Because the distance is directionless, there is $B_k(x_i, y_i) = B_i(x_k, y_k)$, which means that the matrix \mathbf{B}_0 is symmetric. Unique solution is obtained if the inverse of matrix \mathbf{B}_0 exists. Thus, solving the equation (13),

$$\begin{Bmatrix} \mathbf{a} \\ \mathbf{b} \end{Bmatrix} \mathbf{G}^{-1} = \begin{Bmatrix} \mathbf{u}^e \\ \mathbf{0} \end{Bmatrix} \quad (17)$$

Finally, substituting (17) in (7), the interpolation is expressed

$$u(\mathbf{x}_I) = [\mathbf{B}^T(\mathbf{x}_I) \quad \mathbf{P}^T(\mathbf{x}_I)] \mathbf{G}^{-1} \begin{Bmatrix} \mathbf{u}^e \\ \mathbf{0} \end{Bmatrix} = \varphi(\mathbf{x}_I) \mathbf{u}^e \quad (18)$$

in which $\varphi(\mathbf{x}_I)$ is the shape function defined by

$$\varphi(\mathbf{x}_I) = [\phi_1(\mathbf{x}_I), \phi_2(\mathbf{x}_I), \dots, \phi_i(\mathbf{x}_I), \dots, \phi_n(\mathbf{x}_I)] \quad (19)$$

The shape functions are interpolating, since they respect the Kronecker delta property,

$$\phi_i(\mathbf{x}_j) = \begin{cases} 1, & i = j, \quad j = 1, 2, \dots, n \\ 0, & i \neq j, \quad i, j = 1, 2, \dots, n \end{cases} \quad (20)$$

This means that these functions pass through every single node within the influence-domain, in opposition to approximation shape functions which do not. Interpolation shape function reduces the computational cost associated with the numerical analysis. This reduction comes from the possibility to use direct imposition methods (such as the penalty technique) to enforce the essential and natural boundary conditions, in opposition to the Lagrange multipliers in approximation methods.

4. Solid Mechanics Fundamentals

Solid mechanics is the study of deformation and motion under the action of forces. Solid mechanics main goal is to understand the relationship between stress and strain, as well as, the relationship between strain and displacements. Knowing the configuration of the structure, its material characteristics and the applied loads it is possible to define the stress/strain fields using the main relations between them [48].

All solids were considered as being linear-elastic, which means that the relationship between stress and strain is assumed to be linear. Thus, with the removal of the applied load, the solid returns to its initial (undeformed) shape. Additionally, since this is a **static study**, only static loads were applied, meaning that stresses, strains and displacements are not considered as a function of time.

There are two types of materials: anisotropic and isotropic. On the **anisotropic materials**, the properties varies with the directions. The deformation caused by a force applied in a certain direction is different from the deformation caused by the same force applied in a different direction. On the **isotropic materials**, there are only two independent materials properties: the Young Modulus (E) and the Poisson ratio (ν). So, this kind of materials are a special case of anisotropic materials. In this thesis, only isotropic elastic materials were used [38, 49].

4.1 Stress components

Applying external loads, internal forces are produced These internal forces are defined by the amount of force per unit area, entitled **stress**. [50]

The stress in a body, on a certain point, is given by the stress tensor,

$$\boldsymbol{\sigma} = \begin{bmatrix} \sigma_{xx} & \tau_{xy} & \tau_{xz} \\ \tau_{yx} & \sigma_{yy} & \tau_{yz} \\ \tau_{zx} & \tau_{zy} & \sigma_{zz} \end{bmatrix} \quad (21)$$

Therefore, there are six stress components in total at a point. This stress tensor can also be rewritten in a vector form,

$$\boldsymbol{\sigma} = \{\sigma_{xx} \ \sigma_{yy} \ \sigma_{zz} \ \tau_{xy} \ \tau_{yz} \ \tau_{zx}\}^T \quad (22)$$

Stress can be divided into two categories, normal stress, which is perpendicular to the plane in which acts, denoted by the letter σ and shear stress, which is tangential to the acting plane, denoted by the letter τ .

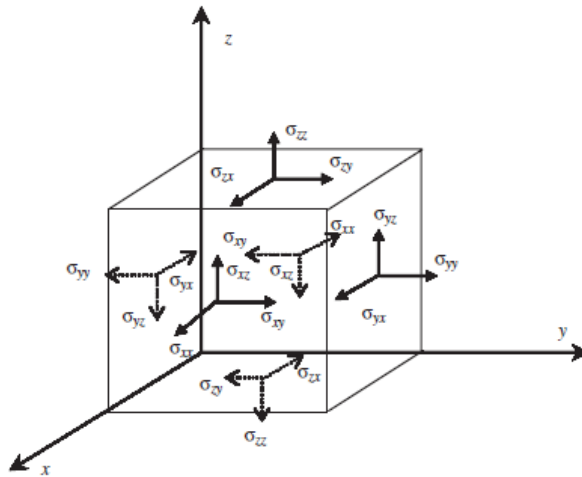


Figure 8: Six independent stress components at a point in a solid viewed on the surfaces of an infinitely small cubic block [50]

4.2 Equilibrium equations

Although stresses vary according the volume of the body, these cannot vary randomly between two given points. An infinitesimal element is characterized by three-dimensional equilibrium equations.

For the same general 3D problem, equilibrium equations can be recognised for an infinitesimal element,

$$\begin{aligned}
\frac{\partial \sigma_{xx}}{\partial x} + \frac{\partial \tau_{yx}}{\partial y} + \frac{\partial \tau_{zx}}{\partial z} + f_x &= 0 \\
\frac{\partial \tau_{xy}}{\partial x} + \frac{\partial \sigma_{yy}}{\partial y} + \frac{\partial \tau_{zy}}{\partial z} + f_y &= 0 \\
\frac{\partial \tau_{xz}}{\partial x} + \frac{\partial \tau_{yz}}{\partial y} + \frac{\partial \sigma_{zz}}{\partial z} + f_z &= 0
\end{aligned} \tag{23}$$

Where f_x, f_y, f_z are the body forces applied on the infinitesimal volume along the directions of the Cartesian axis.

4.3 Components of strain

Because no material is perfectly rigid, when subject to external loads, a body will become deformed. Because of the applied force, a certain point where the force is being applied, leads to a change on the location. Therefore, **strain** is the change of displacement per unit length, and therefore the components of strain can be obtained from the derivatives of the displacements,

$$\begin{aligned}
\varepsilon_{xx} &= \frac{\partial u}{\partial x} \\
\varepsilon_{yy} &= \frac{\partial v}{\partial y} \\
\varepsilon_{zz} &= \frac{\partial w}{\partial z} \\
\gamma_{xy} &= \frac{\partial u}{\partial y} + \frac{\partial v}{\partial x} \\
\gamma_{xz} &= \frac{\partial u}{\partial z} + \frac{\partial w}{\partial x} \\
\gamma_{yz} &= \frac{\partial v}{\partial z} + \frac{\partial w}{\partial y}
\end{aligned} \tag{24}$$

Where u, v and w are the displacements components in the x, y and z directions, respectively.

There is also two types of strain. The normal strain which can be represented by the letter ε , and represents the relative change of length of a certain line segment. And the shear strain, represented by the letter γ and refers to the change in the angle of two previously perpendicular line segments.

$$\boldsymbol{\varepsilon} = \begin{bmatrix} \varepsilon_{xx} & \gamma_{xy} & \gamma_{xz} \\ \gamma_{yx} & \varepsilon_{yy} & \gamma_{yz} \\ \gamma_{zx} & \gamma_{zy} & \varepsilon_{zz} \end{bmatrix} \quad (25)$$

The vector for the strain comes,

$$\boldsymbol{\varepsilon} = \{ \varepsilon_{xx} \ \varepsilon_{yy} \ \varepsilon_{zz} \ \gamma_{xy} \ \gamma_{yz} \ \gamma_{zx} \} \quad (26)$$

The equations (24), the six strain-displacement relationships, can be represented in a matrix form as the product of the partial differential equation operator matrix \mathbf{L} and the displacement field \mathbf{u} ,

$$\boldsymbol{\varepsilon} = \mathbf{L} \mathbf{u} \quad (27)$$

Where \mathbf{u} is the displacement vector, which has the form of,

$$\mathbf{u} = \begin{Bmatrix} u \\ v \\ w \end{Bmatrix} \quad (28)$$

Where \mathbf{L} , the matrix of partial differential operators, is given by,

$$\mathbf{L} = \begin{bmatrix} \frac{\partial}{\partial x} & 0 & 0 & \frac{\partial}{\partial y} & 0 & \frac{\partial}{\partial z} \\ 0 & \frac{\partial}{\partial y} & 0 & \frac{\partial}{\partial x} & \frac{\partial}{\partial z} & 0 \\ 0 & 0 & \frac{\partial}{\partial z} & 0 & \frac{\partial}{\partial y} & \frac{\partial}{\partial x} \end{bmatrix}^T \quad (29)$$

4.4 Constitutive equations

All solids used in this work were considered as being isotropic and linear-elastic. Due to this, not only is the material fully defined by just its Elastic Modulus E and by its Poisson's ratio ν , but the components of stress and strain relation is given by the generalized Hooke's law,

$$\boldsymbol{\sigma} = \boldsymbol{c} \boldsymbol{\varepsilon} \quad (30)$$

Where \boldsymbol{c} is the material constitutive matrix defined by,

$$\boldsymbol{c} = \frac{E}{(1+\nu)(1-2\nu)} \begin{bmatrix} 1-\nu & \nu & \nu & 0 & 0 & 0 \\ \nu & 1-\nu & \nu & 0 & 0 & 0 \\ \nu & \nu & 1-\nu & 0 & 0 & 0 \\ 0 & 0 & 0 & (1-2\nu)/2 & 0 & 0 \\ 0 & 0 & 0 & 0 & (1-2\nu)/2 & 0 \\ 0 & 0 & 0 & 0 & 0 & (1-2\nu)/2 \end{bmatrix} \quad (31)$$

4.5 Strong form and weak formulation

The differential equations governing the performance of an arbitrary problem must follow the equilibrium equations presented in equation (23) or other kind of equilibrium equations that are the result of simplifications of the equations (23). This is the **strong form formulation** in solid mechanics, which means that the differential equations must be satisfied at every single mathematical point of the domain. Solving these kinds of equations is not efficient, particularly, in problems with intricate domains, several material interfaces and complex boundary conditions.

Thus, the **weak form formulation** is used to achieve the insufficiencies in the field of computational mechanics of the strong form. Instead of solving differential equations which may not always have a straightforward solution, it produces a set of discretized systems equations in an integral form, being established for each integration point. Hence, the accuracy of the solution depends on the density of the mesh discretizing the problem domain. Furthermore, the implementation of the boundary conditions is easier since they can be applied directly to any arbitrary node. [5, 8, 50, 51]

4.5.1 Galerkin weak form

The RPIM formulation uses the Galerkin weak formulation to obtain approximate solutions based on an energy principle: the Hamilton's principle. Hamilton's principle allows the derivation of the partial differential equations for the problem and states: "Of all the admissible time histories of displacement the most accurate solution makes the Lagrangian functional of a minimum." [50].

The Lagrangian function, L , has all the physical information regarding the problem, as well the forces acting on it,

$$L = T - U + W_f \quad (32)$$

Where T is the kinetic energy, U is the strain energy and W_f is the work produced by the external forces.

Combining the equation (32) and the idea behind the Hamilton's principle,

$$\int_{t_1}^{t_2} (\delta T - \delta U + \delta W_f) dt = 0 \quad (33)$$

Or substituting (32) in (33),

$$\delta \int_{t_1}^{t_2} L dt = 0 \quad (34)$$

Considering a solid, in which Ω denotes a domain of \mathbb{R}^3 , Γ the exterior boundary, Γ_t the natural boundary in which an external force f is applied, Γ_u the essential boundary where displacements are constrained and \mathbf{b} and $\bar{\mathbf{t}}$ are the body force applied on the solid and the traction force vector, respectively, as shown in the Figure 9,

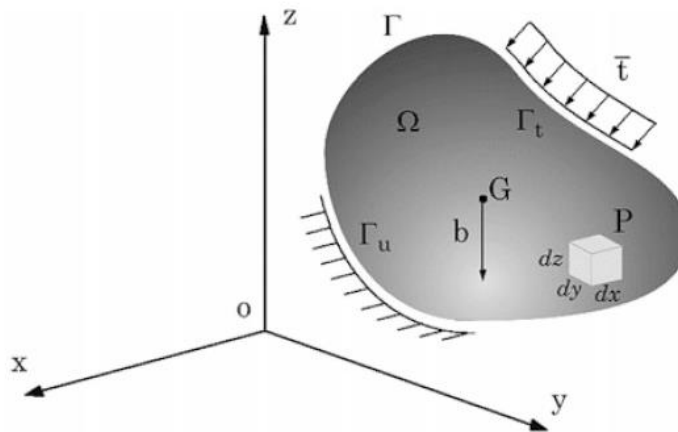


Figure 9: 3D solid mechanics problem

The strain energy, for a linear-elastic material can be expressed as,

$$U = \frac{1}{2} \int_{\Omega} \boldsymbol{\varepsilon}^T \boldsymbol{\sigma} d\Omega \quad (35)$$

The kinetic energy is defined as,

$$T = \frac{1}{2} \int_{\Omega} \rho \dot{\mathbf{u}}^T \dot{\mathbf{u}} d\Omega \quad (36)$$

Where $\dot{\mathbf{u}}$ is the velocity, displacement's first derivate with respect to time, and ρ is the density of the material point.

The work produced by external forces comes,

$$W_f = \int_{\Omega} \mathbf{u}^T \mathbf{b} d\Omega + \int_{\Gamma_t} \mathbf{u}^T \bar{\mathbf{t}} d\Gamma \quad (37)$$

By substituting equations (35), (36) and (37) in equation (32) the following is obtained,

$$\int_{t_1}^{t_2} \left[\frac{1}{2} \int_{\Omega} \delta(\rho \dot{\mathbf{u}}^T \dot{\mathbf{u}}) d\Omega - \frac{1}{2} \int_{\Omega} \delta(\boldsymbol{\varepsilon}^T \boldsymbol{\sigma}) d\Omega + \int_{\Omega} \delta \mathbf{u}^T \mathbf{b} d\Omega + \int_{\Gamma_t} \delta \mathbf{u}^T \bar{\mathbf{t}} d\Gamma \right] = 0 \quad (38)$$

Since only static problems are considered, the first term of equation (38) can be eliminated,

$$\int_{t_1}^{t_2} \left[-\frac{1}{2} \int_{\Omega} \delta(\boldsymbol{\varepsilon}^T \boldsymbol{\sigma}) d\Omega + \int_{\Omega} \delta \mathbf{u}^T \mathbf{b} d\Omega + \int_{\Gamma_t} \delta \mathbf{u}^T \bar{\mathbf{t}} d\Gamma \right] dt = 0 \quad (39)$$

Several simplifications can be made to the first term of the integral (39). The integrand function is,

$$\delta(\boldsymbol{\varepsilon}^T \boldsymbol{\sigma}) = \delta \boldsymbol{\varepsilon}^T \boldsymbol{\sigma} + \boldsymbol{\varepsilon}^T \delta \boldsymbol{\sigma} \quad (40)$$

Given that both terms are scalars in equation (40), they can be transposed without affecting the result,

$$\boldsymbol{\varepsilon}^T \delta \boldsymbol{\sigma} = (\boldsymbol{\varepsilon}^T \delta \boldsymbol{\sigma})^T = \delta \boldsymbol{\sigma}^T \boldsymbol{\varepsilon} \quad (41)$$

Attending to the generalized Hooke's law shown in equation (30), and the symmetric property of material matrix shown in (31), $\mathbf{c}^T = \mathbf{c}$, it is possible to write equation (41) as,

$$\delta \boldsymbol{\sigma}^T \boldsymbol{\varepsilon} = \delta \boldsymbol{\varepsilon}^T \boldsymbol{\sigma} \quad (42)$$

Substituting equation (42) in (40),

$$\delta(\boldsymbol{\varepsilon}^T \boldsymbol{\sigma}) = 2\delta \boldsymbol{\varepsilon}^T \boldsymbol{\sigma} \quad (43)$$

Replacing equation (43) in (40),

$$\int_{t_1}^{t_2} \left[- \int_{\Omega} \delta \boldsymbol{\varepsilon}^T \boldsymbol{\sigma} d\Omega + \int_{\Omega} \delta \mathbf{u}^T \mathbf{b} d\Omega + \int_{\Gamma_t} \delta \mathbf{u}^T \bar{\mathbf{t}} d\Gamma \right] dt = 0 \quad (44)$$

For the time integration to be valid for any pair of initial and final time, t_1 and t_2 respectively, the integrand of (44) must be null. This lead to the "Galerkin weak form" equation,

$$- \int_{\Omega} \delta \boldsymbol{\varepsilon}^T \boldsymbol{\sigma} d\Omega + \int_{\Omega} \delta \mathbf{u}^T \mathbf{b} d\Omega + \int_{\Gamma_t} \delta \mathbf{u}^T \bar{\mathbf{t}} d\Gamma = 0 \quad (45)$$

Substituting equations (27) and (30) in (45), the generic Galerkin weak form written in terms of displacement is obtained,

$$\int_{\Omega} \delta(\mathbf{L}\mathbf{u})^T \mathbf{c}(\mathbf{L}\mathbf{u}) d\Omega + \int_{\Omega} \delta\mathbf{u}^T \mathbf{b} d\Omega - \int_{\Gamma_t} \delta\mathbf{u}^T \bar{\mathbf{t}} d\Gamma = 0 \quad (46)$$

4.6 Discrete Systems Equations

The principle of virtual work states that the total virtual work done by the body internal stresses and the applied external forces on a system in static equilibrium is zero for a set of infinitesimal virtual displacements from equilibrium. The discrete system of equations for meshless methods are obtained based on the principle of virtual work, with the shape functions presented in the chapter 3 being used as trial functions.

The approximation of the variable field in an integration point \mathbf{x}_I comes [22],

$$\mathbf{u}(\mathbf{x}_I) = \sum_{i=1}^n \varphi_i(\mathbf{x}_I) \mathbf{u}_i \quad (47)$$

which $\varphi_i(\mathbf{x}_I)$ is the meshless interpolation function and \mathbf{u}_i is the nodal displacement vector of the n nodes belonging to the influence domain of the integration point \mathbf{x}_I .

By the principle of virtual work, virtual displacements of nodes within the “influence-domain” of an interest point \mathbf{x}_I cause a virtual displacement in the integration point itself, and it can be interpolated considering the interpolation functions. The test function or virtual displacement is defined as,

$$\delta\mathbf{u}(\mathbf{x}_I) = \sum_{i=1}^n \varphi_i(\mathbf{x}_I) \delta\mathbf{u}_i \quad (48)$$

Where $\delta \mathbf{u}(\mathbf{x}_I)$ is the nodal values for the test function. Which can be substituted in equation (46), obtaining,

$$\int_{\Omega} \left(\sum_{i=1}^n \varphi_i(\mathbf{x}_I) \delta \mathbf{u}_i \right)^T \mathbf{L}^T \mathbf{c} \mathbf{L} \sum_{j=1}^n \varphi_j(\mathbf{x}_I) \mathbf{u}_j \, d\Omega - \int_{\Omega} \left(\sum_{i=1}^n \varphi_i(\mathbf{x}_I) \delta \mathbf{u}_i \right)^T \mathbf{b} \, d\Omega - \int_{\Gamma_t} \left(\sum_{i=1}^n \varphi_i(\mathbf{x}_I) \delta \mathbf{u}_i \right)^T \bar{\mathbf{t}} \, d\Gamma = 0 \quad (49)$$

Equation (49) can be also written as,

$$\sum_{i=1}^n \sum_{j=1}^n \delta \mathbf{u}_i^T \int_{\Omega} \mathbf{B}^T \mathbf{c} \mathbf{B} \, d\Omega \mathbf{u}_j - \sum_{i=1}^n \delta \mathbf{u}_i^T \int_{\Omega} \varphi_i^T(\mathbf{x}_I) \mathbf{b} \, d\Omega - \sum_{i=1}^n \delta \mathbf{u}_i^T \int_{\Omega} \varphi_i^T(\mathbf{x}_I) \bar{\mathbf{t}} \, d\Omega = 0 \quad (50)$$

Where the deformability matrix \mathbf{B} is given by,

$$\mathbf{B} = \begin{bmatrix} \frac{\partial \varphi_i}{\partial x} & 0 & 0 & \frac{\partial \varphi_i}{\partial y} & 0 & \frac{\partial \varphi_i}{\partial z} \\ 0 & \frac{\partial \varphi_i}{\partial y} & 0 & \frac{\partial \varphi_i}{\partial x} & \frac{\partial \varphi_i}{\partial z} & 0 \\ 0 & 0 & \frac{\partial \varphi_i}{\partial z} & 0 & \frac{\partial \varphi_i}{\partial y} & \frac{\partial \varphi_i}{\partial x} \end{bmatrix}^T \quad (51)$$

Being $i = \{1, 2, \dots, n\}$ the order of the node within the influence-domain of \mathbf{x}_I .

Equation (50) can be represented as,

$$\delta \mathbf{U}^T (\mathbf{K} \mathbf{u} - \mathbf{F}) = 0 \quad (52)$$

Where \mathbf{F} is the sum of the second and third term of equation (50).

Thus, equation (52) can be finally translated in the following linear equation,

$$(\mathbf{K} \mathbf{u} - \mathbf{F}) = 0 \quad (53)$$

Essential boundaries can be directly applied in the stiffness matrix, \mathbf{K} , because of possessing the Kronecker delta property.

5.3D Model Construction

A three-dimensional analysis will be performed for a dental implant.

The dental implant under study is built with three major parts: the titanium sleeve, the nylon sleeve and the abutment. With the technical drawings, Figure 10, it was possible to draw two out of three parts of the implant: the titanium sleeve and the abutment. For the nylon sleeve, as the technical drawing was not available, it was assumed that the space between the titanium sleeve and the abutment was filled with nylon representing the corresponding part.

In the next subchapters, a brief introduction to the program used for the analysis, the materials used for the three parts of the dental implant, the loads applied on it and the essential boundaries used in the analysis will be presented.

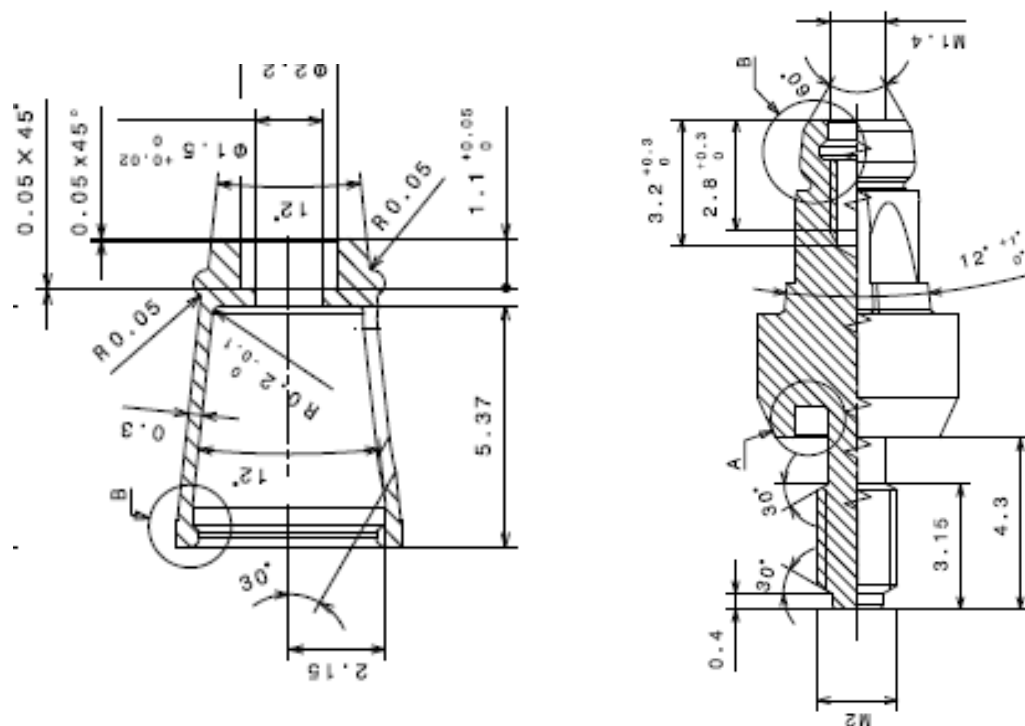


Figure 10: Detailed scheme of the parts belonged to the dental implant on study



Figure 11: Images of titanium sleeve and abutment, respectively [1]

5.1 Programs

The meshing of the implant was done in a commercial software, due to the high complexity of the geometry of the dental implant. The final model has a total of 9202 nodes. Afterwards, the several analyses were performed on FEMAS. Nevertheless, it would be possible to construct the geometric model and corresponding mesh using directly the FEMAS software. Therefore, a brief description of this software will be done.

5.1.1 FEMAS

FEMAS, acronym for “Finite Element and Meshless Method Analysis Software” is an academic software, developed in the commercial software *MATLAB*, created by Jorge Belinha, professor and researcher at the Faculty of Engineering of the University of Porto, to analyze several computational mechanics problems using the Finite Element Method (FEM) and several meshless methods (RPIM and NRPIM) [52].

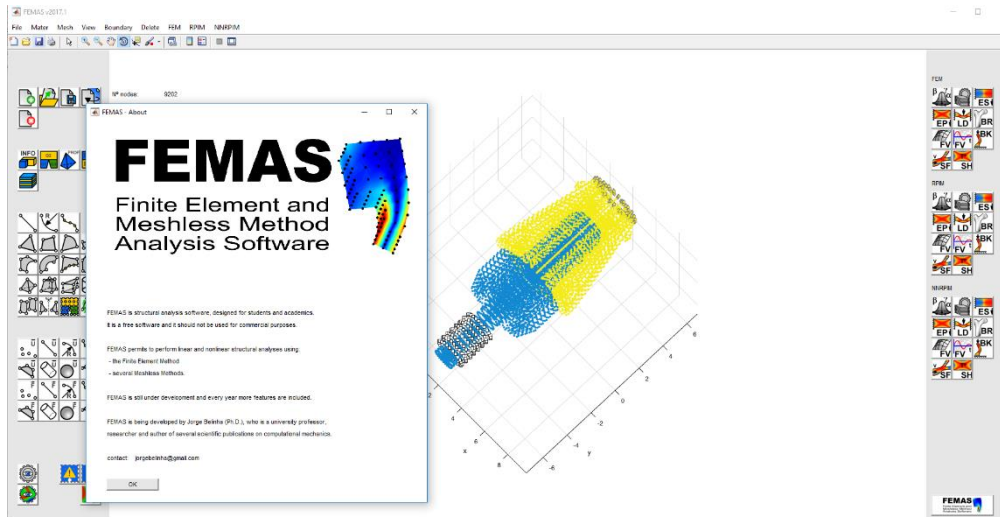


Figure 12: FEMAS initial presentation and GUI interface

FEMAS can perform the following analyses:

- Static linear-elastic
- Elasto-plastic
- Crack opening path
- Bone tissue remodeling
- Free Vibration
- Bucking
- Fluid flow (low velocities)

It is possible to work with 2D and 3D problems with FEMAS. The computational framework uses the classical three-dimensional deformation theory, 3D problems, and the plane stress and plane strain 2D deformation theory, for 2D problems, and allows the use of both isotropic and anisotropic materials, which the user can choose. The software permits to build autonomously the 2D and 3D numerical model. The user controls the nodal discretization, the material disposition and the location of the essential and natural boundary condition. All these tasks are performed without the use of any external CAD software. Still, meshes generated with others CAD commercial software can also be imported and read using FEMAS.

The elastic static analysis performed by FEMAS can be divided in three phases: pre-process, process and post-process. For more detail, see Table 3.

Additionally, FEMAS allows to present the displacement, stress and strain fields along with the solid domain using figures and arrays, which permits further data analysis, as it is possible to observe in the Figure 13.

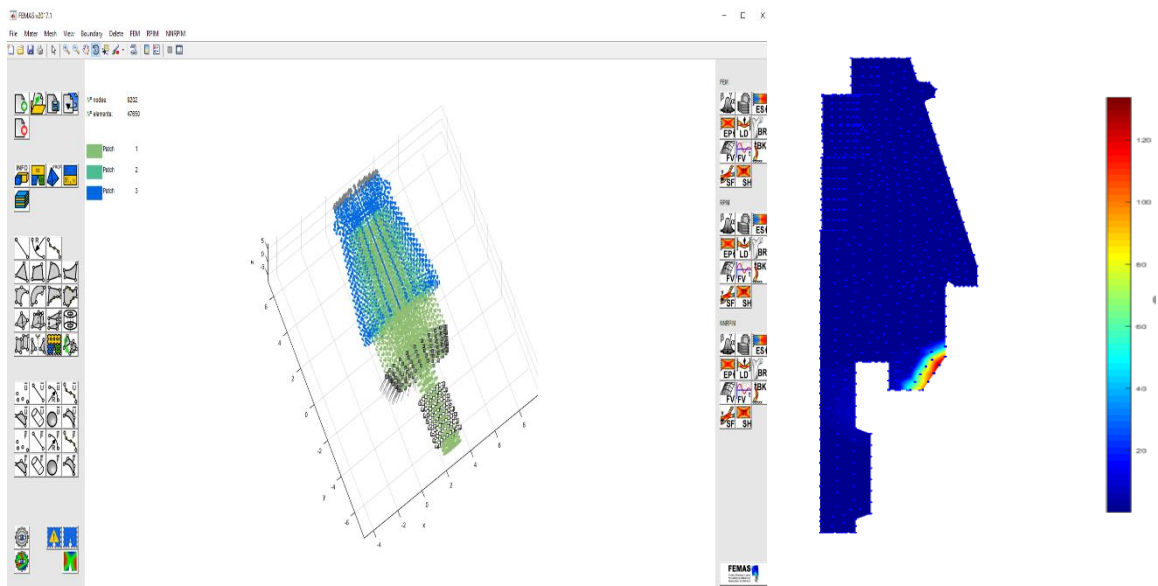


Figure 13: Example of a 3D model of a complex dental implant on FEMAS and its natural and essential boundaries; Example of a stress field of the dental implant obtained with FEMAS

Table 3: Phases description [53]

	Phase	Phase description
Pre-process	1. Pre-process	Nodal discretization is determined. Influence-domains are found (meshless methods); elements are created (FEM). Integration mesh is determined
	2. Shape function	Shape functions are determined for all integration points
Process	3. Stiffness matrix	Local stiffness matrix is determined and the global stiffness matrix is assembled
	4. Natural boundary	Natural boundary is defined, and external forces are applied
	5. Essential boundary	Essential boundary is defined and constrained displacements are imposed
	6. Displacement field	Displacement field vector is determined
	7. Stress/Strain field	Strain and stress fields are determined
Post-process	8. Field images	The variable fields are presented in the FEMAS GUI

5.2 Materials

5.2.1 Nylon sleeve

The polymers have a few **advantages** in comparison with other kind of materials. Thus, polymer possess: a high biocompatibility; the possibility of changing easily its properties; and a low friction coefficient. Additionally, polymers are easy to work with and to modify chemically and physically its properties (even in the most complex structures).

However, the presence of some substances such as monomers, catalyzers and additives (which can be released to the body), the facility of absorbing water and biomolecules of the surrounding atmosphere and the low mechanical properties are the main **problems** of using this kind of materials.

For the nylon sleeve, the polymer used was the *Grilamid*, which is a Nylon. The different kinds of the materials used in this work are shown next. Thus, a brief description of each kind and its mechanical properties is presented.

5.2.1.1 Description

Grilamid L 20 H FWA Natural (L20H) is a medium viscosity, unreinforced and heat stabilized Polyamide 12. Used for direct contact with potable water and food-stuff.

Grivory GV-5 FWA Natural (GV5) is a 50% glass fiber reinforced engineering thermoplastic material based on a combination of semi-crystalline with partially aromatic copolyamide. Suitable for parts in direct contact with drinking water and food.

Grilamid LV-3H (LV3H) is a 30% glass fiber reinforced, heat stabilized polyamide 12 injection moulding grade. This material is suitable for production of technical parts in the application fields of electronics, automotive, safety technology, mechanical engineering and domestic appliances.

Grilamid LKN-5HI (LKN) is a 50% glass bead reinforced, heat stabilized polyamide 12 injection moulding part.

5.2.1.2 Mechanical Properties

Table 4: Mechanical properties of the several polymers for the nylon sleeve used on the analysis

Material	Tensile E Modulus [MPa]	Tensile Strength at Yield [MPa]	Elongation at Yield [%]	Tensile Strength at Break [MPa]	Elongation at Break [%]
Grilamid L 20 H FWA Natural	1100	40	12	-	> 50
Grivory GV-5 FWA Natural	18000	250	-	-	2.5
Grilamid LV-3H	6000	-	-	105	8
Grilamid LKN-5H	2300	45	7	40	25

5.2.2 Titanium sleeve and abutment

As mentioned before in section 2.1.2, the titanium is a very good material to use in dental implants. Thus, both the abutment and the sleeve covering the nylon sleeve will be made of titanium. In Table 5, it is presented the mechanical properties of two different kinds of commercial titanium.

Table 5: Mechanical properties of the titanium used on the analysis

<u>Properties</u>	<u>Ti, degree 4</u>	<u>Ti, degree 5</u>
ρ (kg/m^3)	4.55	4428.78
E (GPa)	120	113.8
ν	0.37	0.342
σ_{ced} (MPa)	690	880
σ_{rot} (MPa)	400	950

5.3 Loads

For simulate the masticatory forces, it was applied seven different **load** cases on the upper part of the dental implant (more precisely in the titanium sleeve) uniformly distributed. The angle of the applied forces was varied accordingly with Table 6. The masticatory forces will be considered 150 N in y direction (vertical) and 15 N in the x direction (horizontal) [43].

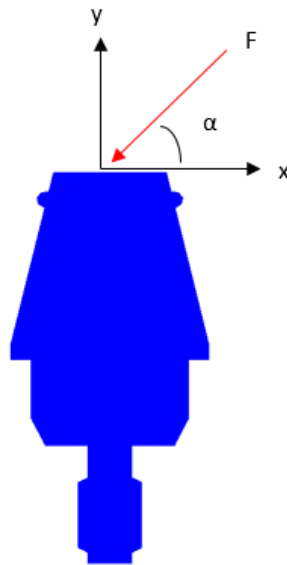


Figure 14: Schematic representation of the load cases

Table 6: Force angles and consequent Cartesian components (N)

Angle	f_x	f_y	f_z
90°	0	1	0
75°	0.174	0.966	0
60°	0.5	0.866	0
45°	0.707	0.707	0
30°	0.866	0.5	0
15°	0.966	0.259	0
0°	1	0	0

Since it is only aimed to study the elastic response of the materials, in this study all the applied forces have as magnitude 1N. This allows to obtain the result of any another load magnitude by just multiplying the value of the load by the obtained result.

For simulating the implant screw attach, a study of **torsion** will be performed. Four equal forces were applied on the upper part of the titanium sleeve, with 90° degrees between them, as it is possible to observe in the Figure 15.

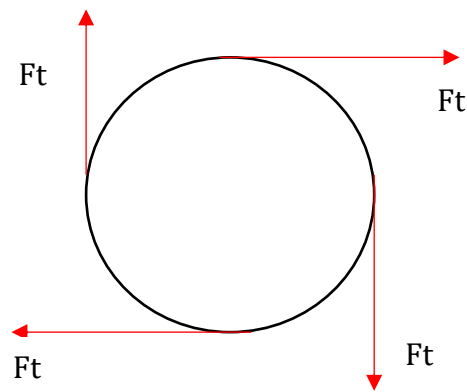


Figure 15: Representative scheme of the forces for torsion

Since it is only aimed to study the elastic response of the materials, in this study the moment applied has as magnitude of 1Nmm. This allows to obtain the result of any another moment magnitudes by just multiplying the value of the moment by the obtained result.

5.4 Essential boundaries conditions

For the studied implant, there were considered three distinct essential boundaries conditions, see Figure 16.

The case (1) represents the worst possible condition that the implant can experience. It is the example of a complete osseous reabsorption. The dental implant only be attached by its thread.

The case (2) is representing an example in which the cortical bone has a high Young modulus, E , and the trabecular bone has a low Young modulus. This also means that the cortical bone is strong and the trabecular bone is fragile.

For the last case, case (3), a mixed case between case (1) and case (2) is considered. This case attempts to reproduce a real normal scenario.

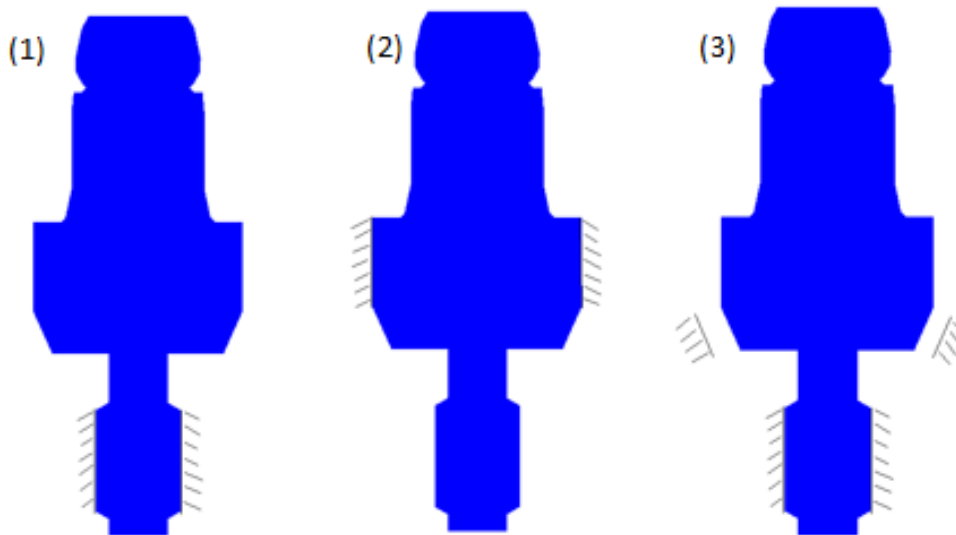


Figure 16: Different types of essential boundaries conditions.

Thus, four mechanical cases were performing, considering these three essential conditions.

For the first boundary condition (1), it was applied the different loads, Mechanical Case A (MCA) and the torsion, Mechanical Case D (MCD)

For the second type of essential boundary (2) it was applied the different loads, Mechanical Case B (MCB).

For last, for essential boundary (3), it was again applied the different loads, Mechanical Case C (MCC).

6. Numerical Analysis

The 3D geometric model used was the one presented in the chapter 5. All the examples presented in this chapter are analysed with the linear tetrahedral finite element. All the analyses were performed with the FEM and the RPIM, making a comparison between them afterwards. For the RPIM, it was used the parameters (c and p) already mentioned in the section 3.3. However, for the analysis the parameters used were: the number of nodes inside the influence domain was 27, $c = 1.42$, $p = 1.03$, the polynomial basis is constant and it was used tetrahedrons instead of hexahedrons.

In all the following examples, the material used for the titanium sleeve and the abutment was the *titanium degree 5th* (presented in the Table 5). Regarding the nylon sleeve, for mechanical cases MCA, MCB, MCC and MCD, the material used was the *Grilamid L20 H FWA Natural*, presented in Table 4. In section 6.5 it is presented a study for distinct nylon materials. Thus, in section 6.5 all the nylon types from the Table 4 were considered and a comparison study was performed.

Both FEM and RPIM are discretization techniques well studied and validated in the literature [5, 50]. Preliminary tests have shown that the nodal discretization level used in this work is sufficient to obtain a stable (converged) solution.

6.1 Mechanical Case A

The first mechanical case analysed, Mechanical Case A (MCA), considers the seven different forces described in Table 6 and the boundary condition (1), shown in Figure 16.

In order to understand the effect of the load orientation in the implant, three interest points were selected in the interior of the domain, Figure 17. From these points were obtained the local displacements, stresses and strains.

Regarding interest point P1, it is possible to observe the measured local displacements, stresses and strains in Table 7. For the interest point P2, it is possible to observe the measured local displacements, stresses and strains in Table

8. And, concerning interest point P3, it is possible to observe the measured local displacements, stresses and strains in Table 9.

Additionally, in order to clarify the results of Table 7, Table 8 and Table 9, auxiliary graphics are presented, showing the variation of the stress and strain to the three points on study for both numerical methods (FEM and RPIM) for the distinct load angles, see Figure 18 and Figure 19.

Moreover, in order to show the stress and strain distribution in complete domain, stress and strain maps are presented, respectively, for the three distinct parts that constitute the dental implant, allowing to visually compare the RPIM and FEM solutions for distinct load angles. For the abutment, see Table 10 and Table 11. To the nylon sleeve, see Table 12 and Table 13. Finally, for the titanium sleeve, see Table 14 and Table 15.

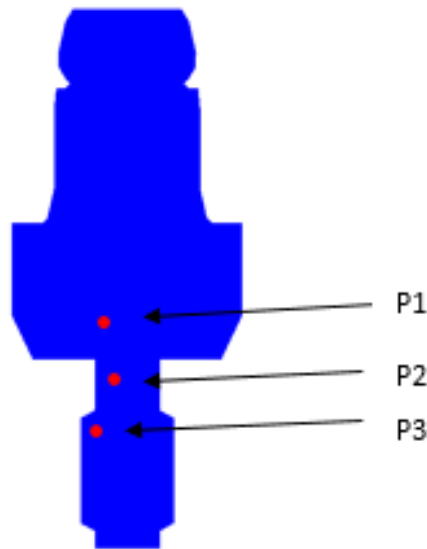


Figure 17: Interest Point for analyses on MCA

Table 7: Obtained values for point 1 with both numerical methods, with respect to the angle of the applied load.

Angle	Method	ux	uy	uz	σ_1	σ_2	σ_3	σ_{ef}	ϵ_1	ϵ_2	ϵ_3	ϵ_{ef}
0	FEM	-1,32E-03	-5,35E-04	3,17E-06	-8,17E-01	1,62E+00	9,46E+00	8,27E+00	2,20E-05	1,29E-05	-7,67E-05	6,60E-05
	RPIM	-1,41E-03	-5,61E-04	-4,30E-07	-4,41E-01	1,66E+00	1,03E+01	9,30E+00	2,76E-05	1,37E-05	-8,49E-05	7,37E-05
	Dif.	6,82E-02	4,93E-02	1,14E+00	4,60E-01	2,86E-02	8,75E-02	1,24E-01	2,55E-01	6,10E-02	1,06E-01	1,17E-01
15	FEM	-1,28E-03	-5,20E-04	3,07E-06	-8,13E-01	1,58E+00	9,23E+00	8,06E+00	2,14E-05	1,26E-05	-7,48E-05	6,43E-05
	RPIM	-1,37E-03	-5,46E-04	-4,14E-07	-4,50E-01	1,63E+00	1,00E+01	9,06E+00	2,68E-05	1,34E-05	-8,27E-05	7,18E-05
	Dif.	6,82E-02	4,91E-02	1,13E+00	4,47E-01	2,94E-02	8,72E-02	1,23E-01	2,55E-01	5,99E-02	1,06E-01	1,16E-01
30	FEM	-1,15E-03	-4,70E-04	2,77E-06	-7,54E-01	1,44E+00	8,37E+00	7,30E+00	1,92E-05	1,14E-05	-6,78E-05	5,83E-05
	RPIM	-1,22E-03	-4,93E-04	-3,70E-07	-4,27E-01	1,48E+00	9,10E+00	8,20E+00	2,41E-05	1,21E-05	-7,50E-05	6,50E-05
	Dif.	6,82E-02	4,89E-02	1,13E+00	4,33E-01	3,03E-02	8,68E-02	1,23E-01	2,55E-01	5,88E-02	1,05E-01	1,16E-01
45	FEM	-9,36E-04	-3,88E-04	2,27E-06	-6,43E-01	1,20E+00	6,95E+00	6,05E+00	1,58E-05	9,50E-06	-5,62E-05	4,83E-05
	RPIM	-1,00E-03	-4,07E-04	-3,01E-07	-3,75E-01	1,23E+00	7,55E+00	6,78E+00	1,99E-05	1,00E-05	-6,21E-05	5,38E-05
	Dif.	6,82E-02	4,88E-02	1,13E+00	4,16E-01	3,15E-02	8,63E-02	1,22E-01	2,55E-01	5,73E-02	1,04E-01	1,15E-01
60	FEM	-6,62E-04	-2,80E-04	1,62E-06	-4,87E-01	-8,74E-01	5,05E+00	4,38E+00	1,13E-05	6,91E-06	-4,08E-05	3,50E-05
	RPIM	-7,07E-04	-2,93E-04	-2,11E-07	-2,98E-01	-9,04E-01	5,48E+00	4,91E+00	1,42E-05	7,29E-06	-4,50E-05	3,90E-05
	Dif.	6,82E-02	4,83E-02	1,13E+00	3,89E-01	3,35E-02	8,53E-02	1,20E-01	2,54E-01	5,48E-02	1,03E-01	1,13E-01
75	FEM	-3,43E-04	-1,52E-04	8,65E-07	-2,98E-01	-4,93E-01	2,81E+00	2,42E+00	6,08E-06	3,85E-06	-2,26E-05	1,94E-05
	RPIM	-3,66E-04	-1,59E-04	-1,07E-07	-1,99E-01	-5,12E-01	3,04E+00	2,70E+00	7,62E-06	4,04E-06	-2,48E-05	2,15E-05
	Dif.	6,81E-02	4,74E-02	1,12E+00	3,33E-01	3,82E-02	8,29E-02	1,16E-01	2,52E-01	4,86E-02	9,99E-02	1,09E-01
90	FEM	-2,98E-07	-1,42E-05	4,69E-08	-6,18E-02	-7,72E-02	-3,97E-01	3,28E-01	7,07E-07	5,31E-07	-3,12E-06	2,65E-06
	RPIM	-2,85E-07	-1,46E-05	4,93E-09	-6,22E-02	-8,43E-02	-4,14E-01	3,41E-01	7,66E-07	5,14E-07	-3,25E-06	2,76E-06
	Dif.	4,29E-02	2,84E-02	8,95E-01	7,74E-03	9,19E-02	4,24E-02	4,06E-02	8,32E-02	3,15E-02	4,10E-02	4,11E-02

Table 8: Obtained values for point 2 with both numerical methods, with respect to the angle of the applied load.

Angle	Method	ux	uy	uz	σ_1	σ_2	σ_3	σ_{ef}	ϵ_1	ϵ_2	ϵ_3	ϵ_{ef}
0	FEM	-2,73E-04	-1,67E-04	3,39E-06	-5,16E-01	-8,62E-01	1,58E+01	1,51E+01	3,95E-05	3,55E-05	-1,35E-04	1,19E-04
	RPIM	-2,98E-04	-1,77E-04	-4,82E-07	3,38E-01	-3,69E-01	1,76E+01	1,76E+01	5,04E-05	4,23E-05	-1,55E-04	1,37E-04
	Dif.	9,14E-02	5,61E-02	1,14E+00	1,66E+00	5,72E-01	1,14E-01	1,64E-01	2,78E-01	1,93E-01	1,44E-01	1,57E-01
15	FEM	-2,64E-04	-1,64E-04	3,29E-06	-5,00E-01	-8,35E-01	1,55E+01	1,48E+01	3,85E-05	3,47E-05	-1,32E-04	1,16E-04
	RPIM	-2,88E-04	-1,73E-04	-4,65E-07	3,27E-01	-3,58E-01	1,72E+01	1,72E+01	4,92E-05	4,14E-05	-1,51E-04	1,34E-04
	Dif.	9,14E-02	5,59E-02	1,14E+00	1,65E+00	5,71E-01	1,14E-01	1,63E-01	2,76E-01	1,91E-01	1,43E-01	1,56E-01
30	FEM	-2,37E-04	-1,49E-04	2,96E-06	-4,50E-01	-7,51E-01	1,40E+01	1,34E+01	3,50E-05	3,16E-05	-1,20E-04	1,05E-04
	RPIM	-2,58E-04	-1,57E-04	-4,17E-07	2,93E-01	-3,23E-01	1,56E+01	1,56E+01	4,46E-05	3,76E-05	-1,37E-04	1,22E-04
	Dif.	9,15E-02	5,57E-02	1,14E+00	1,65E+00	5,69E-01	1,13E-01	1,62E-01	2,74E-01	1,89E-01	1,42E-01	1,55E-01
45	FEM	-1,93E-04	-1,24E-04	2,43E-06	-3,69E-01	-6,16E-01	1,17E+01	1,12E+01	2,91E-05	2,63E-05	-9,98E-05	8,75E-05
	RPIM	-2,11E-04	-1,30E-04	-3,40E-07	2,40E-01	-2,66E-01	1,30E+01	1,30E+01	3,70E-05	3,12E-05	-1,14E-04	1,01E-04
	Dif.	9,16E-02	5,55E-02	1,14E+00	1,65E+00	5,67E-01	1,12E-01	1,61E-01	2,71E-01	1,87E-01	1,40E-01	1,53E-01
60	FEM	-1,37E-04	-9,00E-05	1,73E-06	-2,64E-01	-4,38E-01	8,48E+00	8,13E+00	2,12E-05	1,92E-05	-7,26E-05	6,37E-05
	RPIM	-1,49E-04	-9,50E-05	-2,41E-07	1,70E-01	-1,91E-01	9,42E+00	9,41E+00	2,68E-05	2,27E-05	-8,27E-05	7,34E-05
	Dif.	9,17E-02	5,50E-02	1,14E+00	1,64E+00	5,64E-01	1,11E-01	1,58E-01	2,66E-01	1,83E-01	1,38E-01	1,51E-01
75	FEM	-7,12E-05	-5,04E-05	9,18E-07	-1,40E-01	-2,31E-01	4,73E+00	4,54E+00	1,18E-05	1,08E-05	-4,06E-05	3,56E-05
	RPIM	-7,77E-05	-5,31E-05	-1,24E-07	8,87E-02	-1,03E-01	5,24E+00	5,23E+00	1,49E-05	1,27E-05	-4,60E-05	4,08E-05
	Dif.	9,19E-02	5,39E-02	1,14E+00	1,63E+00	5,54E-01	1,07E-01	1,51E-01	2,54E-01	1,72E-01	1,33E-01	1,45E-01
90	FEM	-5,73E-07	-7,28E-06	4,05E-08	-6,21E-03	-6,61E-03	-6,55E-01	6,48E-01	1,69E-06	1,68E-06	-5,72E-06	5,06E-06
	RPIM	-6,64E-07	-7,57E-06	3,82E-10	2,69E-03	-7,70E-03	-6,95E-01	6,92E-01	1,88E-06	1,76E-06	-6,09E-06	5,40E-06
	Dif.	1,59E-01	4,01E-02	9,91E-01	1,43E+00	1,64E-01	6,11E-02	6,79E-02	1,11E-01	4,31E-02	6,51E-02	6,69E-02

Table 9: Obtained values for point 3 with both numerical methods, with respect to the angle of the applied load.

Angle	Method	ux	uy	uz	σ_1	σ_2	σ_3	σ_{ef}	ϵ_1	ϵ_2	ϵ_3	ϵ_{ef}
0	FEM	1,07E-06	-3,42E-05	3,16E-07	1,04E+00	1,82E+00	8,92E+00	7,52E+00	1,92E-05	1,03E-05	-7,09E-05	6,05E-05
	RPIM	-1,06E-07	-3,87E-05	1,44E-07	-8,69E-01	2,27E+00	1,06E+01	9,11E+00	2,63E-05	1,03E-05	-8,49E-05	7,30E-05
	Dif.	1,10E+00	1,30E-01	5,45E-01	1,64E-01	2,44E-01	1,88E-01	2,11E-01	3,70E-01	5,55E-03	1,98E-01	2,07E-01
15	FEM	9,92E-07	-3,34E-05	3,12E-07	1,02E+00	1,78E+00	8,70E+00	7,33E+00	1,87E-05	9,97E-06	-6,91E-05	5,90E-05
	RPIM	-1,47E-07	-3,77E-05	1,40E-07	-8,55E-01	2,22E+00	1,03E+01	8,87E+00	2,56E-05	1,00E-05	-8,27E-05	7,11E-05
	Dif.	1,15E+00	1,29E-01	5,52E-01	1,62E-01	2,43E-01	1,87E-01	2,10E-01	3,69E-01	4,47E-03	1,97E-01	2,06E-01
30	FEM	8,45E-07	-3,03E-05	2,87E-07	-9,30E-01	1,62E+00	7,89E+00	6,64E+00	1,69E-05	9,00E-06	-6,26E-05	5,35E-05
	RPIM	-1,78E-07	-3,42E-05	1,27E-07	-7,81E-01	2,01E+00	9,36E+00	8,03E+00	2,31E-05	9,03E-06	-7,48E-05	6,44E-05
	Dif.	1,21E+00	1,28E-01	5,59E-01	1,60E-01	2,42E-01	1,86E-01	2,09E-01	3,67E-01	3,25E-03	1,96E-01	2,04E-01
45	FEM	6,41E-07	-2,51E-05	2,42E-07	-7,76E-01	1,35E+00	6,54E+00	5,50E+00	1,40E-05	7,42E-06	-5,18E-05	4,43E-05
	RPIM	-1,97E-07	-2,83E-05	1,04E-07	-6,55E-01	1,67E+00	7,74E+00	6,64E+00	1,91E-05	7,44E-06	-6,19E-05	5,32E-05
	Dif.	1,31E+00	1,27E-01	5,68E-01	1,56E-01	2,40E-01	1,84E-01	2,08E-01	3,65E-01	1,63E-03	1,94E-01	2,03E-01
60	FEM	3,93E-07	-1,82E-05	1,81E-07	-5,70E-01	-9,86E-01	4,74E+00	3,98E+00	1,01E-05	5,34E-06	-3,76E-05	3,20E-05
	RPIM	-2,02E-07	-2,05E-05	7,54E-08	-4,83E-01	1,22E+00	5,60E+00	4,79E+00	1,37E-05	5,33E-06	-4,47E-05	3,85E-05
	Dif.	1,51E+00	1,25E-01	5,83E-01	1,51E-01	2,37E-01	1,82E-01	2,05E-01	3,62E-01	1,20E-03	1,92E-01	2,00E-01
75	FEM	1,18E-07	-1,01E-05	1,07E-07	-3,24E-01	-5,55E-01	2,62E+00	2,19E+00	5,53E-06	2,89E-06	-2,07E-05	1,77E-05
	RPIM	-1,94E-07	-1,13E-05	4,11E-08	-2,79E-01	-6,83E-01	3,08E+00	2,63E+00	7,48E-06	2,86E-06	-2,46E-05	2,11E-05
	Dif.	2,64E+00	1,20E-01	6,16E-01	1,38E-01	2,30E-01	1,76E-01	1,98E-01	3,52E-01	8,47E-03	1,85E-01	1,94E-01
90	FEM	-1,65E-07	-1,28E-06	2,62E-08	-3,98E-02	-8,58E-02	-3,38E-01	2,78E-01	7,68E-07	2,42E-07	-2,64E-06	2,25E-06
	RPIM	-1,72E-07	-1,34E-06	4,05E-09	-4,24E-02	-9,88E-02	-3,63E-01	2,96E-01	8,44E-07	2,00E-07	-2,82E-06	2,41E-06
	Dif.	4,53E-02	4,54E-02	8,45E-01	6,48E-02	1,52E-01	7,33E-02	6,53E-02	1,00E-01	1,74E-01	6,69E-02	6,79E-02

Visualizing Table 7, relative to point P1, the values obtained for FEM and RPIM are similar and the differences are very low around 5% - 10%, except for u_z , for which the values obtained with both methods are significantly different.

Relative to Table 8, for point P2, for u_z and σ_{11} the differences are relevant. For the other values, the differences between both techniques are about 15% - 20%.

Regarding to Table 9, for point P3, the differences are a slightly higher, around 15% - 30%. Notice that for u_x and u_z the differences between the FEM and RPIM are significant.

It is possible to visualize that the difference between both methodologies increases with the approach to the boundary conditions (the FEM and the meshless solution in nodes closer to the boundary conditions are significantly different).

Another fact is that for the load angle of 90°, the differences are usually much lesser than for the other angles.

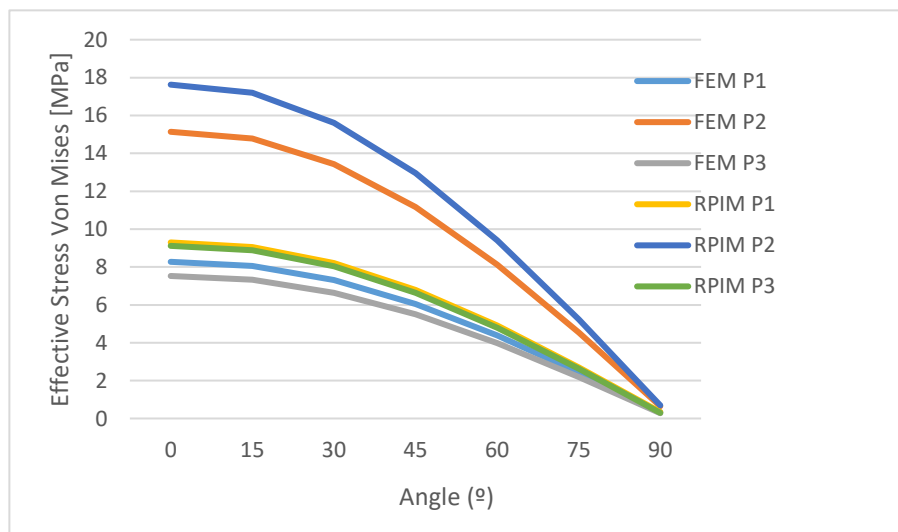
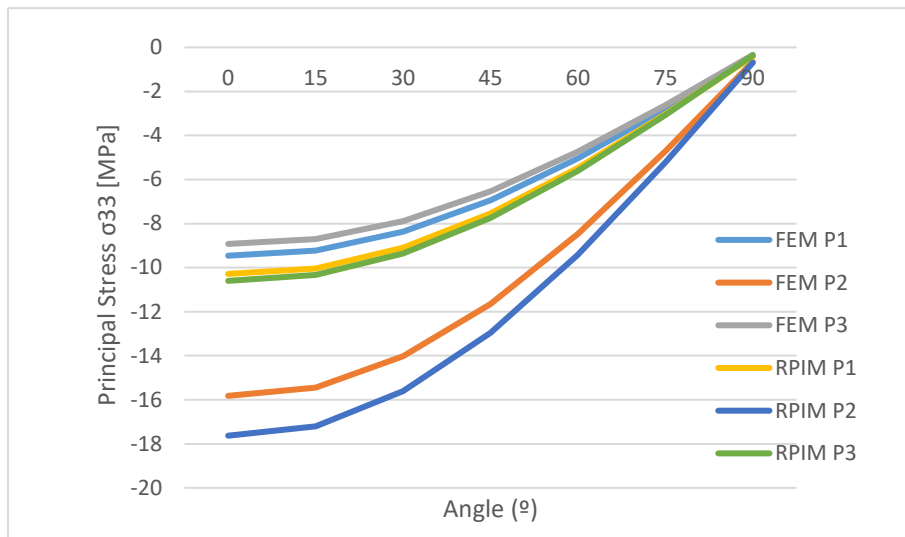
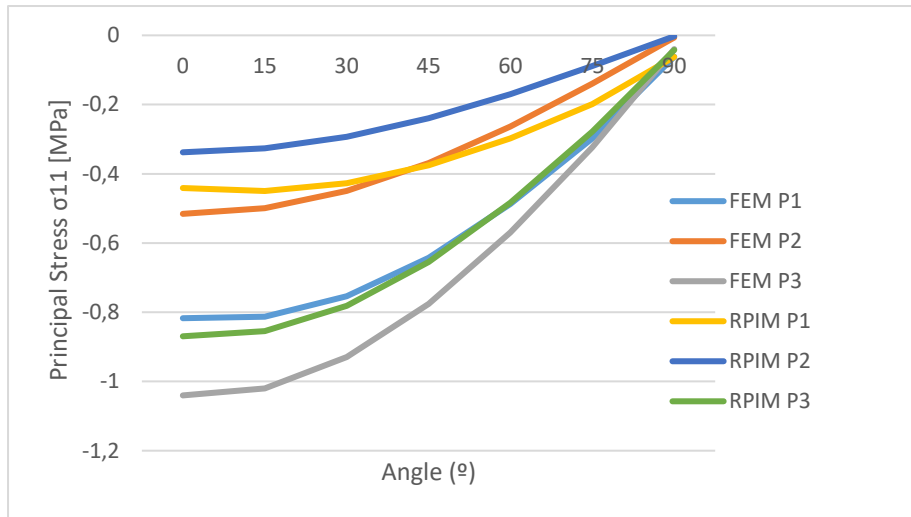


Figure 18: Principal Stress σ_{11} , Principal Stress σ_{33} and Effective Stress (Von Mises), respectively for MCA obtained with both numerical methods for distinct load angles

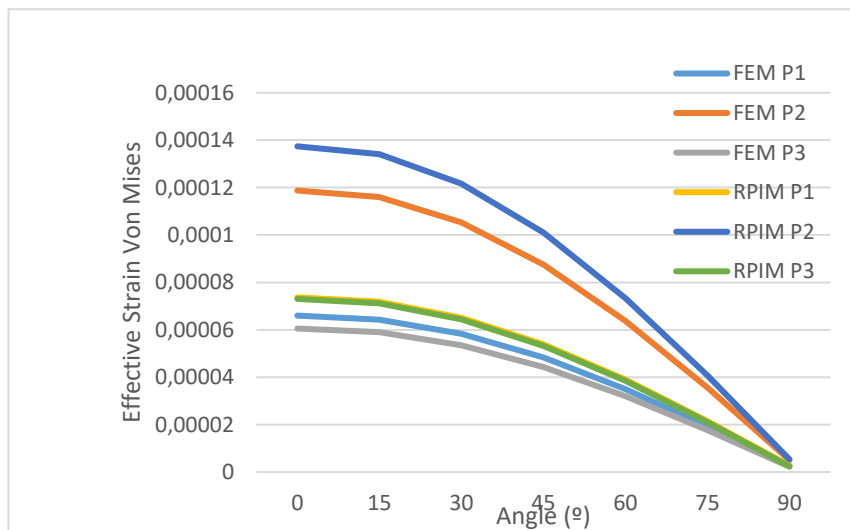
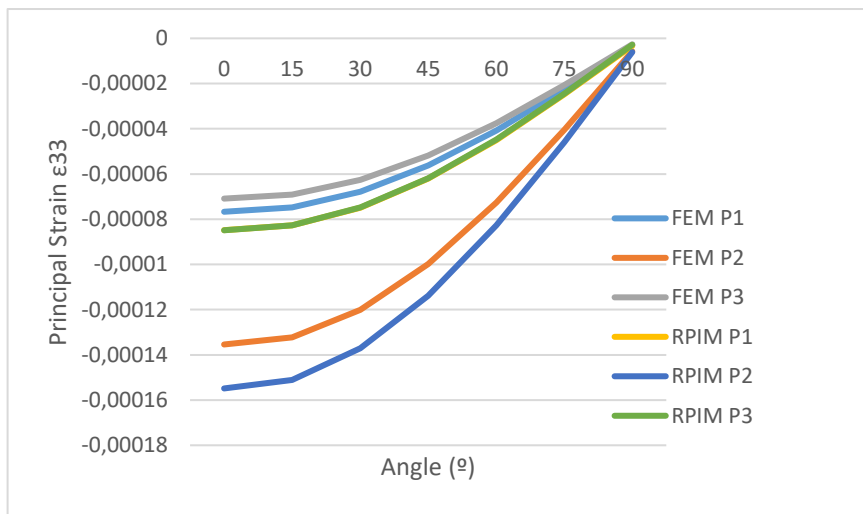
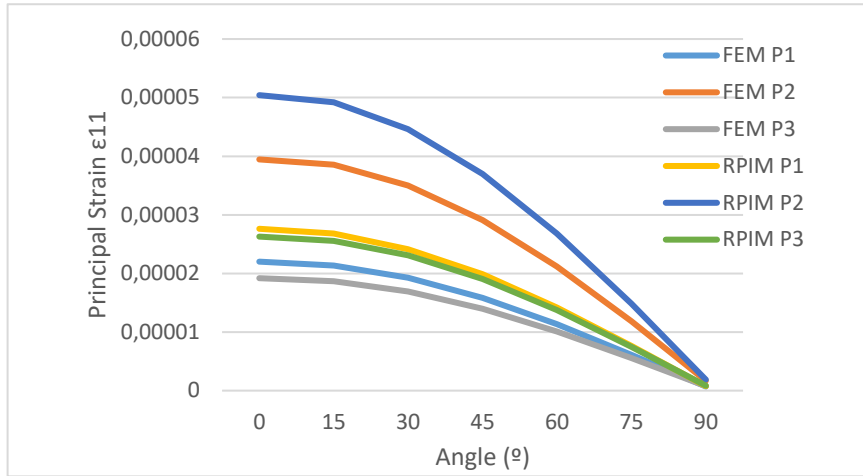


Figure 19: Principal Strain ϵ_{11} , Principal Strain ϵ_{33} and Effective Strain (Von Mises), respectively for MCA obtained with both numerical methods for distinct load angles

From the Figure 18 and Figure 19, it is possible to observe that in those graphics both FEM and RPIM follows the same trend and the values for the stresses and strain decreases with the increase of the load angle, which is expected because it is know that the shear loads are much more prejudicial than the axial loads.

Regarding the effective stress von Mises, the maximum value obtained was 18 MPa for 0° and around 0.5 MPa for 90° . Taking into account the masticatory forces ($Fv = 150 \text{ N}$ and $Fh = 15 \text{ N}$) and knowing that the yield stress of the commercial titanium used is 880 MPa, it is possible to observe that the implant will handle this force magnitudes since $18 \times 15 = 90 \text{ MPa}$ and $0.5 \times 150 = 75 \text{ MPa}$, which is much lower than 880 MPa.

Table 10: Stress distribution map on abutment for MCA. Effective stress (von Mises), principal stress σ_{11} and principal stress σ_{33} , respectively. [MPa]

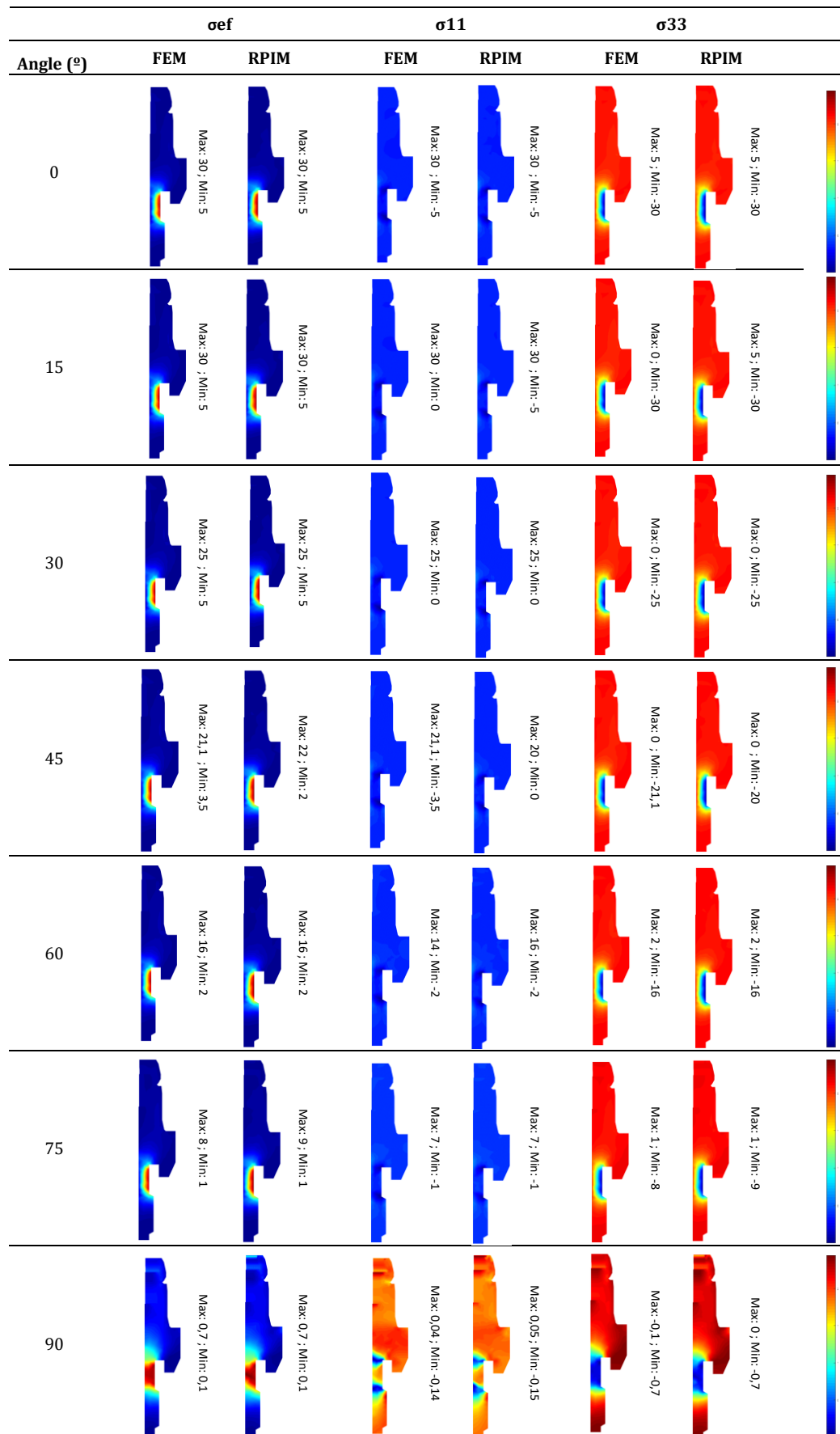


Table 11: Strain distribution map on abutment for MCA. Effective strain (von Mises), principal strain ϵ_{11} and principal strain ϵ_{33} , respectively.

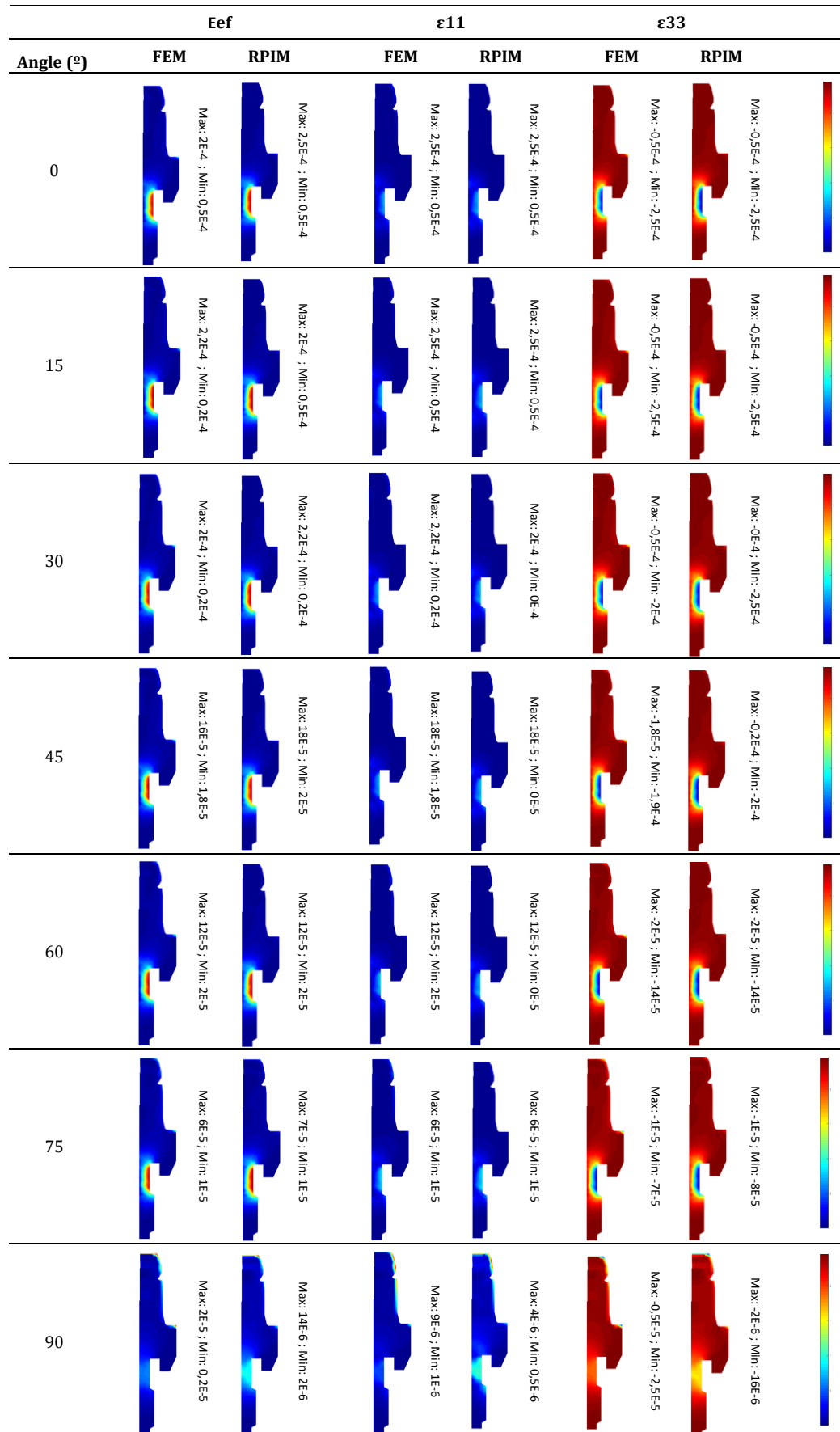


Table 12: Stress distribution map on nylon sleeve for MCA. Effective stress (von Mises), principal stress σ_{11} and principal stress σ_{33} , respectively. [MPa]

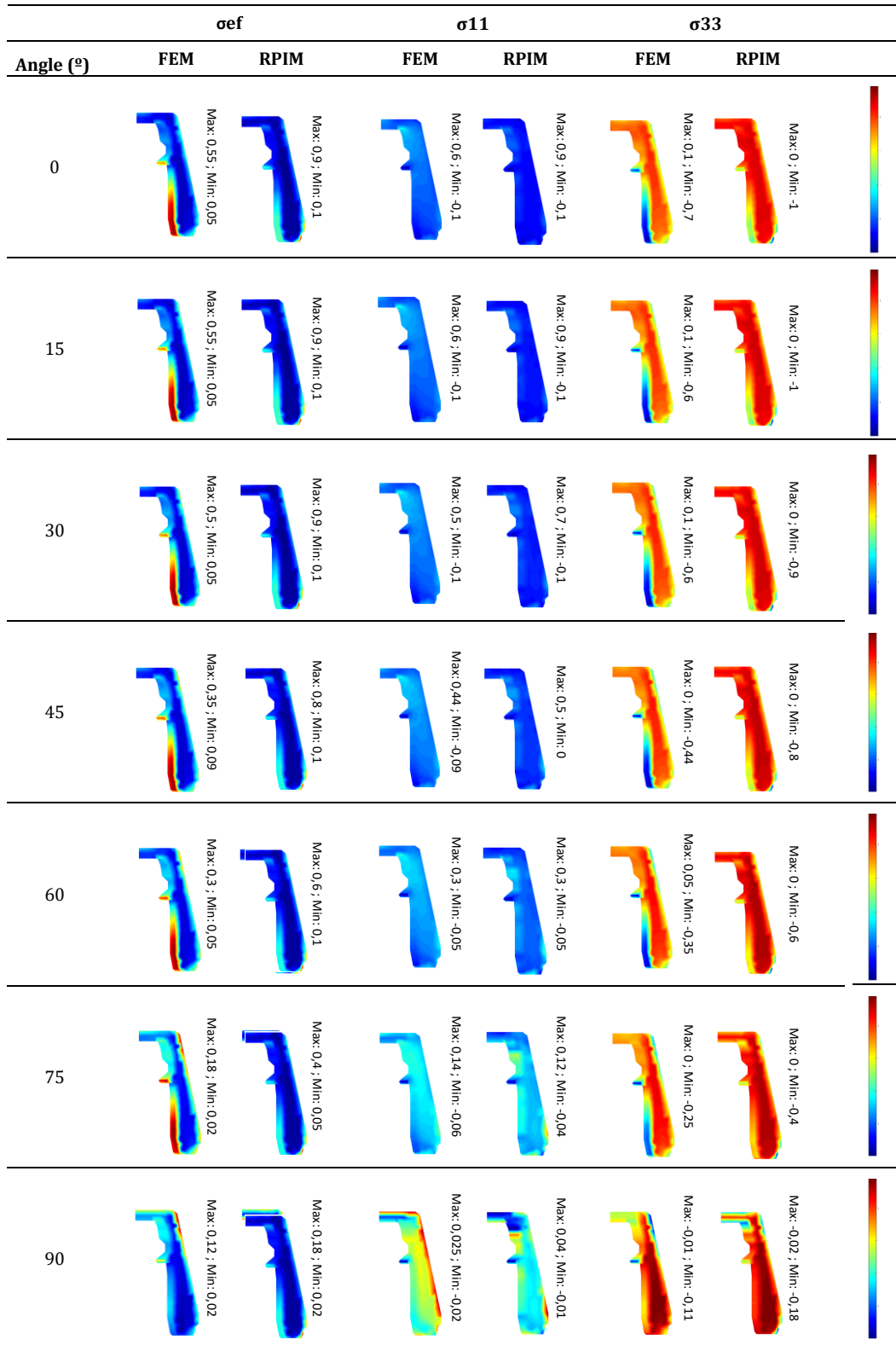


Table 13: Strain distribution map on nylon sleeve for MCA. Effective strain (von Mises), principal strain ϵ_{11} and principal strain ϵ_{33} , respectively.

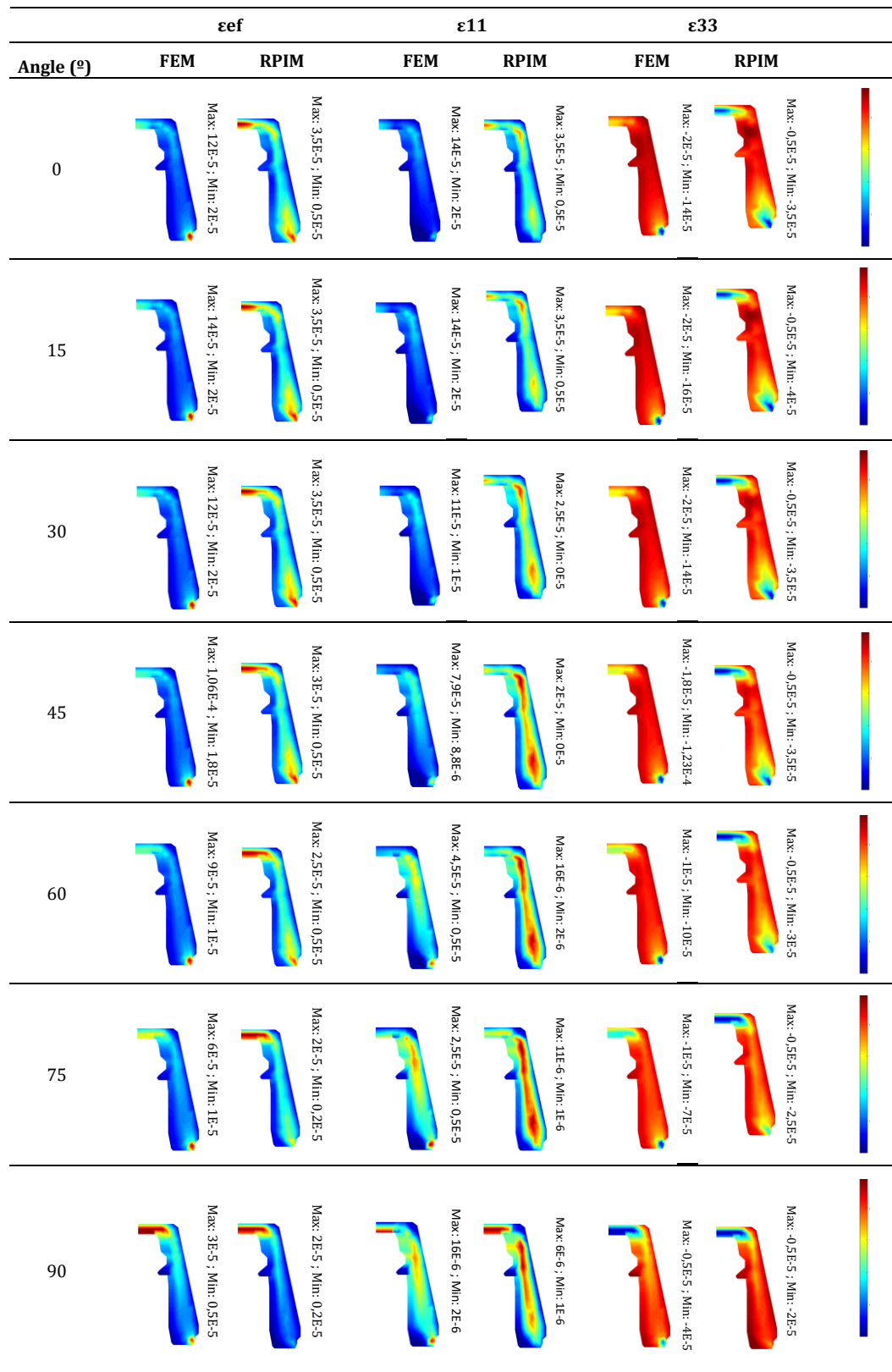


Table 14: Stress distribution map on titanium sleeve for MCA. Effective stress (von Mises), principal stress σ_{11} and principal stress σ_{33} , respectively. [MPa]

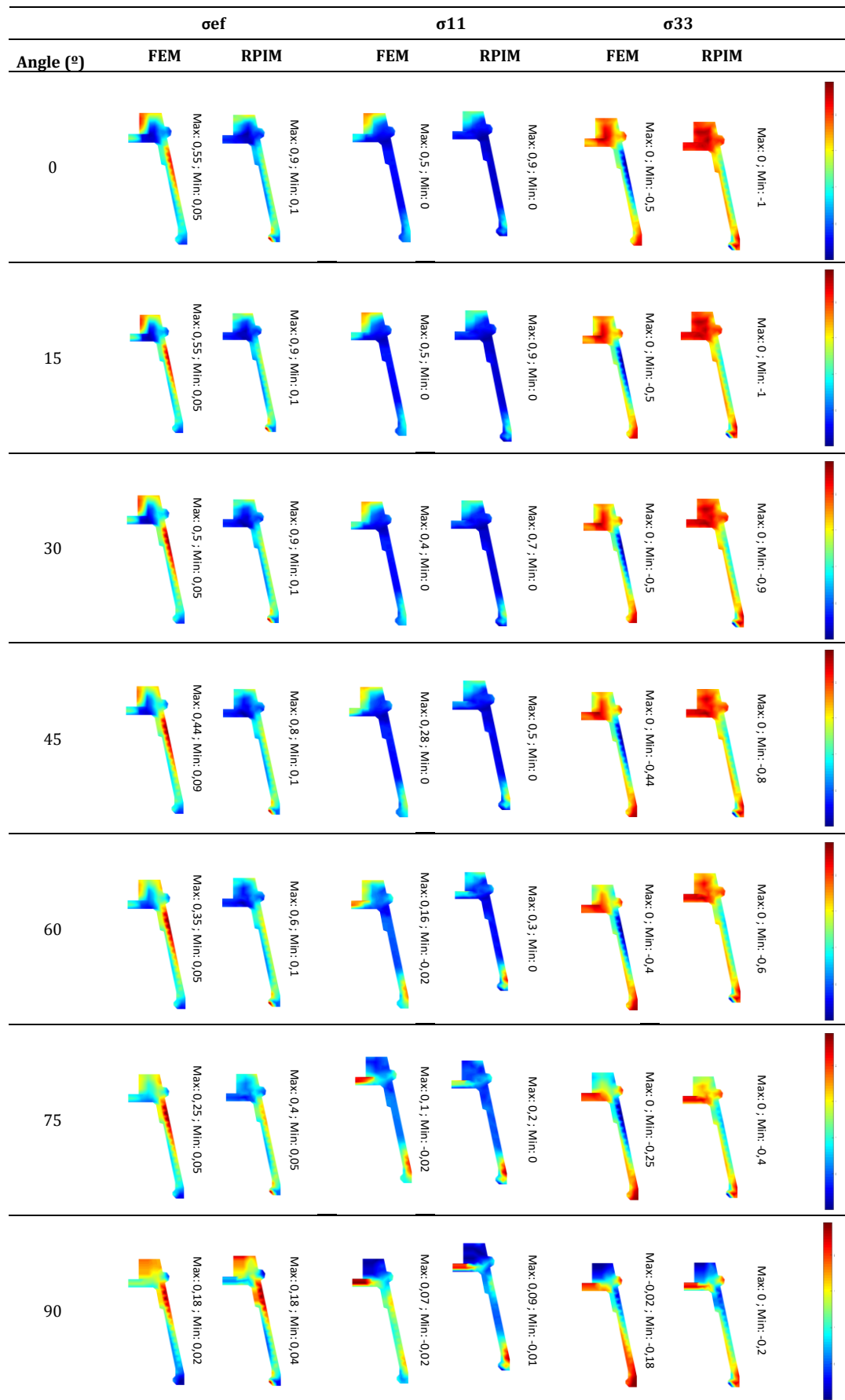
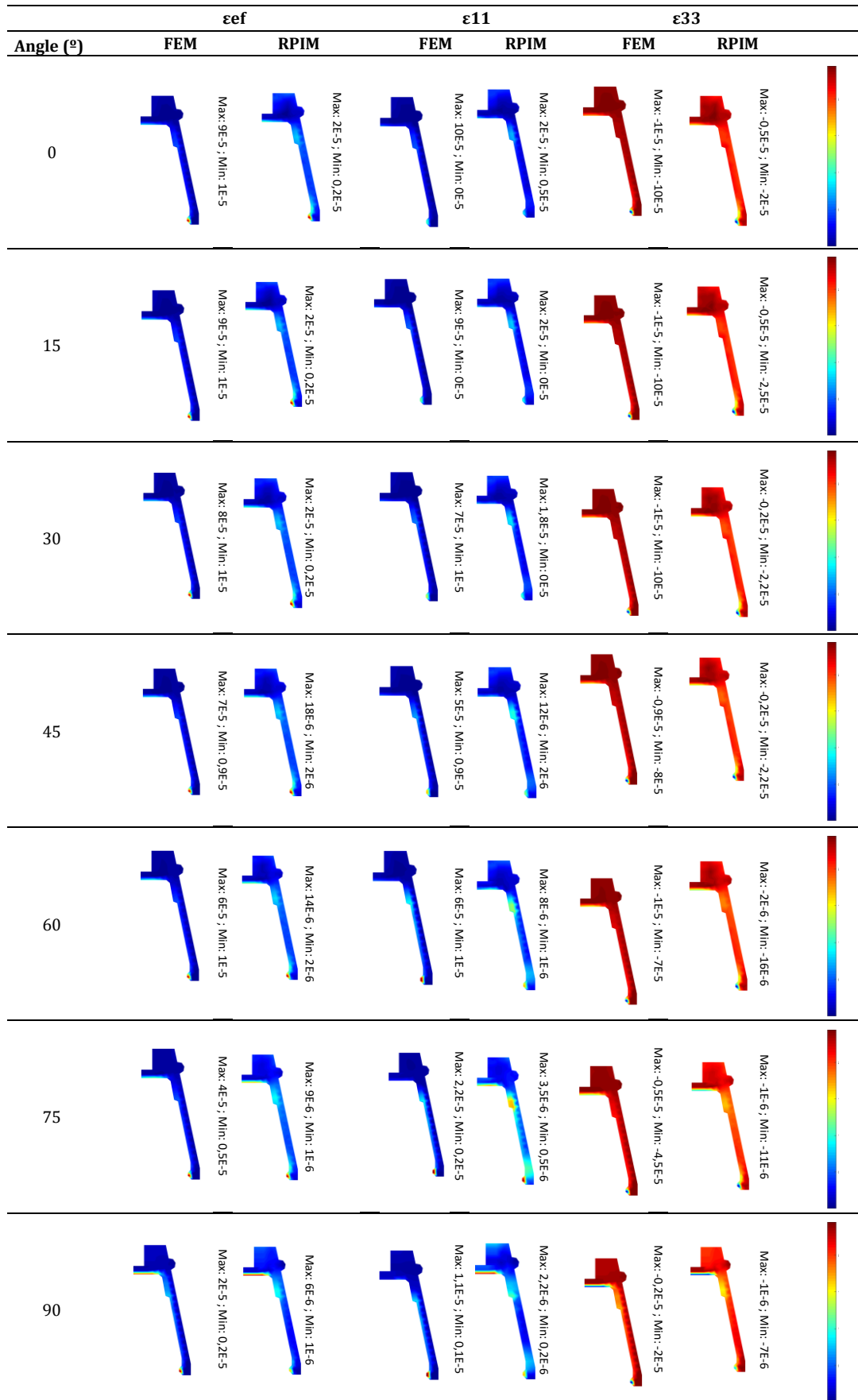


Table 15: Strain distribution map on titanium sleeve for MCA. Effective strain (von Mises), principal strain ϵ_{11} and principal strain ϵ_{33} , respectively



For the abutment, Table 10 and Table 11, it is seen that the most solicited part is right above the clamped. And again, that there is a decrease in both stress and strain values with the increase of the load angles.

Regarding the nylon sleeve and the titanium sleeve, the same observations can be made. Both FEM and RPIM values decrease with the increment of the applied load angle. Both methods predict high stresses in the upper part and high strains in the lower part.

6.2 Mechanical Case B

The second mechanical case (MCB) analysed considers the seven forces described in Table 6 and the boundary condition (2), shown in Figure 16. In order to understand the effect of the load orientation in the dental implant, three interest points were selected in the interior of the domain, Figure 20. From these points were obtained the local displacements, stresses and strains.

Regarding interest point P4, it is possible to observe the measured local displacements, stresses and strains in Table 16. For point P5, it is possible to observe the measured local displacements, stresses and strains in Table 17. And concerning the interest point P6, the measured local displacements, stresses and strains are presented in Table 18.

To clarify the results of MCB shown in the Table 16, Table 17 and Table 18, auxiliary charts are presented showing the variation of the stress and strain, respectively, at the interest points on study for both numerical methods (FEM and RPIM) for the distinct load angles. The charts are presented in Figure 21 and Figure 22.

Furthermore, to show the stress and strain field in the complete domain, stress and strain maps are presented, respectively, for the three distinct parts that constitute the dental implant, allowing to visually compare the RPIM and FEM solutions for distinct load angles. For the abutment, visualize Table 19 and Table 20. For the nylon sleeve, observe Table 21 and Table 22. Lastly, to the titanium sleeve, see Table 23 and Table 24.

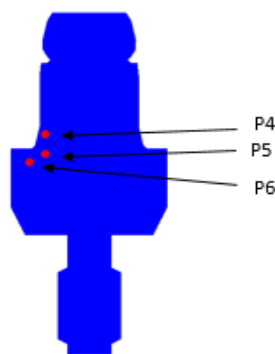


Figure 20: Interest points for analysis on MCB

Table 16: Obtained values for point 4 with both numerical methods, with respect to the angle of the applied load.

Angle	Method	ux	uy	uz	σ_1	σ_2	σ_3	σ_{ef}	ϵ_1	ϵ_2	ϵ_3	ϵ_{ef}
0	FEM	-1,21E-05	-1,35E-05	1,20E-07	-4,79E-02	-1,63E-01	1,08E+00	9,79E-01	2,85E-06	1,54E-06	-8,93E-06	7,76E-06
	RPIM	-9,73E-06	-9,77E-06	1,10E-07	-3,60E-02	-1,11E-01	-7,23E-01	6,52E-01	1,88E-06	1,02E-06	-5,96E-06	5,17E-06
	Dif.	1,98E-01	2,76E-01	8,21E-02	2,50E-01	3,16E-01	3,31E-01	3,34E-01	3,40E-01	3,38E-01	3,32E-01	3,33E-01
15	FEM	-1,18E-05	-1,35E-05	1,20E-07	-4,85E-02	-1,62E-01	1,07E+00	9,68E-01	2,82E-06	1,52E-06	-8,83E-06	7,67E-06
	RPIM	-9,44E-06	-9,76E-06	1,15E-07	-3,62E-02	-1,11E-01	-7,17E-01	6,47E-01	1,86E-06	1,01E-06	-5,91E-06	5,13E-06
	Dif.	1,97E-01	2,75E-01	4,73E-02	2,55E-01	3,17E-01	3,29E-01	3,31E-01	3,38E-01	3,33E-01	3,30E-01	3,31E-01
30	FEM	-1,06E-05	-1,25E-05	1,13E-07	-4,58E-02	-1,50E-01	-9,83E-01	8,90E-01	2,59E-06	1,39E-06	-8,12E-06	7,05E-06
	RPIM	-8,50E-06	-9,09E-06	1,11E-07	-3,39E-02	-1,02E-01	-6,62E-01	5,97E-01	1,72E-06	9,36E-07	-5,46E-06	4,74E-06
	Dif.	1,97E-01	2,73E-01	1,04E-02	2,60E-01	3,19E-01	3,26E-01	3,29E-01	3,35E-01	3,28E-01	3,28E-01	3,28E-01
45	FEM	-8,68E-06	-1,07E-05	9,72E-08	-3,99E-02	-1,28E-01	-8,32E-01	7,52E-01	2,18E-06	1,17E-06	-6,87E-06	5,96E-06
	RPIM	-6,98E-06	-7,79E-06	1,01E-07	-2,93E-02	-8,72E-02	-5,63E-01	5,07E-01	1,46E-06	7,95E-07	-4,64E-06	4,02E-06
	Dif.	1,96E-01	2,71E-01	3,54E-02	2,67E-01	3,21E-01	3,24E-01	3,25E-01	3,32E-01	3,21E-01	3,25E-01	3,25E-01
60	FEM	-6,19E-06	-8,15E-06	7,52E-08	-3,13E-02	-9,76E-02	-6,24E-01	5,62E-01	1,63E-06	8,69E-07	-5,14E-06	4,46E-06
	RPIM	-4,98E-06	-5,97E-06	8,30E-08	-2,27E-02	-6,60E-02	-4,25E-01	3,82E-01	1,09E-06	5,99E-07	-3,50E-06	3,03E-06
	Dif.	1,95E-01	2,68E-01	1,04E-01	2,76E-01	3,24E-01	3,19E-01	3,20E-01	3,27E-01	3,10E-01	3,20E-01	3,20E-01
75	FEM	-3,28E-06	-5,06E-06	4,80E-08	-2,05E-02	-6,02E-02	-3,73E-01	3,34E-01	9,62E-07	5,08E-07	-3,06E-06	2,66E-06
	RPIM	-2,71E-06	-3,82E-06	6,11E-08	-1,48E-02	-4,12E-02	-2,64E-01	2,37E-01	6,73E-07	3,71E-07	-2,17E-06	1,88E-06
	Dif.	1,74E-01	2,45E-01	2,71E-01	2,77E-01	3,15E-01	2,93E-01	2,92E-01	3,00E-01	2,69E-01	2,93E-01	2,93E-01
90	FEM	-1,42E-07	-1,62E-06	1,76E-08	-7,96E-03	-1,87E-02	-9,71E-02	8,43E-02	2,35E-07	1,12E-07	-7,83E-07	6,74E-07
	RPIM	-1,36E-07	-1,27E-06	3,30E-08	-5,41E-03	-1,21E-02	-7,47E-02	6,62E-02	1,81E-07	1,04E-07	-6,10E-07	5,27E-07
	Dif.	4,81E-02	2,14E-01	8,77E-01	3,20E-01	3,51E-01	2,31E-01	2,15E-01	2,30E-01	7,19E-02	2,21E-01	2,19E-01

Table 17: Obtained values for point 5 with both numerical methods, with respect to the angle of the applied load.

Angle	Method	ux	uy	uz	σ_1	σ_2	σ_3	σ_{ef}	ϵ_1	ϵ_2	ϵ_3	ϵ_{ef}
0	FEM	-1,63E-06	-6,99E-06	-7,72E-08	-3,00E-01	-3,17E-01	-9,15E-01	6,07E-01	6,09E-07	4,18E-07	-6,41E-06	5,27E-06
	RPIM	-1,55E-06	-5,11E-06	9,59E-09	-1,83E-01	-2,04E-01	-6,37E-01	4,44E-01	6,07E-07	3,71E-07	-4,58E-06	3,78E-06
	Dif.	4,88E-02	2,70E-01	1,12E+00	3,90E-01	3,57E-01	3,04E-01	2,68E-01	4,58E-03	1,13E-01	2,86E-01	2,83E-01
15	FEM	-1,57E-06	-7,01E-06	-7,64E-08	-2,97E-01	-3,15E-01	-9,05E-01	5,99E-01	6,04E-07	4,04E-07	-6,34E-06	5,21E-06
	RPIM	-1,50E-06	-5,12E-06	1,20E-08	-1,81E-01	-2,03E-01	-6,31E-01	4,40E-01	6,10E-07	3,57E-07	-4,53E-06	3,75E-06
	Dif.	4,68E-02	2,69E-01	1,16E+00	3,92E-01	3,55E-01	3,03E-01	2,67E-01	1,08E-02	1,18E-01	2,85E-01	2,81E-01
30	FEM	-1,40E-06	-6,56E-06	-7,05E-08	-2,74E-01	-2,91E-01	-8,34E-01	5,52E-01	5,58E-07	3,62E-07	-5,84E-06	4,80E-06
	RPIM	-1,34E-06	-4,79E-06	1,37E-08	-1,66E-01	-1,88E-01	-5,82E-01	4,05E-01	5,72E-07	3,18E-07	-4,18E-06	3,45E-06
	Dif.	4,43E-02	2,69E-01	1,19E+00	3,95E-01	3,54E-01	3,02E-01	2,65E-01	2,51E-02	1,20E-01	2,84E-01	2,80E-01
45	FEM	-1,13E-06	-5,65E-06	-5,97E-08	-2,32E-01	-2,48E-01	-7,06E-01	4,66E-01	4,77E-07	2,93E-07	-4,94E-06	4,06E-06
	RPIM	-1,09E-06	-4,13E-06	1,44E-08	-1,40E-01	-1,60E-01	-4,93E-01	3,44E-01	4,96E-07	2,58E-07	-3,54E-06	2,93E-06
	Dif.	4,09E-02	2,69E-01	1,24E+00	3,97E-01	3,53E-01	3,01E-01	2,63E-01	4,00E-02	1,19E-01	2,82E-01	2,78E-01
60	FEM	-7,89E-07	-4,36E-06	-4,49E-08	-1,74E-01	-1,88E-01	-5,29E-01	3,49E-01	3,64E-07	2,03E-07	-3,70E-06	3,04E-06
	RPIM	-7,62E-07	-3,19E-06	1,41E-08	-1,04E-01	-1,22E-01	-3,71E-01	2,58E-01	3,85E-07	1,81E-07	-2,66E-06	2,20E-06
	Dif.	3,50E-02	2,69E-01	1,31E+00	4,01E-01	3,51E-01	2,99E-01	2,59E-01	5,77E-02	1,10E-01	2,80E-01	2,75E-01
75	FEM	-3,93E-07	-2,78E-06	-2,70E-08	-1,03E-01	-1,15E-01	-3,17E-01	2,08E-01	2,30E-07	9,60E-08	-2,21E-06	1,81E-06
	RPIM	-3,95E-07	-2,08E-06	1,31E-08	-6,26E-02	-7,68E-02	-2,28E-01	1,59E-01	2,54E-07	9,26E-08	-1,64E-06	1,36E-06
	Dif.	4,76E-03	2,51E-01	1,49E+00	3,95E-01	3,33E-01	2,79E-01	2,34E-01	1,07E-01	3,51E-02	2,57E-01	2,52E-01
90	FEM	3,09E-08	-9,99E-07	-7,22E-09	-2,57E-02	-3,51E-02	-8,28E-02	5,31E-02	8,54E-08	-2,25E-08	-5,68E-07	4,69E-07
	RPIM	1,71E-08	-7,51E-07	1,10E-08	-1,45E-02	-2,36E-02	-6,18E-02	4,35E-02	9,75E-08	-6,17E-09	-4,43E-07	3,70E-07
	Dif.	4,46E-01	2,48E-01	2,52E+00	4,33E-01	3,27E-01	2,53E-01	1,81E-01	1,41E-01	7,26E-01	2,20E-01	2,11E-01

Table 18: Obtained values for point 6 with both numerical methods, with respect to the angle of the applied load.

Angle	Method	ux	uy	uz	σ_1	σ_2	σ_3	σ_{ef}	ϵ_1	ϵ_2	ϵ_3	ϵ_{ef}
0	FEM	-7,91E-07	-2,84E-06	3,85E-08	-1,03E-02	-1,45E-01	-5,93E-01	5,29E-01	1,85E-06	3,20E-07	-4,80E-06	4,21E-06
	RPIM	-4,35E-07	-1,69E-06	6,60E-08	-1,38E-01	-1,44E-01	-4,15E-01	2,74E-01	2,60E-07	1,91E-07	-2,90E-06	2,38E-06
	Dif.	4,51E-01	4,03E-01	7,12E-01	1,24E+01	3,11E-03	3,01E-01	4,82E-01	8,60E-01	4,04E-01	3,96E-01	4,34E-01
15	FEM	-7,70E-07	-2,84E-06	3,75E-08	-8,00E-03	-1,43E-01	-5,87E-01	5,25E-01	1,85E-06	3,10E-07	-4,76E-06	4,18E-06
	RPIM	-4,17E-07	-1,69E-06	6,67E-08	-1,38E-01	-1,44E-01	-4,11E-01	2,70E-01	2,50E-07	1,82E-07	-2,87E-06	2,36E-06
	Dif.	4,59E-01	4,04E-01	7,78E-01	1,62E+01	5,34E-03	3,00E-01	4,85E-01	8,65E-01	4,11E-01	3,97E-01	4,36E-01
30	FEM	-6,97E-07	-2,65E-06	3,40E-08	-5,14E-03	-1,32E-01	-5,41E-01	4,85E-01	1,73E-06	2,79E-07	-4,39E-06	3,86E-06
	RPIM	-3,70E-07	-1,58E-06	6,29E-08	-1,29E-01	-1,34E-01	-3,79E-01	2,48E-01	2,23E-07	1,62E-07	-2,64E-06	2,17E-06
	Dif.	4,68E-01	4,05E-01	8,52E-01	2,40E+01	1,48E-02	2,99E-01	4,88E-01	8,71E-01	4,21E-01	3,98E-01	4,38E-01
45	FEM	-5,75E-07	-2,28E-06	2,81E-08	-1,91E-03	-1,12E-01	-4,58E-01	4,12E-01	1,48E-06	2,29E-07	-3,72E-06	3,28E-06
	RPIM	-2,99E-07	-1,35E-06	5,48E-08	-1,10E-01	-1,15E-01	-3,22E-01	2,09E-01	1,82E-07	1,29E-07	-2,23E-06	1,83E-06
	Dif.	4,81E-01	4,06E-01	9,52E-01	5,66E+01	2,71E-02	2,97E-01	4,92E-01	8,77E-01	4,35E-01	4,00E-01	4,41E-01
60	FEM	-4,15E-07	-1,75E-06	2,03E-08	1,47E-03	-8,40E-02	-3,44E-01	3,11E-01	1,14E-06	1,63E-07	-2,80E-06	2,47E-06
	RPIM	-2,07E-07	-1,04E-06	4,30E-08	-8,43E-02	-8,80E-02	-2,42E-01	1,56E-01	1,30E-07	8,77E-08	-1,67E-06	1,37E-06
	Dif.	5,02E-01	4,08E-01	1,12E+00	5,83E+01	4,72E-02	2,95E-01	4,98E-01	8,86E-01	4,63E-01	4,02E-01	4,45E-01
75	FEM	-2,27E-07	-1,10E-06	1,11E-08	4,82E-03	-5,05E-02	-2,06E-01	1,89E-01	7,19E-07	8,68E-08	-1,69E-06	1,50E-06
	RPIM	-1,03E-07	-6,65E-07	2,89E-08	-5,35E-02	-5,64E-02	-1,50E-01	9,50E-02	7,40E-08	4,02E-08	-1,03E-06	8,42E-07
	Dif.	5,45E-01	3,98E-01	1,60E+00	1,21E+01	1,18E-01	2,72E-01	4,98E-01	8,97E-01	5,36E-01	3,92E-01	4,39E-01
90	FEM	-2,25E-08	-3,82E-07	1,17E-09	8,31E-03	-1,35E-02	-5,48E-02	5,56E-02	2,53E-07	4,32E-09	-4,68E-07	4,35E-07
	RPIM	1,24E-08	-2,24E-07	1,18E-08	-1,55E-02	-1,89E-02	-4,35E-02	2,65E-02	2,83E-08	-1,04E-08	-2,92E-07	2,39E-07
	Dif.	1,55E+00	4,14E-01	9,07E+00	2,86E+00	4,01E-01	2,07E-01	5,23E-01	8,88E-01	3,40E+00	3,77E-01	4,49E-01

From Table 16, relative to point P4, all the differences between the numerical methods in study are around 10% - 30%. The exception is the u_z value obtained with the angle 90°.

Concerning Table 17, for point P5, the differences are between 20% - 30%. However, for principal stress σ_{11} and principal strain ϵ_{11} the values for FEM and RPIM are much more closer. On the other hand, for u_z the difference for both numerical methods are significant.

Regarding Table 18, for point P6 (localized almost inside the clamped part), the differences are much higher than for the previous points, being around 40-50%. The principal stress σ_{22} is the only value which the values for both methods are similar. Although, for u_z , σ_{11} and ϵ_{11} the differences are very high.

Again, the closer the points are from the boundary condition, the differences between both numerical methods increase.

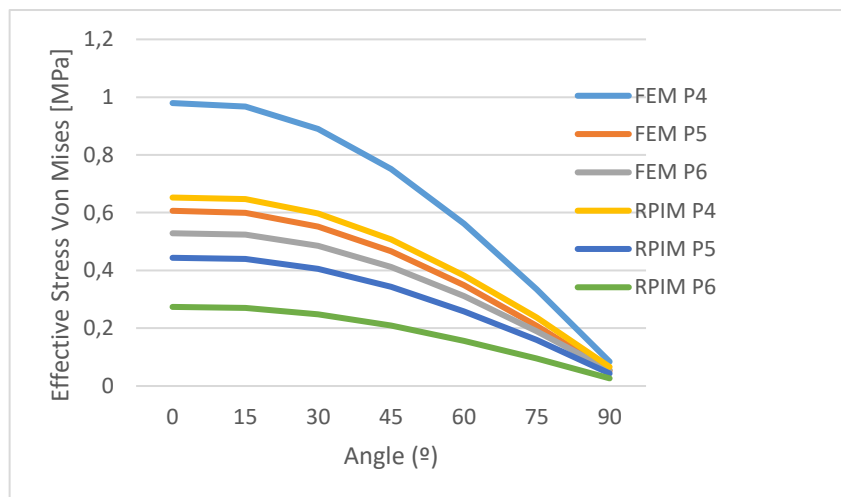
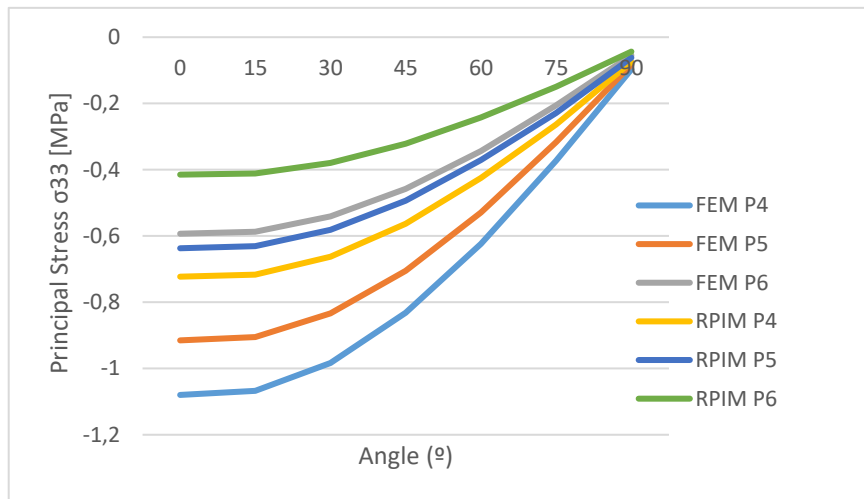
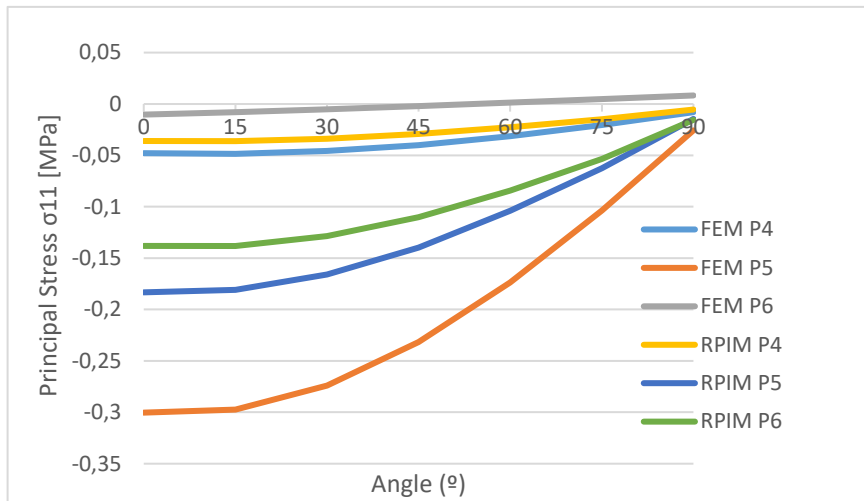


Figure 21: Principal Stress σ_{11} , Principal Stress σ_{33} and Effective Stress (von Mises), respectively for MCB obtained with both numerical methods for distinct load angles

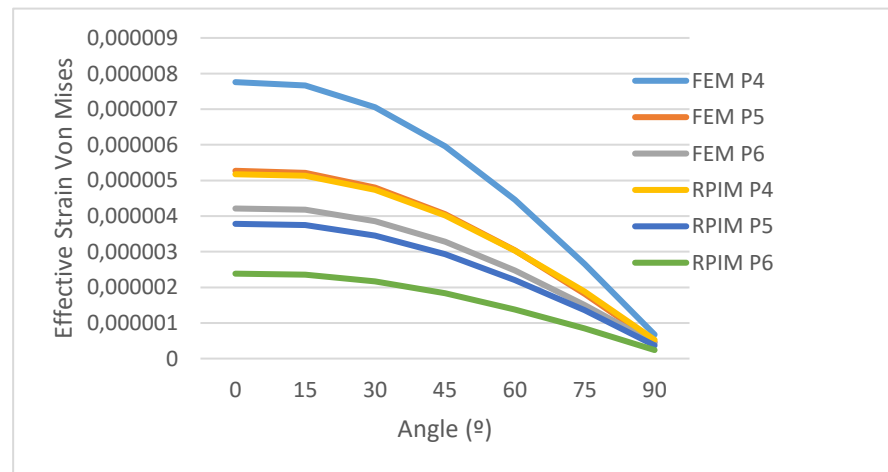
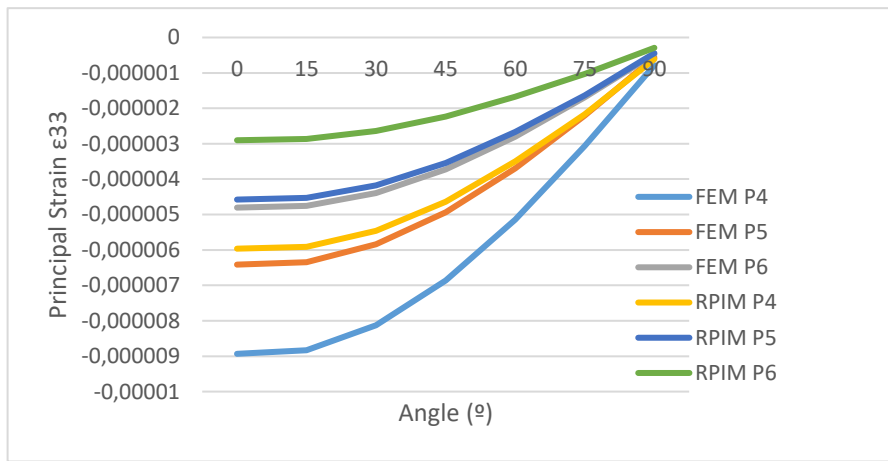
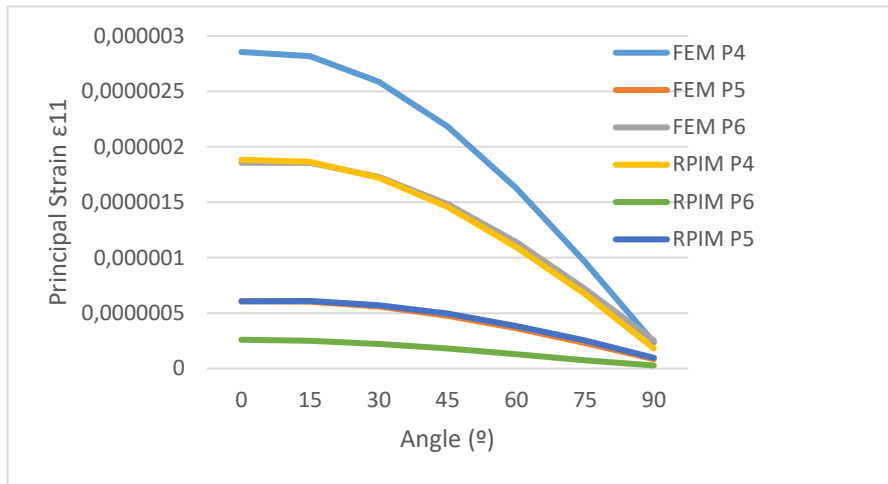


Figure 22: Principal Strain ϵ_{11} , Principal Strain ϵ_{33} and Effective Strain (von Mises), respectively for MCB obtained with both numerical methods for distinct load angles

From the graphics, Figure 21 and Figure 22, for both compared numerical methods, the values for stresses and strains follow the same trend, decreasing with the increase of the load angle, which is expected because it is known that the shear loads are much more prejudicial than the axial loads.

From the effective stress von Mises the maximum value obtained was 1 MPa for 0° and around 0.05 MPa for 90° . Taking into account the masticatory forces ($F_v = 150 \text{ N}$ and $F_h = 15 \text{ N}$) and knowing that the yield stress of the commercial titanium used is 880 MPa, it is possible to observe that the implant will handle this forces since $1 \times 15 = 15 \text{ MPa}$ and $0.05 \times 150 = 7,5 \text{ MPa}$.

Table 19: Stress distribution map on abutment for MCB. Effective stress (Von Mises), principal stress σ_{11} and principal stress σ_{33} , respectively. [MPa]

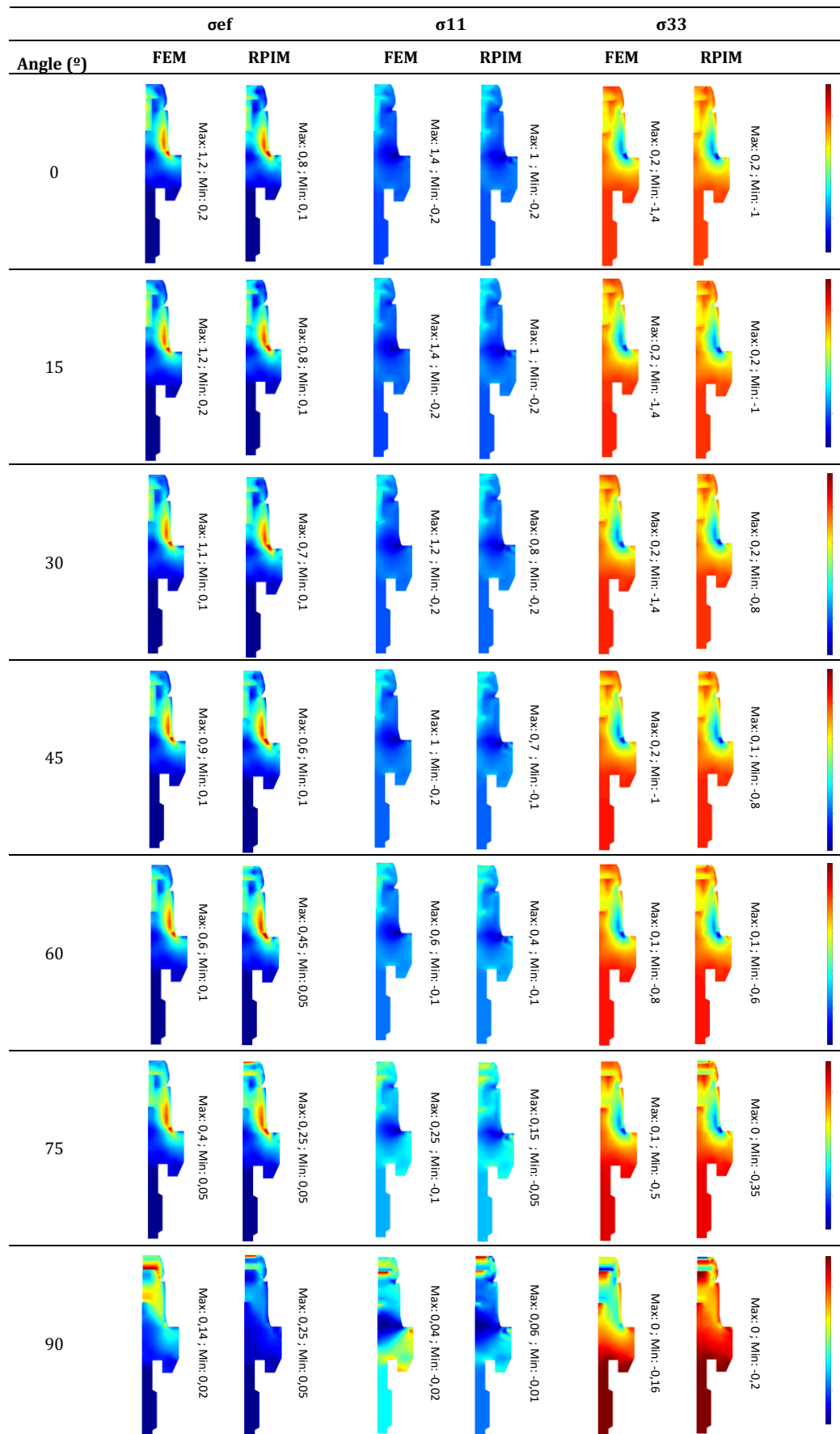


Table 20: Strain distribution map on abutment for MCB. Effective strain (Von Mises), principal strain ϵ_{11} and principal strain ϵ_{33} , respectively.

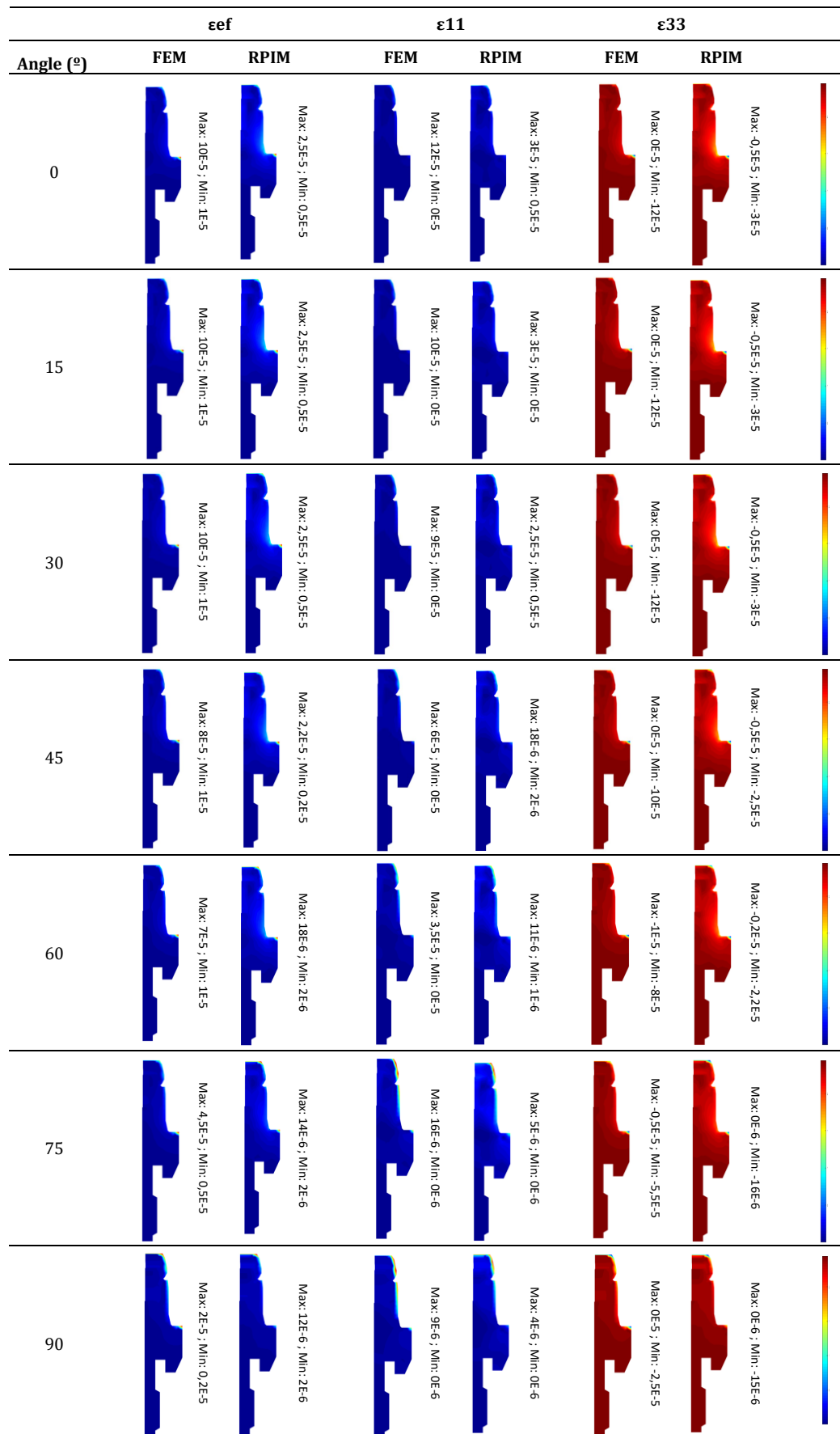


Table 21: Stress distribution map on nylon sleeve for MCB. Effective stress (Von Mises), principal stress σ_{11} and principal stress σ_{33} , respectively. [MPa]

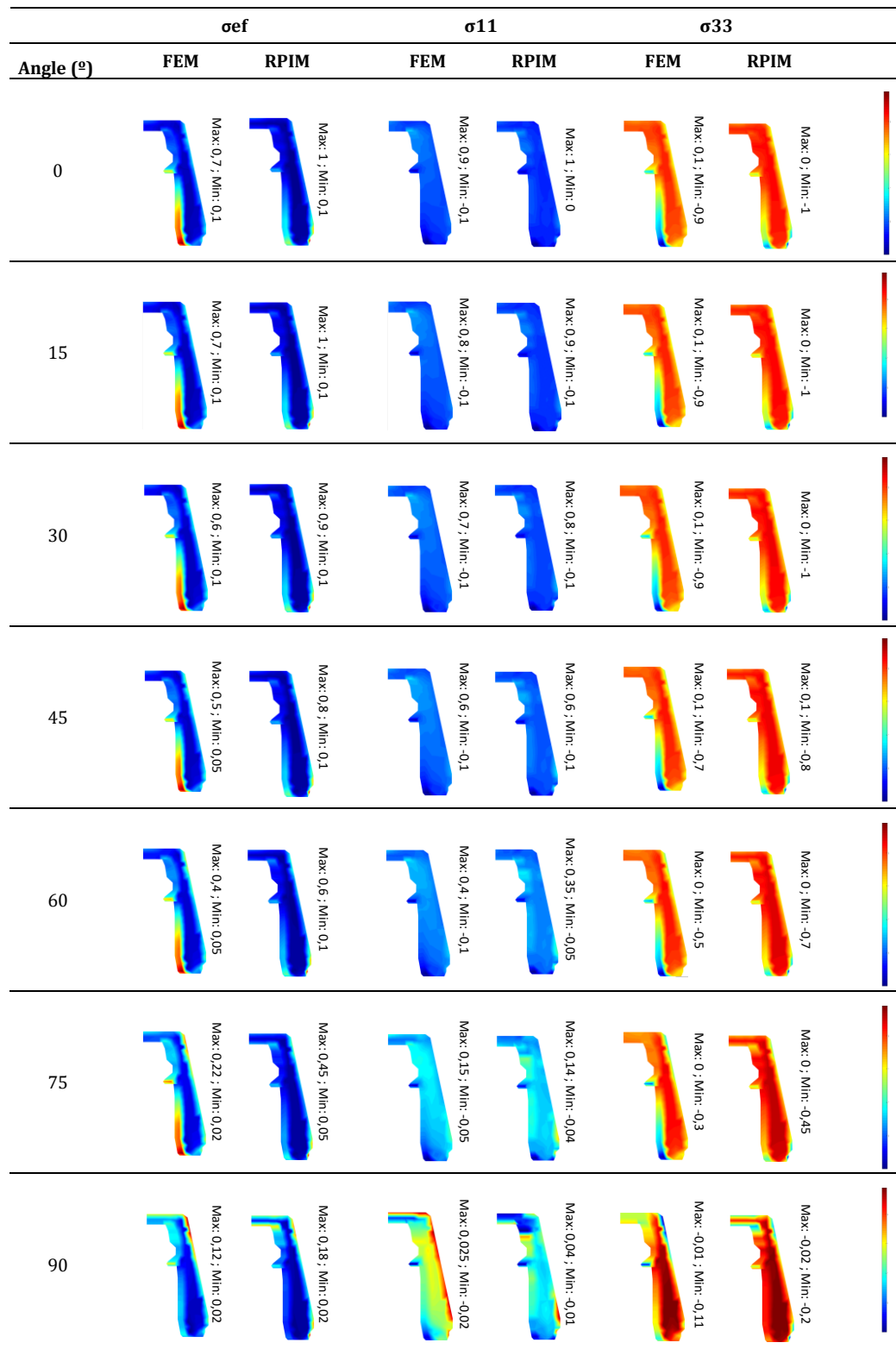


Table 22: Strain distribution map on nylon sleeve for MCB. Effective strain (Von Mises), principal strain ϵ_{11} and principal strain ϵ_{33} , respectively.

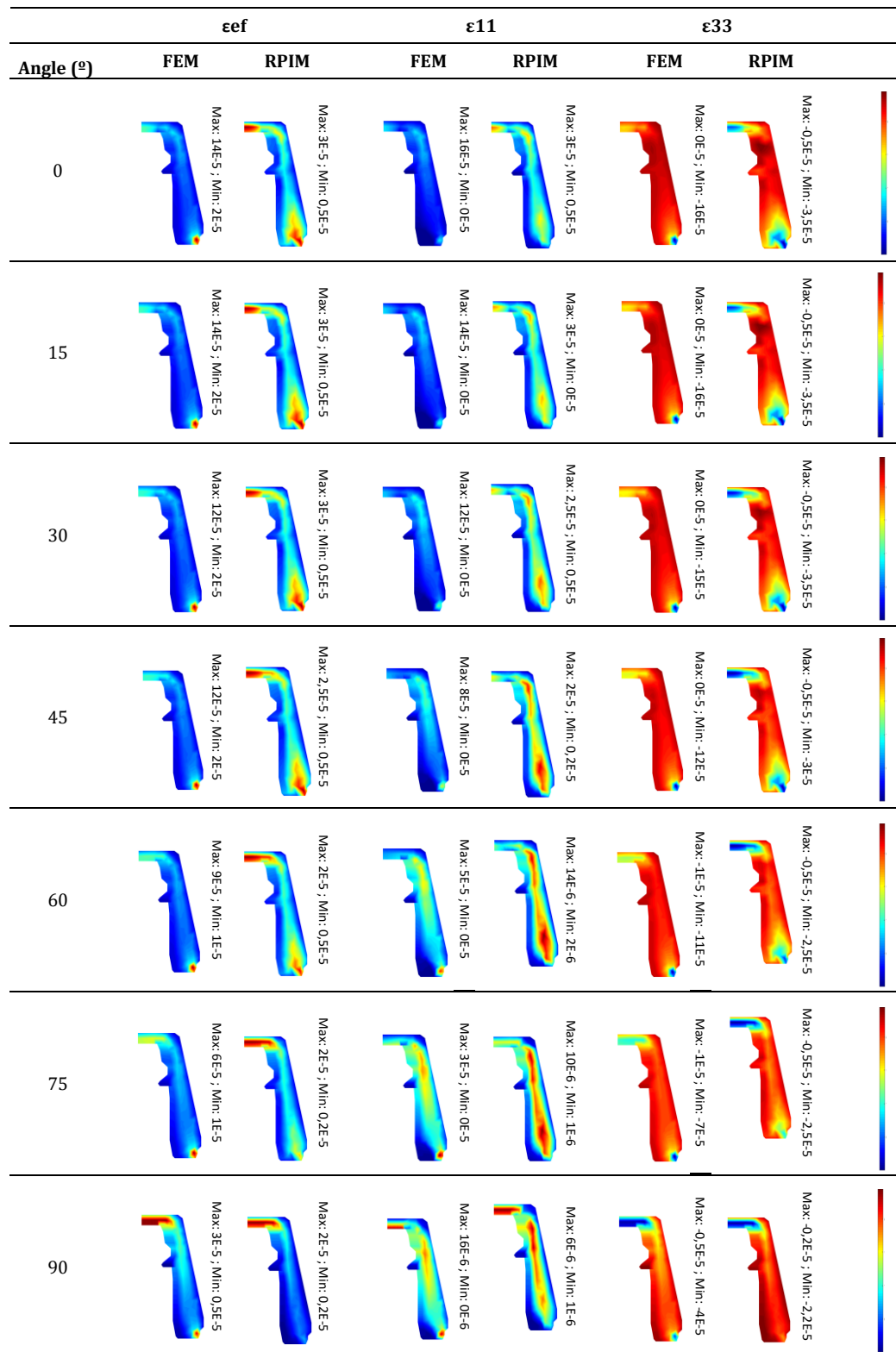


Table 23: Stress distribution map on titanium sleeve for MCB. Effective stress (Von Mises), principal stress σ_{11} and principal stress σ_{33} , respectively. [MPa].

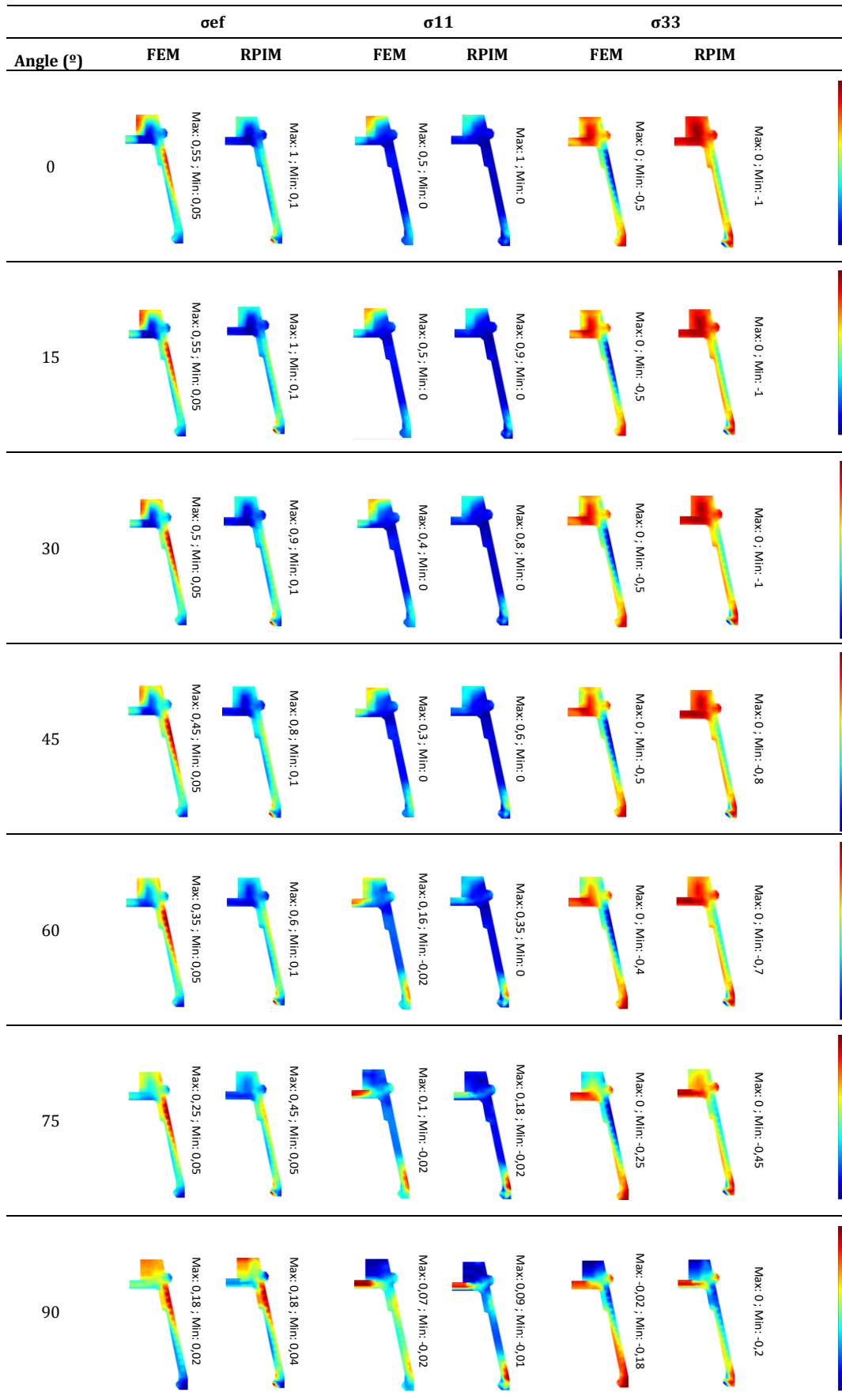
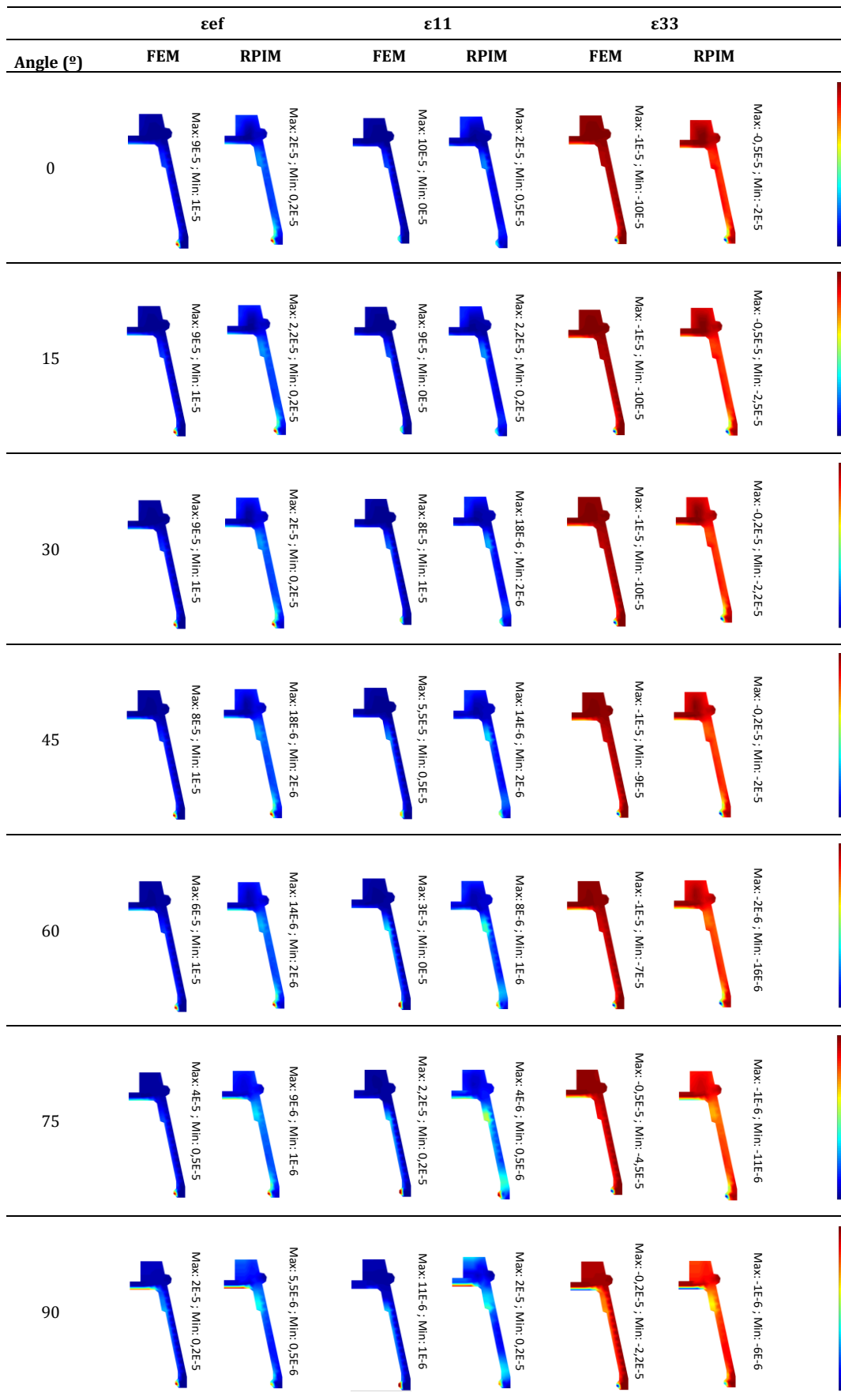


Table 24: Strain distribution map on titanium sleeve for MCB. Effective strain (Von Mises), principal strain ϵ_{11} and principal strain ϵ_{33} , respectively.



Regarding all the stress and strain maps relative to MCB, it is possible to observe that all the three parts will not experience damage in general.

The most solicited zones are really small compared for example with what happens in MCA.

6.3 Mechanical Case C

In this mechanical case, MCC, is it consider the seven different forces described in the Table 6 and the boundary condition (3), shown in Figure 16.

To understand the consequence of the load orientation in the dental implant, six interest points were selected in the interior of the domain, see Figure 23. For these points, P1, P2, P3, P7, P8 and P9 were obtained local displacements, stresses and strains which is possible to observe the measured values on Table 25, Table 26, Table 27, Table 28, Table 29 and Table 30, respectively.

Additionally, for easily interpret the results of Table 25, Table 26, Table 27, Table 28, Table 29 and Table 30, auxiliary graphs are presented, showing the variation of the stress and strain, respectively, with the angle of the applied loads. For the first three interest points (P1, P2 and P3), see Figure 24 and Figure 25 and for the other three points (P7, P8 and P9), see Figure 26 and Figure 27

For illustrating the stress and strain distribution in the complete domain, stress and strain maps are presented, allowing to visually compare the RPIM and FEM solutions for the different load angles. Additionally, these representations allow to visualize separately each one of the three parts constituting the dental implant. For the abutment, see Table 31 and Table 32. To the nylon sleeve, observe Table 33 and Table 34. Plus, observe Table 35 and Table 36 for the titanium sleeve.

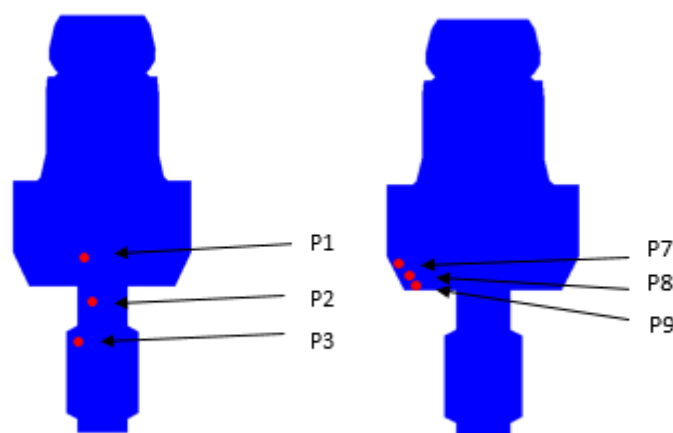


Figure 23: Interest points for analysis on MCC

Table 25: Obtained values for point 1 with both numerical methods, with respect to the angle of the applied load.

a	Method	ux	uy	uz	σ_1	σ_2	σ_3	σ_{ef}	ϵ_1	ϵ_2	ϵ_3	ϵ_{ef}
0	FEM	-3,66E-04	-1,17E-04	-1,86E-05	3,63E-01	6,72E-02	-8,37E-01	1,08E+00	5,22E-06	1,84E-06	-8,49E-06	8,28E-06
	RPIM	-4,80E-04	-1,47E-04	-2,38E-05	5,72E-01	1,95E-01	1,00E+00	1,42E+00	7,16E-06	2,84E-06	-1,08E-05	1,09E-05
	Dif.	3,11E-01	2,54E-01	2,80E-01	5,77E-01	1,89E+00	1,97E-01	3,15E-01	3,72E-01	5,44E-01	2,75E-01	3,11E-01
15	FEM	-3,55E-04	-1,16E-04	-1,78E-05	3,38E-01	7,36E-02	-8,42E-01	1,07E+00	5,00E-06	1,97E-06	-8,48E-06	8,20E-06
	RPIM	-4,65E-04	-1,44E-04	-2,28E-05	5,33E-01	1,99E-01	1,00E+00	1,40E+00	6,80E-06	2,99E-06	-1,07E-05	1,07E-05
	Dif.	3,09E-01	2,49E-01	2,84E-01	5,74E-01	1,70E+00	1,90E-01	3,03E-01	3,60E-01	5,12E-01	2,65E-01	3,00E-01
30	FEM	-3,21E-04	-1,06E-04	-1,58E-05	2,92E-01	7,39E-02	-7,89E-01	9,91E-01	4,46E-06	1,96E-06	-7,90E-06	7,58E-06
	RPIM	-4,19E-04	-1,32E-04	-2,03E-05	4,58E-01	1,89E-01	-9,34E-01	1,28E+00	5,98E-06	2,92E-06	-9,91E-06	9,75E-06
	Dif.	3,07E-01	2,45E-01	2,89E-01	5,65E-01	1,57E+00	1,83E-01	2,90E-01	3,43E-01	4,91E-01	2,54E-01	2,86E-01
45	FEM	-2,64E-04	-8,95E-05	-1,27E-05	2,29E-01	6,72E-02	-6,84E-01	8,43E-01	3,64E-06	1,79E-06	-6,79E-06	6,46E-06
	RPIM	-3,45E-04	-1,11E-04	-1,64E-05	3,52E-01	1,67E-01	-8,03E-01	1,07E+00	4,77E-06	2,65E-06	-8,42E-06	8,19E-06
	Dif.	3,04E-01	2,38E-01	2,96E-01	5,38E-01	1,48E+00	1,74E-01	2,73E-01	3,12E-01	4,82E-01	2,40E-01	2,69E-01
60	FEM	-1,90E-04	-6,68E-05	-8,74E-06	1,56E-01	5,08E-02	-5,32E-01	6,42E-01	2,64E-06	1,44E-06	-5,22E-06	4,92E-06
	RPIM	-2,47E-04	-8,20E-05	-1,14E-05	2,25E-01	1,31E-01	-6,17E-01	8,00E-01	3,26E-06	2,18E-06	-6,36E-06	6,10E-06
	Dif.	2,99E-01	2,29E-01	3,08E-01	4,46E-01	1,57E+00	1,60E-01	2,45E-01	2,37E-01	5,16E-01	2,19E-01	2,41E-01
75	FEM	-1,02E-04	-3,95E-05	-4,20E-06	9,18E-02	1,37E-02	-3,47E-01	4,05E-01	1,69E-06	7,92E-07	-3,33E-06	3,11E-06
	RPIM	-1,32E-04	-4,76E-05	-5,64E-06	1,08E-01	6,37E-02	-3,93E-01	4,80E-01	1,82E-06	1,31E-06	-3,90E-06	3,67E-06
	Dif.	2,86E-01	2,06E-01	3,44E-01	1,75E-01	3,67E+00	1,32E-01	1,84E-01	7,72E-02	6,53E-01	1,73E-01	1,80E-01
90	FEM	-2,21E-07	-3,34E-06	-1,54E-07	5,69E-02	5,18E-02	-9,25E-02	1,47E-01	6,07E-07	5,49E-07	-1,10E-06	1,12E-06
	RPIM	-1,94E-07	-3,52E-06	-1,23E-07	5,22E-02	5,04E-02	-1,00E-01	1,52E-01	5,91E-07	5,70E-07	-1,15E-06	1,16E-06
	Dif.	1,21E-01	5,40E-02	2,02E-01	8,29E-02	2,75E-02	8,68E-02	3,33E-02	2,72E-02	3,84E-02	4,94E-02	3,30E-02

Table 26: Obtained values for point 2 with both numerical methods, with respect to the angle of the applied load.

Angle	Method	ux	uy	uz	σ_1	σ_2	σ_3	σ_{ef}	ϵ_1	ϵ_2	ϵ_3	ϵ_{ef}
0	FEM	-9,68E-05	-4,57E-05	-7,35E-06	3,67E-02	-1,39E-01	3,85E+00	3,80E+00	1,08E-05	8,82E-06	-3,35E-05	2,97E-05
	RPIM	-1,28E-04	-5,65E-05	-9,87E-06	3,86E-01	-1,31E-01	5,04E+00	5,19E+00	1,70E-05	1,11E-05	-4,50E-05	4,03E-05
	Dif.	3,24E-01	2,36E-01	3,42E-01	9,52E+00	5,31E-02	3,11E-01	3,66E-01	5,73E-01	2,60E-01	3,42E-01	3,59E-01
15	FEM	-9,46E-05	-4,56E-05	-7,04E-06	3,50E-02	-1,36E-01	3,83E+00	3,78E+00	1,08E-05	8,81E-06	-3,34E-05	2,95E-05
	RPIM	-1,25E-04	-5,61E-05	-9,48E-06	3,75E-01	-1,30E-01	5,00E+00	5,14E+00	1,68E-05	1,10E-05	-4,46E-05	3,99E-05
	Dif.	3,21E-01	2,30E-01	3,47E-01	9,71E+00	4,34E-02	3,05E-01	3,59E-01	5,63E-01	2,54E-01	3,35E-01	3,52E-01
30	FEM	-8,59E-05	-4,24E-05	-6,24E-06	3,11E-02	-1,24E-01	3,55E+00	3,51E+00	9,96E-06	8,19E-06	-3,10E-05	2,74E-05
	RPIM	-1,13E-04	-5,19E-05	-8,45E-06	3,39E-01	-1,20E-01	4,61E+00	4,74E+00	1,54E-05	1,02E-05	-4,11E-05	3,68E-05
	Dif.	3,17E-01	2,25E-01	3,53E-01	9,89E+00	3,29E-02	2,98E-01	3,51E-01	5,51E-01	2,46E-01	3,27E-01	3,44E-01
45	FEM	-7,13E-05	-3,63E-05	-5,02E-06	2,53E-02	-1,04E-01	3,03E+00	2,99E+00	8,48E-06	7,01E-06	-2,64E-05	2,34E-05
	RPIM	-9,36E-05	-4,42E-05	-6,84E-06	2,80E-01	-1,02E-01	3,91E+00	4,01E+00	1,30E-05	8,68E-06	-3,48E-05	3,12E-05
	Dif.	3,13E-01	2,17E-01	3,61E-01	1,01E+01	1,97E-02	2,90E-01	3,40E-01	5,36E-01	2,37E-01	3,18E-01	3,34E-01
60	FEM	-5,19E-05	-2,77E-05	-3,46E-06	1,81E-02	-7,63E-02	2,30E+00	2,28E+00	6,43E-06	5,36E-06	-2,01E-05	1,78E-05
	RPIM	-6,78E-05	-3,34E-05	-4,76E-06	2,02E-01	-7,63E-02	2,94E+00	3,01E+00	9,73E-06	6,55E-06	-2,62E-05	2,34E-05
	Dif.	3,05E-01	2,06E-01	3,76E-01	1,01E+01	3,82E-04	2,77E-01	3,24E-01	5,12E-01	2,24E-01	3,03E-01	3,18E-01
75	FEM	-2,90E-05	-1,72E-05	-1,66E-06	1,05E-02	-4,38E-02	1,42E+00	1,41E+00	3,96E-06	3,34E-06	-1,24E-05	1,10E-05
	RPIM	-3,73E-05	-2,04E-05	-2,36E-06	1,10E-01	-4,57E-02	1,78E+00	1,81E+00	5,77E-06	3,99E-06	-1,58E-05	1,41E-05
	Dif.	2,87E-01	1,83E-01	4,21E-01	9,51E+00	4,27E-02	2,49E-01	2,90E-01	4,59E-01	1,96E-01	2,72E-01	2,85E-01
90	FEM	-1,06E-07	-1,62E-06	-5,05E-08	-2,03E-03	-2,46E-03	-1,45E-01	1,43E-01	3,71E-07	3,66E-07	-1,26E-06	1,11E-06
	RPIM	-1,19E-07	-1,74E-06	-4,50E-08	6,34E-05	-2,56E-03	-1,59E-01	1,58E-01	4,26E-07	3,96E-07	-1,39E-06	1,23E-06
	Dif.	1,18E-01	7,41E-02	1,09E-01	1,03E+00	4,04E-02	9,54E-02	1,04E-01	1,49E-01	8,22E-02	1,01E-01	1,03E-01

Table 27: Obtained values for point 3 with both numerical methods, with respect to the angle of the applied load.

Angle	Method	ux	uy	uz	σ_1	σ_2	σ_3	σ_{ef}	ϵ_1	ϵ_2	ϵ_3	ϵ_{ef}
0	FEM	-4,04E-07	-1,13E-05	-4,94E-07	-5,80E-01	-7,37E-01	3,06E+00	2,41E+00	4,93E-06	3,13E-06	-2,35E-05	1,97E-05
	RPIM	-8,88E-07	-1,51E-05	-7,98E-07	-5,93E-01	1,04E+00	4,27E+00	3,47E+00	8,78E-06	3,67E-06	-3,32E-05	2,82E-05
	Dif.	1,20E+00	3,38E-01	6,14E-01	2,32E-02	4,11E-01	3,93E-01	4,41E-01	7,82E-01	1,74E-01	4,15E-01	4,29E-01
15	FEM	-4,33E-07	-1,12E-05	-4,71E-07	-5,76E-01	-7,34E-01	3,04E+00	2,39E+00	4,90E-06	3,08E-06	-2,33E-05	1,96E-05
	RPIM	-9,07E-07	-1,49E-05	-7,68E-07	-5,90E-01	1,03E+00	4,21E+00	3,43E+00	8,65E-06	3,60E-06	-3,28E-05	2,78E-05
	Dif.	1,09E+00	3,31E-01	6,31E-01	2,36E-02	4,04E-01	3,85E-01	4,33E-01	7,67E-01	1,68E-01	4,07E-01	4,21E-01
30	FEM	-4,33E-07	-1,04E-05	-4,16E-07	-5,33E-01	-6,82E-01	2,81E+00	2,21E+00	4,53E-06	2,83E-06	-2,15E-05	1,81E-05
	RPIM	-8,63E-07	-1,37E-05	-6,87E-07	-5,46E-01	-9,52E-01	3,88E+00	3,15E+00	7,93E-06	3,29E-06	-3,01E-05	2,56E-05
	Dif.	9,92E-01	3,24E-01	6,50E-01	2,42E-02	3,96E-01	3,77E-01	4,24E-01	7,50E-01	1,62E-01	3,99E-01	4,12E-01
45	FEM	-4,04E-07	-8,81E-06	-3,32E-07	-4,53E-01	-5,83E-01	2,39E+00	1,88E+00	3,86E-06	2,38E-06	-1,83E-05	1,54E-05
	RPIM	-7,61E-07	-1,16E-05	-5,58E-07	-4,64E-01	-8,08E-01	3,27E+00	2,65E+00	6,67E-06	2,75E-06	-2,54E-05	2,16E-05
	Dif.	8,84E-01	3,14E-01	6,79E-01	2,50E-02	3,86E-01	3,67E-01	4,12E-01	7,27E-01	1,54E-01	3,88E-01	4,00E-01
60	FEM	-3,47E-07	-6,67E-06	-2,26E-07	-3,42E-01	-4,44E-01	1,81E+00	1,42E+00	2,94E-06	1,77E-06	-1,38E-05	1,16E-05
	RPIM	-6,07E-07	-8,66E-06	-3,91E-07	-3,51E-01	-6,09E-01	2,45E+00	1,98E+00	4,97E-06	2,02E-06	-1,90E-05	1,61E-05
	Dif.	7,49E-01	3,00E-01	7,30E-01	2,64E-02	3,71E-01	3,51E-01	3,93E-01	6,92E-01	1,41E-01	3,70E-01	3,82E-01
75	FEM	-2,66E-07	-4,07E-06	-1,04E-07	-2,08E-01	-2,75E-01	1,10E+00	8,65E-01	1,81E-06	1,04E-06	-8,43E-06	7,10E-06
	RPIM	-4,11E-07	-5,16E-06	-1,98E-07	-2,14E-01	-3,69E-01	1,45E+00	1,17E+00	2,93E-06	1,15E-06	-1,12E-05	9,53E-06
	Dif.	5,45E-01	2,68E-01	8,94E-01	2,98E-02	3,39E-01	3,16E-01	3,52E-01	6,13E-01	1,10E-01	3,32E-01	3,43E-01
90	FEM	-3,68E-08	-2,84E-07	8,01E-09	-8,83E-03	-1,91E-02	-7,52E-02	6,19E-02	1,71E-07	5,38E-08	-5,87E-07	5,01E-07
	RPIM	-3,96E-08	-3,06E-07	3,93E-09	-9,66E-03	-2,26E-02	-8,31E-02	6,79E-02	1,94E-07	4,57E-08	-6,45E-07	5,51E-07
	Dif.	7,59E-02	7,61E-02	5,09E-01	9,38E-02	1,86E-01	1,05E-01	9,69E-02	1,34E-01	1,52E-01	9,84E-02	9,95E-02

Table 28: Obtained values for point 7 with both numerical methods, with respect to the angle of the applied load.

Angle	Method	ux	uy	uz	σ_1	σ_2	σ_3	σ_{ef}	ϵ_1	ϵ_2	ϵ_3	ϵ_{ef}
0	FEM	-3,16E-04	-4,70E-04	-9,88E-05	1,33E+02	5,41E+01	4,78E+01	8,23E+01	9,01E-04	-1,85E-06	-7,32E-05	7,38E-04
	RPIM	-4,20E-04	-6,00E-04	-1,25E-04	1,74E+02	7,06E+01	6,34E+01	1,08E+02	1,18E-03	-6,26E-06	-8,86E-05	9,65E-04
	Dif.	3,26E-01	2,76E-01	2,64E-01	3,10E-01	3,06E-01	3,26E-01	3,06E-01	3,09E-01	2,39E+00	2,11E-01	3,08E-01
15	FEM	-3,07E-04	-4,57E-04	-9,52E-05	1,29E+02	5,25E+01	4,65E+01	8,00E+01	8,75E-04	-1,82E-06	-7,08E-05	7,17E-04
	RPIM	-4,07E-04	-5,82E-04	-1,20E-04	1,69E+02	6,85E+01	6,15E+01	1,04E+02	1,14E-03	-6,11E-06	-8,57E-05	9,36E-04
	Dif.	3,24E-01	2,74E-01	2,64E-01	3,08E-01	3,04E-01	3,24E-01	3,04E-01	3,07E-01	2,36E+00	2,10E-01	3,06E-01
30	FEM	-2,77E-04	-4,13E-04	-8,51E-05	1,17E+02	4,74E+01	4,20E+01	7,21E+01	7,90E-04	-1,66E-06	-6,37E-05	6,47E-04
	RPIM	-3,67E-04	-5,25E-04	-1,07E-04	1,52E+02	6,17E+01	5,55E+01	9,40E+01	1,03E-03	-5,54E-06	-7,69E-05	8,44E-04
	Dif.	3,22E-01	2,72E-01	2,64E-01	3,06E-01	3,02E-01	3,22E-01	3,02E-01	3,05E-01	2,33E+00	2,08E-01	3,04E-01
45	FEM	-2,28E-04	-3,40E-04	-6,92E-05	9,62E+01	3,91E+01	3,46E+01	5,94E+01	6,51E-04	-1,39E-06	-5,22E-05	5,33E-04
	RPIM	-3,01E-04	-4,32E-04	-8,74E-05	1,25E+02	5,08E+01	4,57E+01	7,72E+01	8,47E-04	-4,59E-06	-6,29E-05	6,93E-04
	Dif.	3,19E-01	2,69E-01	2,64E-01	3,03E-01	2,99E-01	3,19E-01	3,00E-01	3,02E-01	2,29E+00	2,06E-01	3,01E-01
60	FEM	-1,64E-04	-2,45E-04	-4,86E-05	6,91E+01	2,81E+01	2,49E+01	4,26E+01	4,67E-04	-1,03E-06	-3,71E-05	3,83E-04
	RPIM	-2,16E-04	-3,09E-04	-6,14E-05	8,97E+01	3,63E+01	3,27E+01	5,52E+01	6,06E-04	-3,33E-06	-4,46E-05	4,96E-04
	Dif.	3,14E-01	2,64E-01	2,64E-01	2,98E-01	2,94E-01	3,13E-01	2,95E-01	2,97E-01	2,23E+00	2,02E-01	2,96E-01
75	FEM	-8,84E-05	-1,32E-04	-2,47E-05	3,73E+01	1,52E+01	1,35E+01	2,30E+01	2,52E-04	-5,99E-07	-1,96E-05	2,06E-04
	RPIM	-1,15E-04	-1,66E-04	-3,12E-05	4,79E+01	1,94E+01	1,76E+01	2,95E+01	3,24E-04	-1,84E-06	-2,33E-05	2,65E-04
	Dif.	3,02E-01	2,52E-01	2,64E-01	2,86E-01	2,82E-01	3,00E-01	2,83E-01	2,85E-01	2,08E+00	1,92E-01	2,84E-01
90	FEM	-1,20E-06	-2,68E-06	3,50E-08	6,85E-01	3,46E-01	2,59E-01	3,90E-01	4,42E-06	5,56E-07	-4,44E-07	3,66E-06
	RPIM	-1,17E-06	-2,98E-06	1,83E-07	7,17E-01	3,63E-01	2,84E-01	3,99E-01	4,59E-06	5,54E-07	-3,51E-07	3,79E-06
	Dif.	1,97E-02	1,10E-01	4,23E+00	4,63E-02	4,88E-02	9,74E-02	2,35E-02	3,79E-02	2,78E-03	2,10E-01	3,51E-02

Table 29: Obtained values for point 8 with both numerical methods, with respect to the angle of the applied load.

Angle	Method	ux	uy	uz	σ_1	σ_2	σ_3	σ_{ef}	ϵ_1	ϵ_2	ϵ_3	ϵ_{ef}
0	FEM	-2,89E-04	-4,42E-04	-9,49E-05	1,07E+02	4,47E+01	3,88E+01	6,58E+01	7,23E-04	8,06E-06	-6,04E-05	5,92E-04
	RPIM	-3,76E-04	-5,68E-04	-1,19E-04	1,34E+02	5,55E+01	4,95E+01	8,14E+01	8,98E-04	4,71E-06	-6,41E-05	7,35E-04
	Dif.	3,03E-01	2,86E-01	2,59E-01	2,45E-01	2,40E-01	2,76E-01	2,37E-01	2,42E-01	4,16E-01	6,17E-02	2,41E-01
15	FEM	-2,81E-04	-4,30E-04	-9,14E-05	1,04E+02	4,35E+01	3,77E+01	6,39E+01	7,03E-04	7,82E-06	-5,84E-05	5,76E-04
	RPIM	-3,65E-04	-5,52E-04	-1,15E-04	1,30E+02	5,38E+01	4,80E+01	7,90E+01	8,71E-04	4,55E-06	-6,19E-05	7,13E-04
	Dif.	3,01E-01	2,84E-01	2,59E-01	2,44E-01	2,38E-01	2,74E-01	2,35E-01	2,40E-01	4,19E-01	6,04E-02	2,39E-01
30	FEM	-2,53E-04	-3,88E-04	-8,17E-05	9,42E+01	3,93E+01	3,41E+01	5,77E+01	6,34E-04	7,05E-06	-5,25E-05	5,20E-04
	RPIM	-3,29E-04	-4,97E-04	-1,03E-04	1,17E+02	4,85E+01	4,33E+01	7,12E+01	7,85E-04	4,07E-06	-5,56E-05	6,43E-04
	Dif.	2,99E-01	2,82E-01	2,59E-01	2,42E-01	2,36E-01	2,72E-01	2,33E-01	2,38E-01	4,22E-01	5,89E-02	2,37E-01
45	FEM	-2,09E-04	-3,20E-04	-6,64E-05	7,76E+01	3,24E+01	2,81E+01	4,75E+01	5,23E-04	5,79E-06	-4,30E-05	4,28E-04
	RPIM	-2,71E-04	-4,09E-04	-8,37E-05	9,62E+01	3,99E+01	3,57E+01	5,85E+01	6,46E-04	3,32E-06	-4,54E-05	5,29E-04
	Dif.	2,96E-01	2,79E-01	2,59E-01	2,39E-01	2,33E-01	2,69E-01	2,31E-01	2,36E-01	4,26E-01	5,69E-02	2,34E-01
60	FEM	-1,50E-04	-2,30E-04	-4,66E-05	5,58E+01	2,33E+01	2,03E+01	3,41E+01	3,76E-04	4,15E-06	-3,05E-05	3,08E-04
	RPIM	-1,94E-04	-2,93E-04	-5,87E-05	6,89E+01	2,86E+01	2,56E+01	4,19E+01	4,62E-04	2,35E-06	-3,22E-05	3,78E-04
	Dif.	2,91E-01	2,74E-01	2,59E-01	2,34E-01	2,28E-01	2,63E-01	2,26E-01	2,31E-01	4,34E-01	5,35E-02	2,30E-01
75	FEM	-8,11E-05	-1,25E-04	-2,37E-05	3,02E+01	1,26E+01	1,10E+01	1,84E+01	2,03E-04	2,22E-06	-1,60E-05	1,66E-04
	RPIM	-1,04E-04	-1,57E-04	-2,98E-05	3,69E+01	1,53E+01	1,38E+01	2,24E+01	2,47E-04	1,21E-06	-1,67E-05	2,03E-04
	Dif.	2,79E-01	2,61E-01	2,60E-01	2,23E-01	2,16E-01	2,50E-01	2,15E-01	2,20E-01	4,54E-01	4,44E-02	2,19E-01
90	FEM	-1,30E-06	-2,69E-06	6,76E-08	5,82E-01	3,30E-01	2,53E-01	2,98E-01	3,58E-06	6,97E-07	-1,80E-07	2,98E-06
	RPIM	-1,34E-06	-2,95E-06	1,92E-07	6,10E-01	3,40E-01	2,54E-01	3,22E-01	3,79E-06	7,10E-07	-2,72E-07	3,16E-06
	Dif.	3,12E-02	9,41E-02	1,84E+00	4,85E-02	3,11E-02	4,13E-03	7,98E-02	6,09E-02	1,86E-02	5,12E-01	6,08E-02

Table 30: Obtained values for point 9 with both numerical methods, with respect to the angle of the applied load.

Angle	Method	ux	uy	uz	σ_1	σ_2	σ_3	σ_{ef}	ϵ_1	ϵ_2	ϵ_3	ϵ_{ef}
0	FEM	-2,63E-04	-4,18E-04	-9,13E-05	1,16E+02	4,98E+01	4,26E+01	6,97E+01	7,72E-04	2,08E-05	-6,21E-05	6,33E-04
	RPIM	-3,39E-04	-5,41E-04	-1,15E-04	1,25E+02	5,35E+01	4,60E+01	7,58E+01	8,39E-04	1,81E-05	-6,67E-05	6,87E-04
	Dif.	2,87E-01	2,96E-01	2,64E-01	8,36E-02	7,28E-02	8,15E-02	8,76E-02	8,58E-02	1,31E-01	7,34E-02	8,55E-02
15	FEM	-2,56E-04	-4,06E-04	-8,80E-05	1,12E+02	4,84E+01	4,14E+01	6,77E+01	7,51E-04	2,02E-05	-6,01E-05	6,15E-04
	RPIM	-3,29E-04	-5,25E-04	-1,11E-04	1,22E+02	5,19E+01	4,47E+01	7,36E+01	8,14E-04	1,75E-05	-6,45E-05	6,67E-04
	Dif.	2,85E-01	2,93E-01	2,65E-01	8,20E-02	7,12E-02	7,99E-02	8,61E-02	8,42E-02	1,34E-01	7,22E-02	8,40E-02
30	FEM	-2,31E-04	-3,67E-04	-7,87E-05	1,02E+02	4,38E+01	3,74E+01	6,12E+01	6,78E-04	1,82E-05	-5,41E-05	5,56E-04
	RPIM	-2,97E-04	-4,74E-04	-9,95E-05	1,10E+02	4,68E+01	4,03E+01	6,63E+01	7,34E-04	1,58E-05	-5,79E-05	6,01E-04
	Dif.	2,83E-01	2,91E-01	2,65E-01	8,02E-02	6,94E-02	7,80E-02	8,43E-02	8,24E-02	1,37E-01	7,07E-02	8,22E-02
45	FEM	-1,91E-04	-3,03E-04	-6,40E-05	8,37E+01	3,61E+01	3,09E+01	5,04E+01	5,59E-04	1,50E-05	-4,43E-05	4,58E-04
	RPIM	-2,44E-04	-3,90E-04	-8,09E-05	9,02E+01	3,85E+01	3,32E+01	5,46E+01	6,04E-04	1,29E-05	-4,74E-05	4,95E-04
	Dif.	2,80E-01	2,88E-01	2,65E-01	7,78E-02	6,69E-02	7,55E-02	8,20E-02	8,00E-02	1,40E-01	6,88E-02	7,98E-02
60	FEM	-1,37E-04	-2,18E-04	-4,49E-05	6,02E+01	2,60E+01	2,23E+01	3,62E+01	4,02E-04	1,08E-05	-3,15E-05	3,29E-04
	RPIM	-1,75E-04	-2,80E-04	-5,68E-05	6,47E+01	2,76E+01	2,39E+01	3,91E+01	4,33E-04	9,19E-06	-3,36E-05	3,54E-04
	Dif.	2,75E-01	2,82E-01	2,65E-01	7,38E-02	6,27E-02	7,12E-02	7,80E-02	7,60E-02	1,46E-01	6,54E-02	7,58E-02
75	FEM	-7,44E-05	-1,18E-04	-2,28E-05	3,26E+01	1,41E+01	1,21E+01	1,96E+01	2,18E-04	5,78E-06	-1,66E-05	1,78E-04
	RPIM	-9,39E-05	-1,50E-04	-2,89E-05	3,47E+01	1,48E+01	1,29E+01	2,09E+01	2,32E-04	4,84E-06	-1,76E-05	1,90E-04
	Dif.	2,62E-01	2,69E-01	2,65E-01	6,33E-02	5,20E-02	6,05E-02	6,78E-02	6,57E-02	1,63E-01	5,65E-02	6,55E-02
90	FEM	-1,40E-06	-2,68E-06	9,10E-08	6,58E-01	3,84E-01	3,02E-01	3,23E-01	3,98E-06	8,48E-07	-9,82E-08	3,32E-06
	RPIM	-1,51E-06	-2,93E-06	1,91E-07	6,21E-01	3,69E-01	2,80E-01	3,07E-01	3,75E-06	8,64E-07	-1,50E-07	3,14E-06
	Dif.	7,88E-02	9,31E-02	1,10E+00	5,60E-02	4,12E-02	7,21E-02	5,06E-02	5,66E-02	1,81E-02	5,31E-01	5,28E-02

Regarding Table 25, Table 26 and Table 27, relative to points P1, P2 and P3 , respectively, the same conclusions can be made from the section 6.1 ,which is, the more closer the points are from the boundary condition the more bigger the difference between both numerical methods are.

For the other three points in study for this case, P7, P8 and P9, relative to Table 28, Table 29 and Table 30, the difference between FEM and RPIM are not so large, with differences for both methods surrounding the 15% - 30%, With the exception for principal strain ε_{22} .

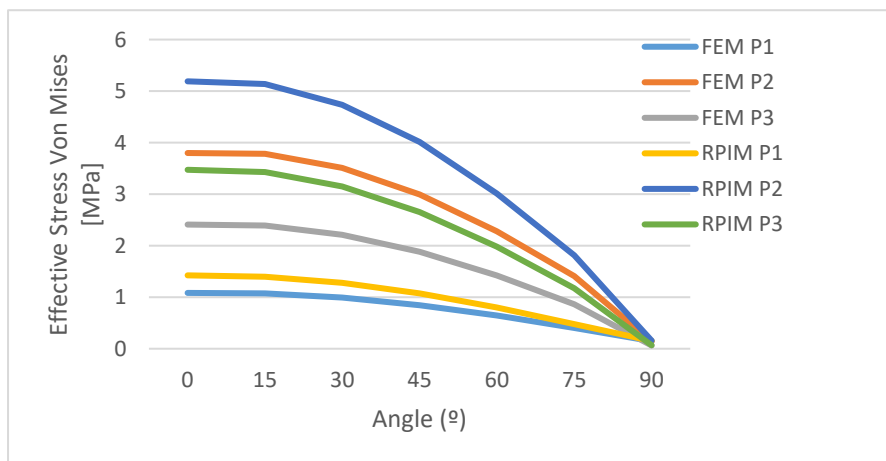
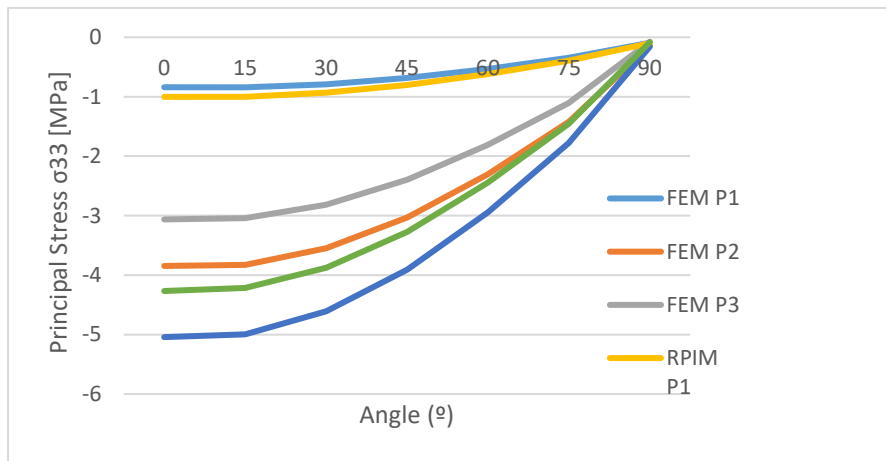
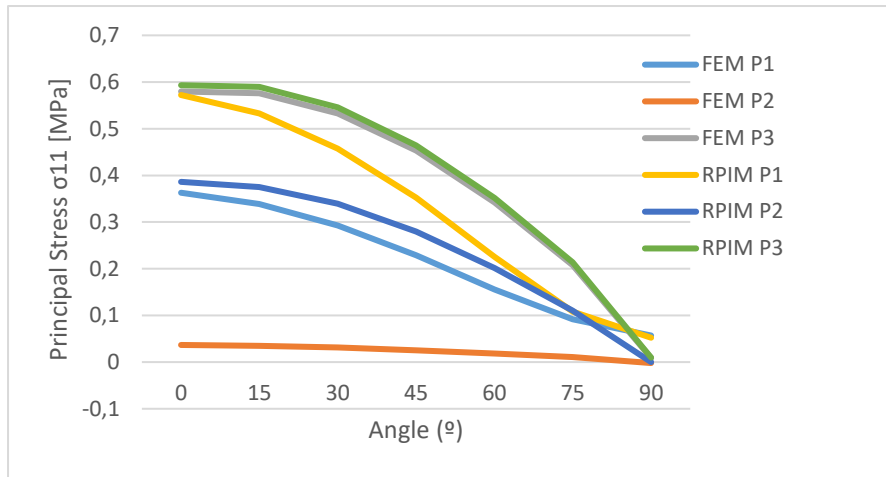


Figure 24: Principal Stress σ_{11} , Principal Stress σ_{33} and Effective Stress (Von Mises), respectively for MCC to interest points P1, P2 and P3 obtained with both numerical methods for distinct load angles

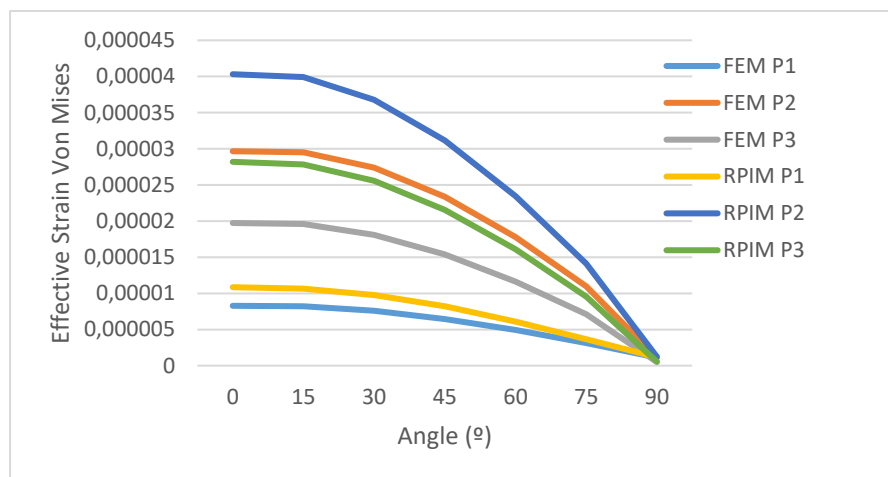
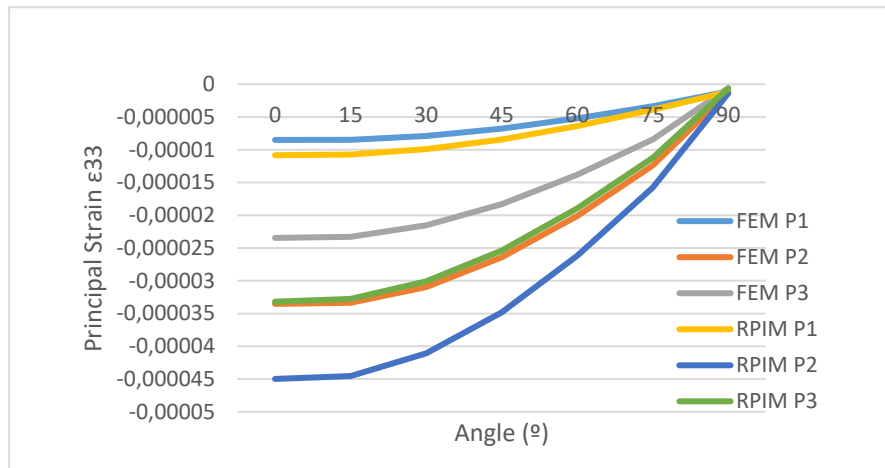
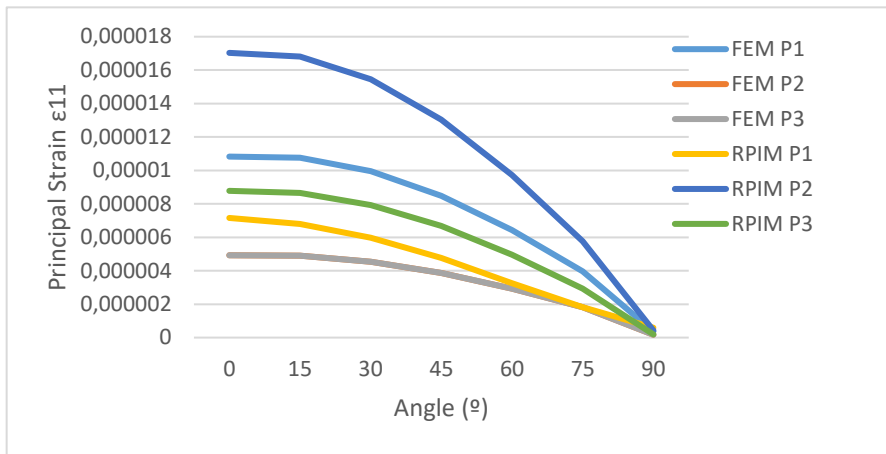


Figure 25: Principal Strain ϵ_{11} , Principal Strain ϵ_{33} and Effective Strain (Von Mises), respectively for MCC to interest points P1, P2 and P3 obtained with both numerical methods for distinct load angles

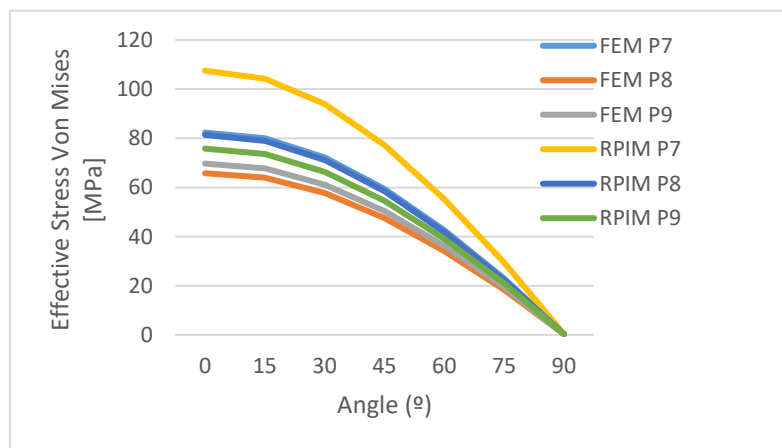
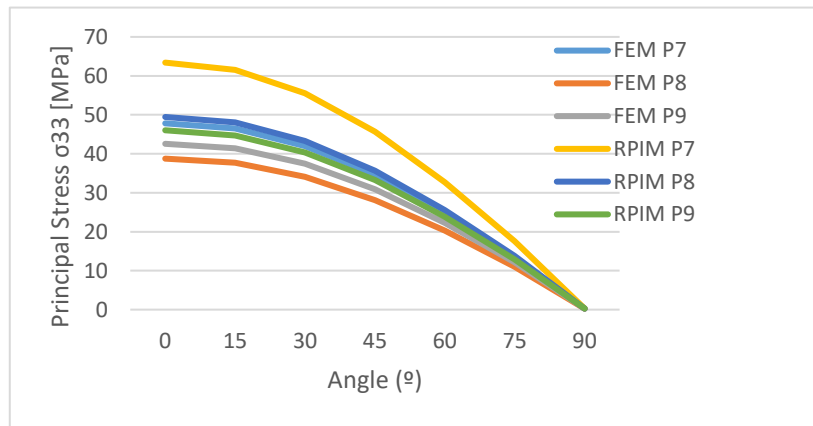
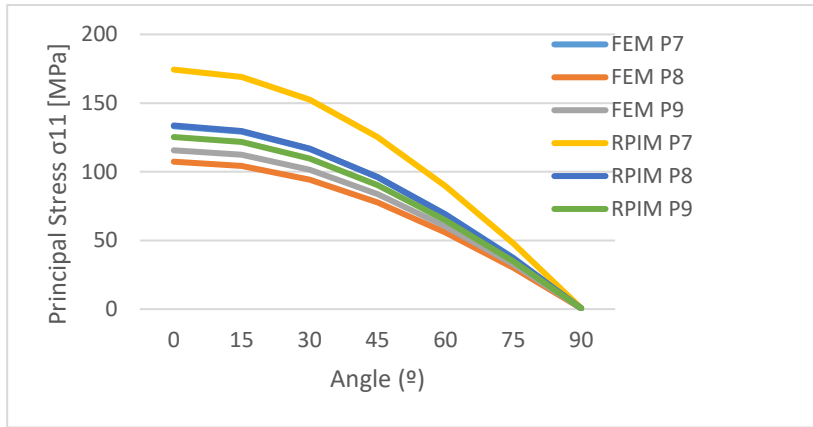


Figure 26: Principal Stress σ_{11} , Principal Stress σ_{33} and Effective Stress (Von Mises), respectively for MCC to interest points P7, P8 and P9 obtained with both numerical methods for distinct load angles

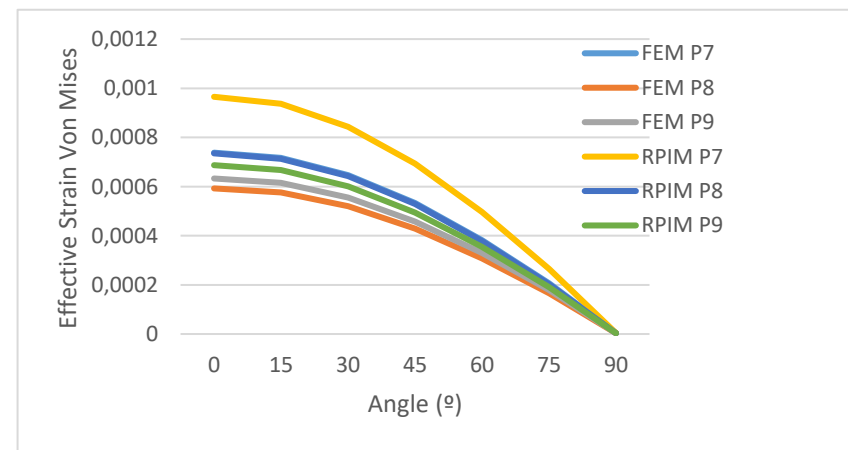
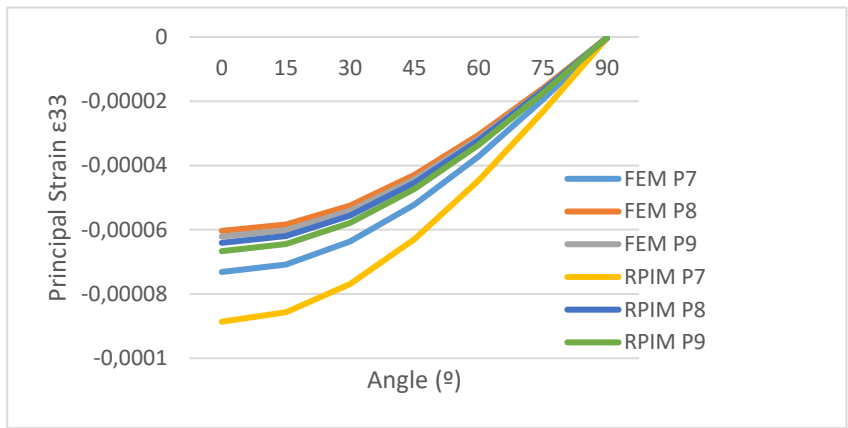
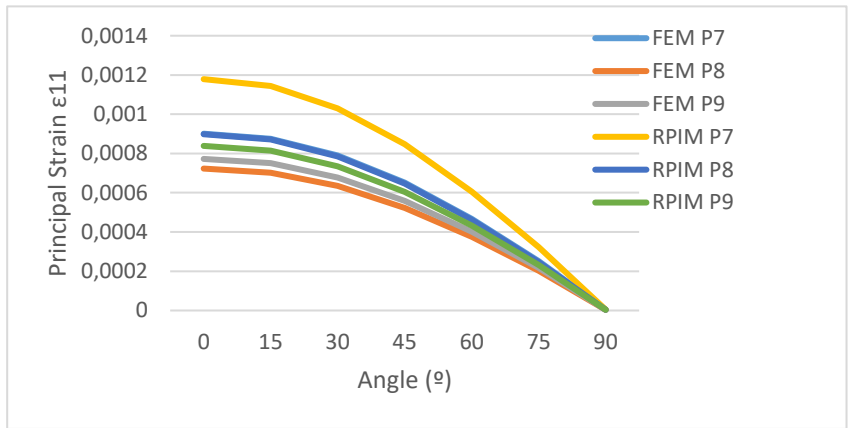


Figure 27: Principal Strain ϵ_{11} , Principal Strain ϵ_{33} and Effective Strain (Von Mises), respectively for MCC to interest points P7, P8 and P9 obtained with both numerical methods for distinct load angles

From the all the four graphics presented previously, both FEM and RPIM follows the same trend and the values for the stresses and strain decreases with the increasing of the load angle, which is expected because it is know that the shear loads are much more prejudicial than the axial loads.

For the points P1, P2 and P3, the effective stress von Mises, see Figure 24, the maximum value obtained was 5 MPa for 0° and around 0.1 MPa for 90° . Taking into account the masticatory forces ($Fv = 150 \text{ N}$ and $Fh = 15 \text{ N}$) and knowing that the yield stress of the commercial titanium used is 880 MPa, it is possible to observe that the implant will handle this forces since $5 \times 15 = 75 \text{ MPa}$ and $0.1 \times 150 = 15 \text{ MPa}$.

On the other hand, for the other three points (P7, P8 and P9), near the part where the implant is simple supported the values obtained for stresses and strains are much higher than expected, see Figure 26 and Figure 27, compared to the other ones obtained in MCA and MCB. This indicates that the boundary condition near point P7, P8 and P9 is excessively rigid. Notice that the implant will be inserted in a bone tissue, and not into a rigid medium. Therefore, relative displacement will be allowed, reducing the stress levels near points P7, P8 and P9. Therefore, future works should include the bone material in the analysis.

Table 31: Stress distribution map on abutment for MCC. Effective stress (von Mises), principal stress σ_{11} and principal stress σ_{33} , respectively. [MPa]

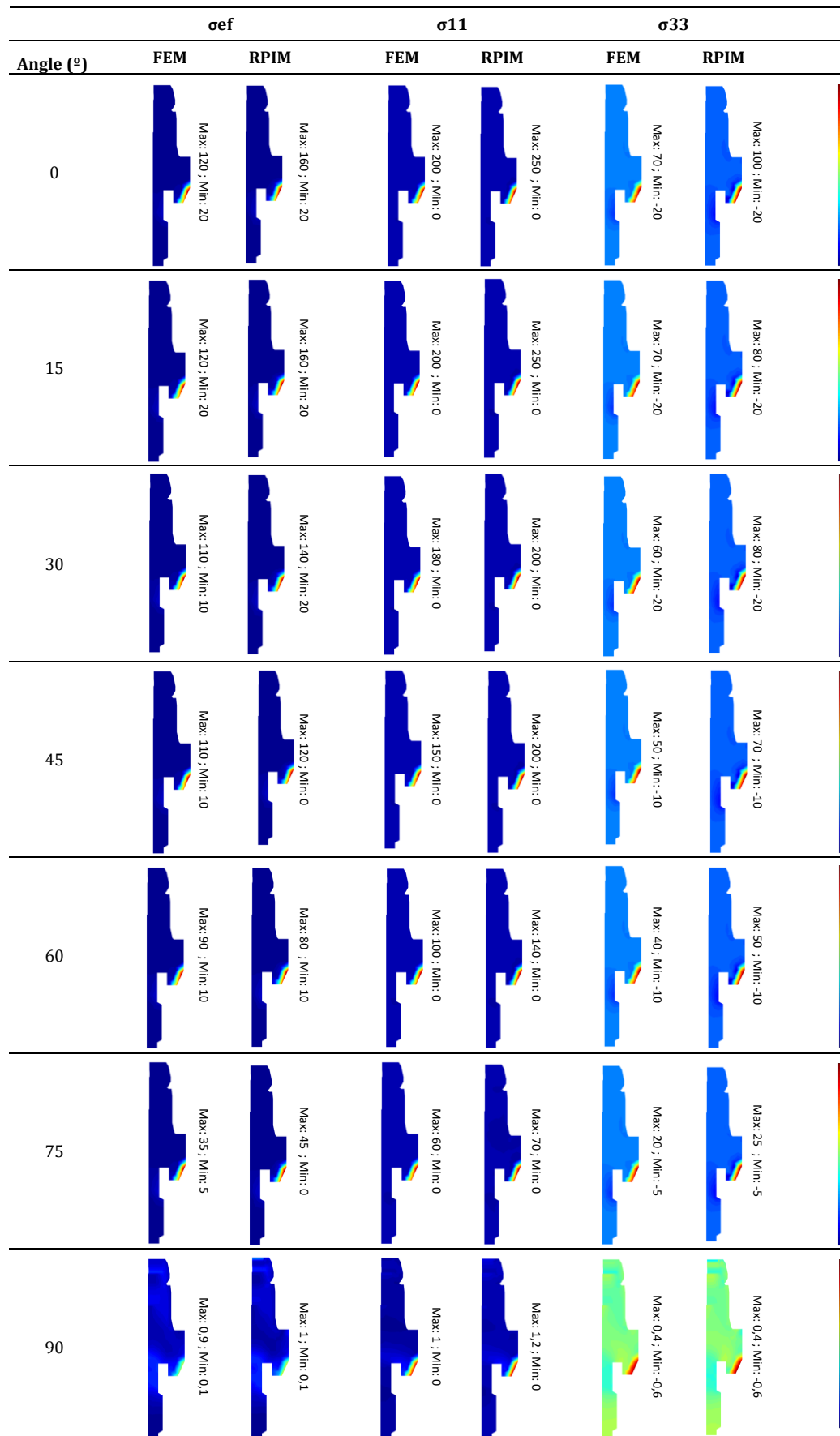


Table 32: Strain distribution map on abutment for MCC. Effective strain (von Mises), principal strain ϵ_{11} and principal strain ϵ_{33} , respectively.

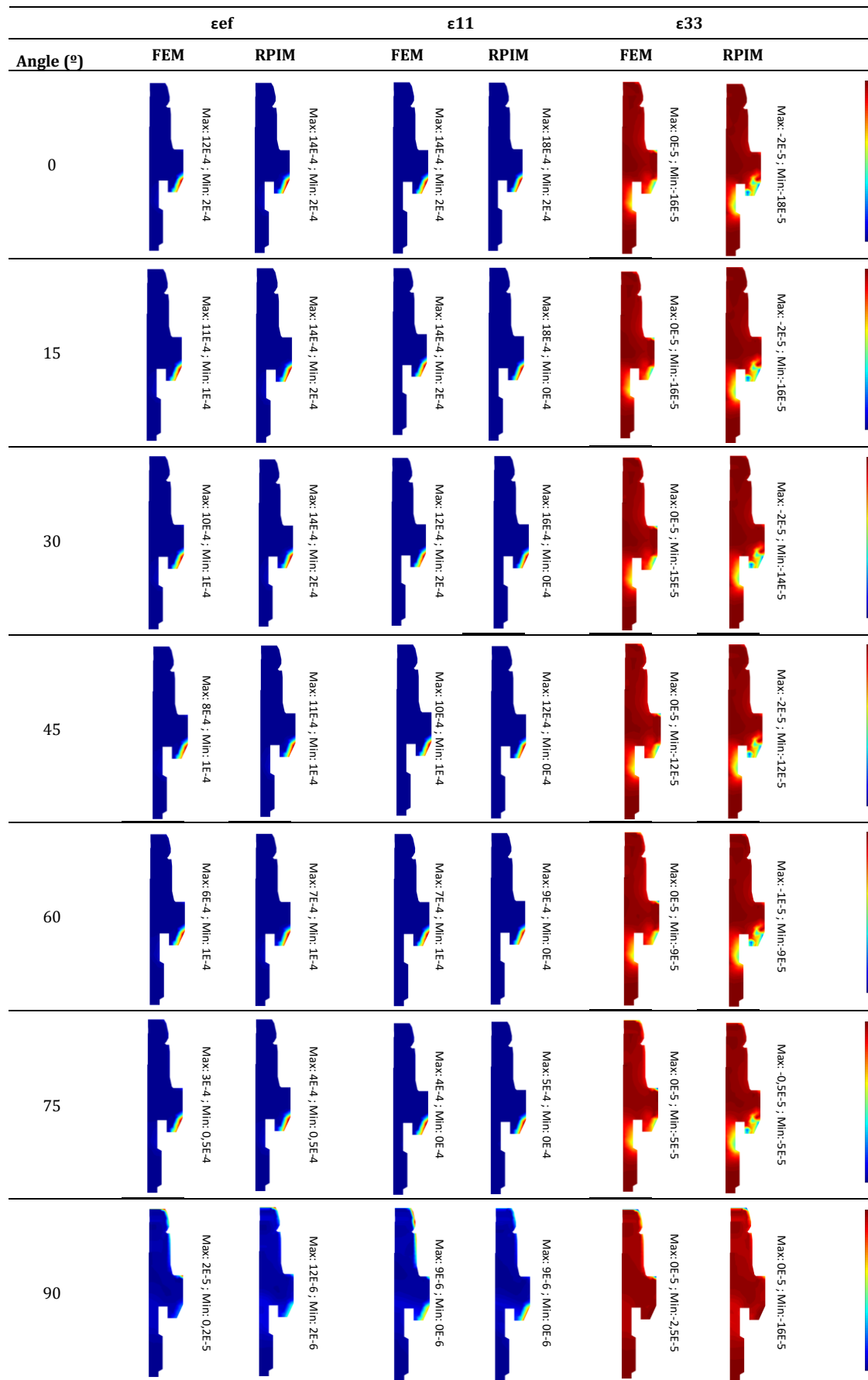


Table 33: Stress distribution map on nylon sleeve for MCC. Effective stress (von Mises), principal stress σ_{11} and principal stress σ_{33} , respectively. [MPa]

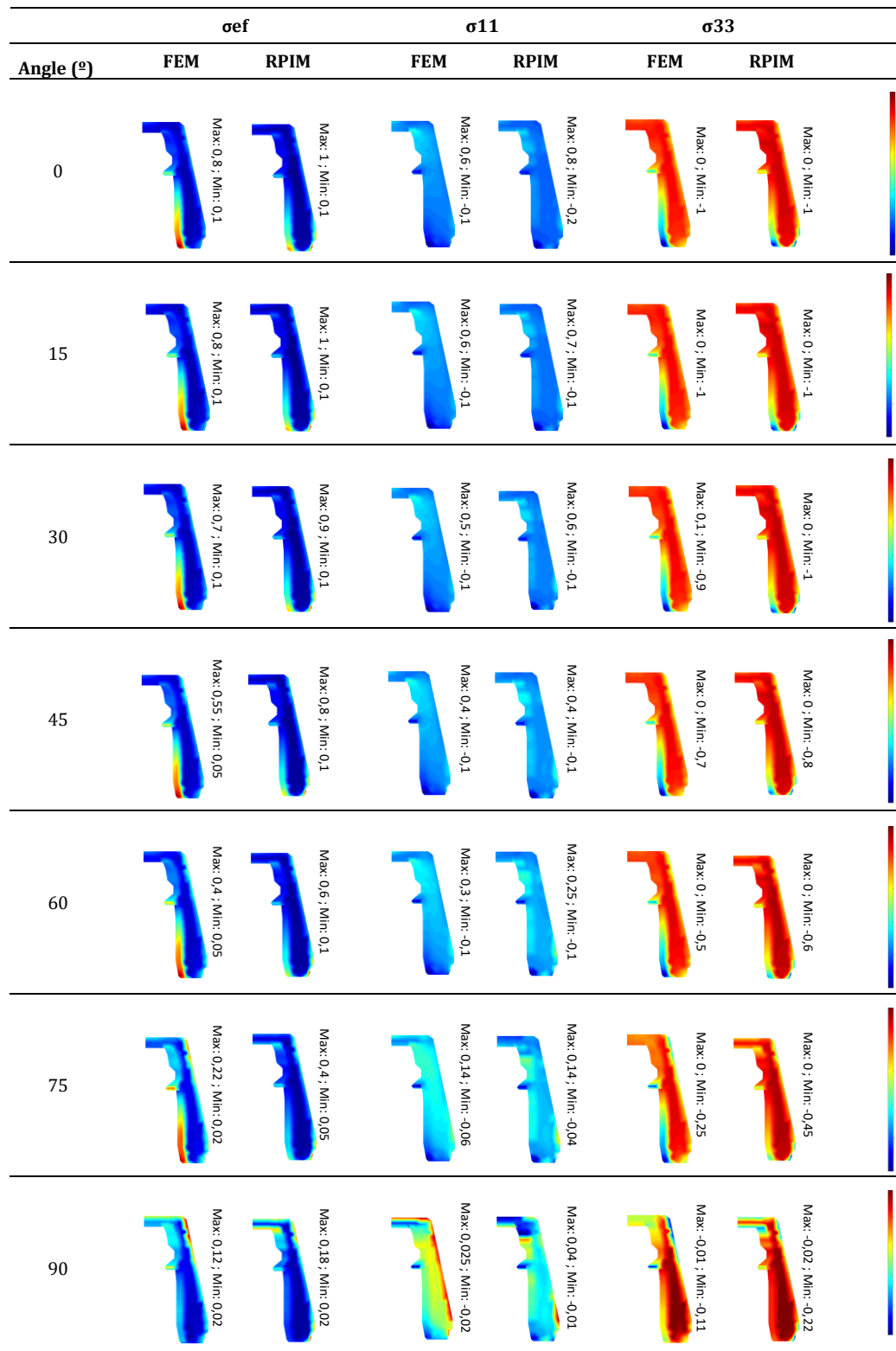


Table 34: Strain distribution map on nylon sleeve for MCC. Effective strain (Von Mises), principal strain ϵ_{11} and principal strain ϵ_{33} , respectively

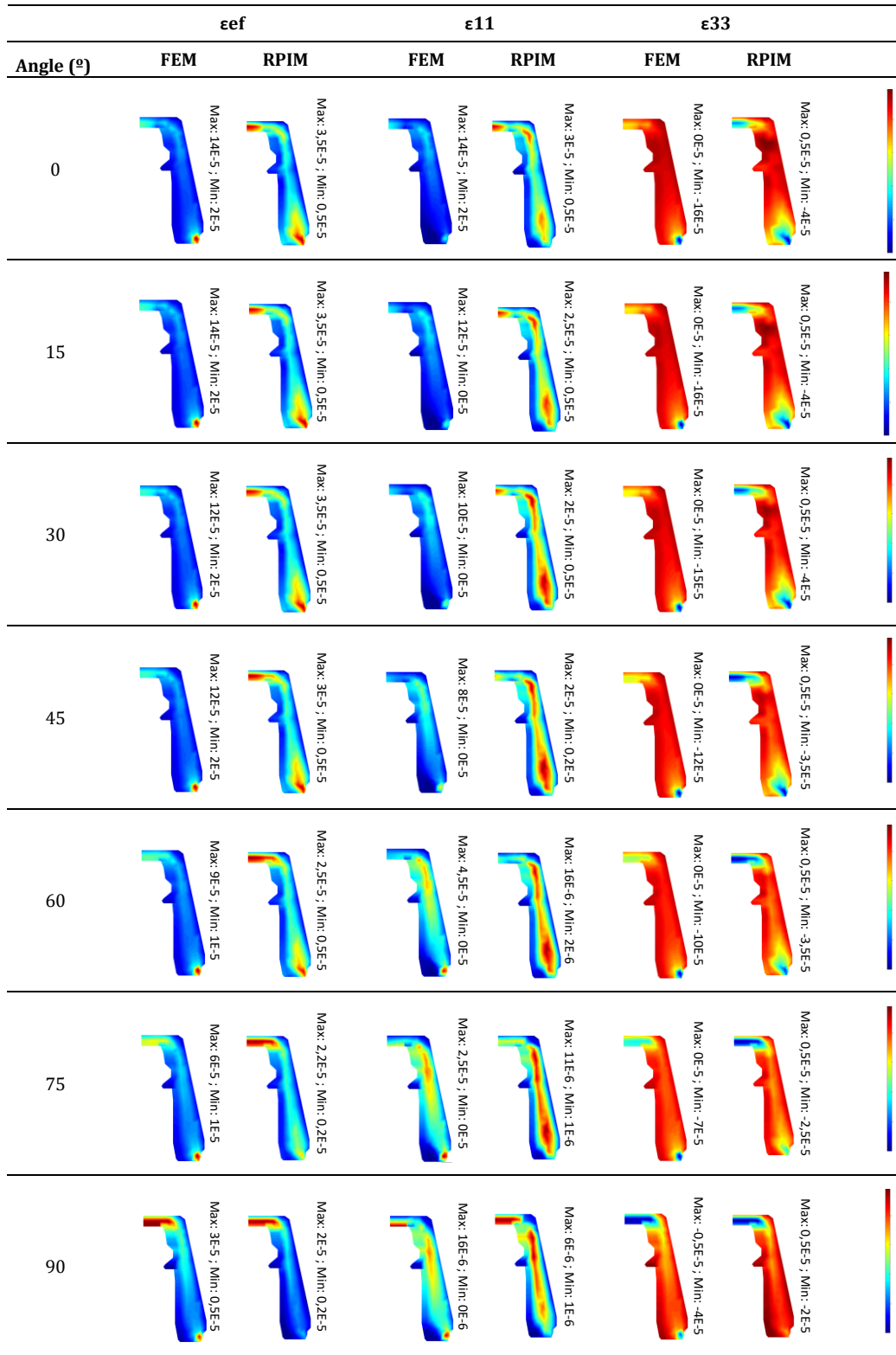


Table 35: Stress distribution map on titanium sleeve for MCC. Effective stress (von Mises), principal stress σ_{11} and principal stress σ_{33} , respectively. [MPa]

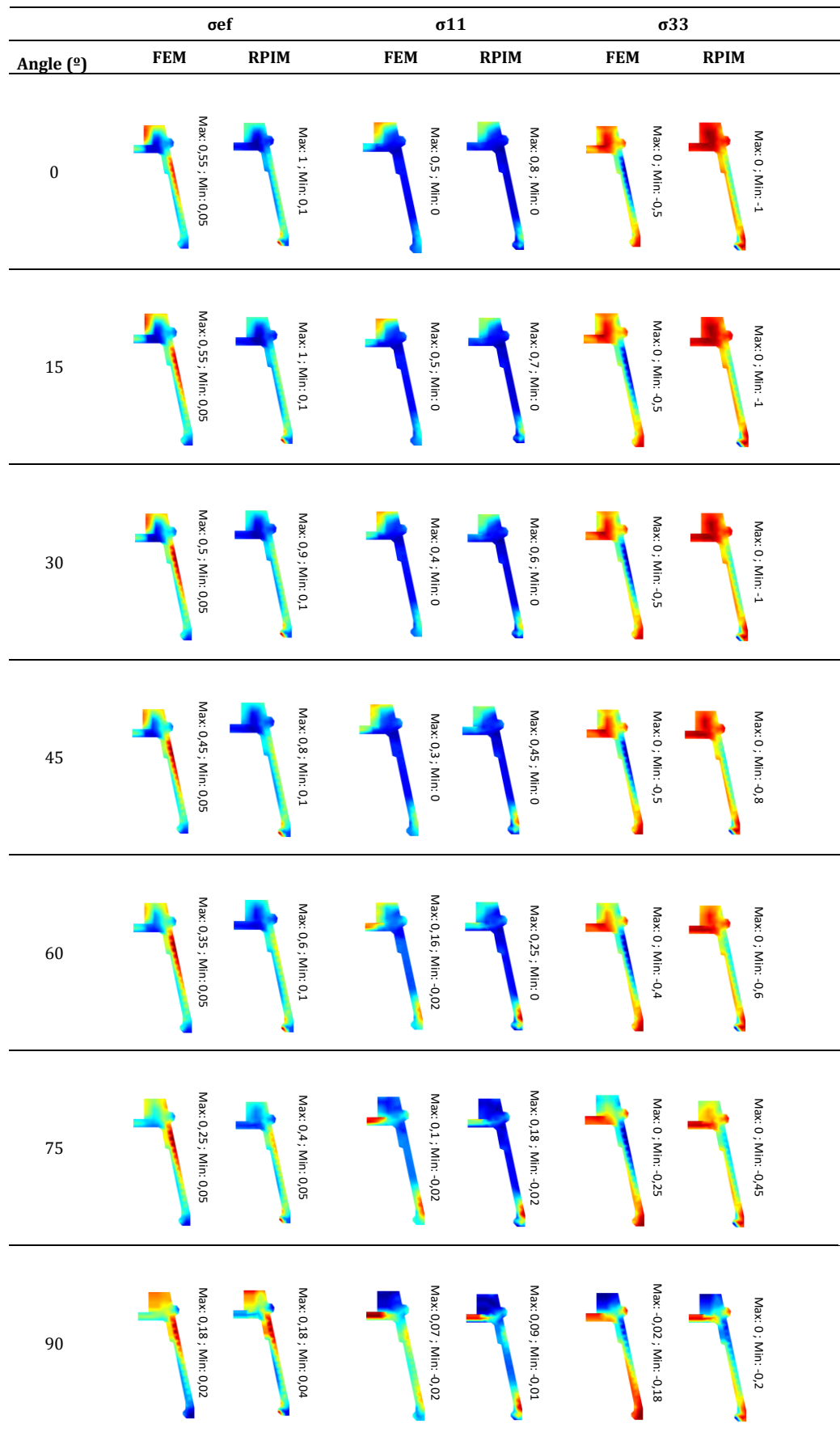
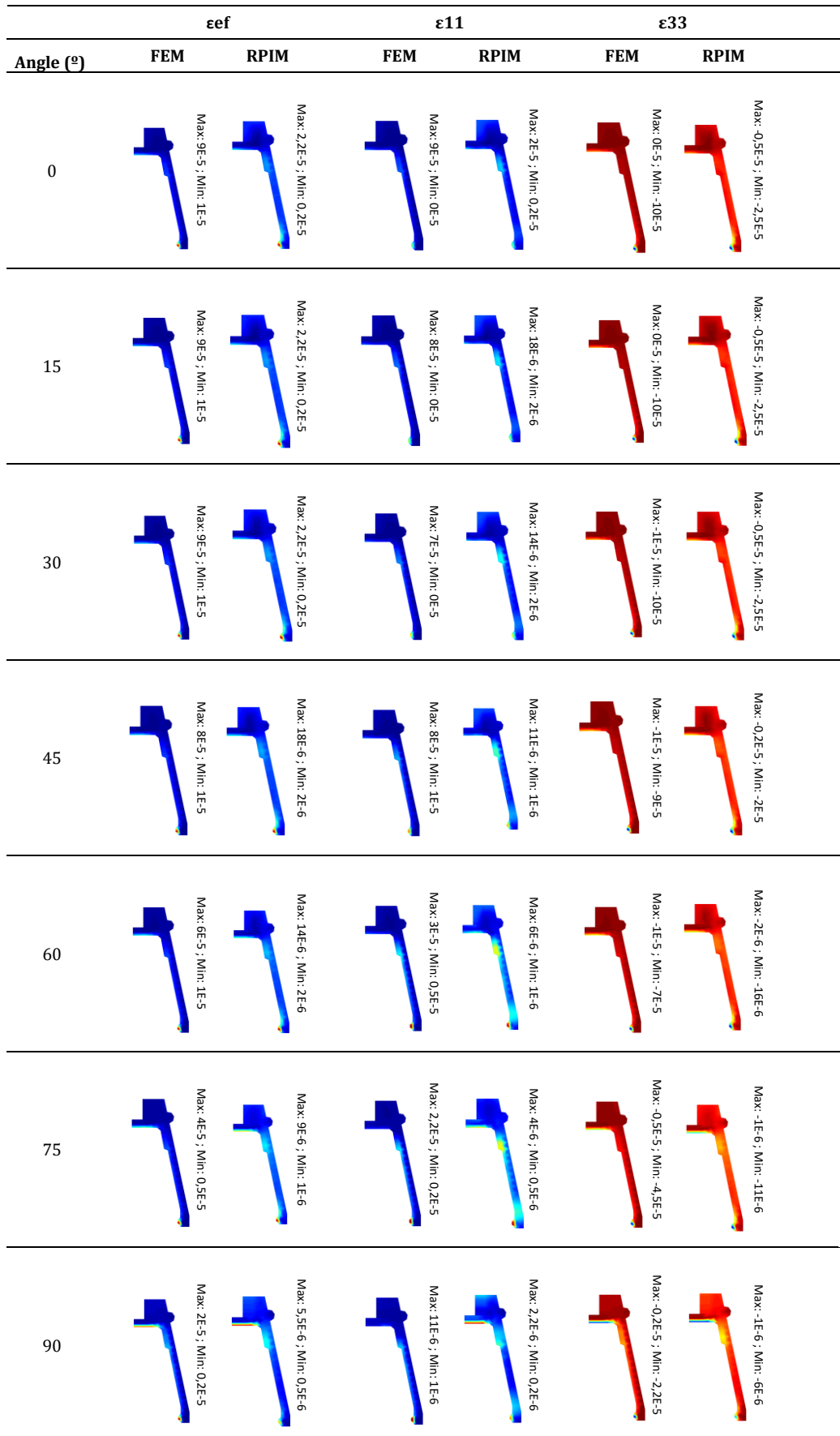


Table 36: Strain distribution map on titanium sleeve for MCC. Effective strain (Von Mises), principal strain ϵ_{11} and principal strain ϵ_{33} , respectively



Regarding the abutment, Table 31 and Table 32, it is again possible to observe that the zones more solicited for all loads, regardless the angle variation, are the ones next to the simple supported zone. Notice that these values are extremely high, comparing with the other mechanical cases.

For the nylon sleeve, Table 33 and Table 34, and for the titanium sleeve, Table 35 and Table 36, the stress and strain zones in interest are not so high and it is also possible to observe that for FEM the results are more expressive than the RPIM results, particularly for the stress in both sleeves.

6.4 Mechanical Case D

The mechanical case D (MCD) studies the torsion. The forces are applied like the ones in Figure 15 and the boundary condition applied is the (1) as explained in section 5.4, shown in Figure 16.

In order to comprehend the effect of the torsion forces applied in the upper part of the implant, several interest points were chosen in the interior of the domain, Figure 28. This set of points is dominated as “line of interest points”, because the only coordinate which varies is the y coordinate.

For these points were measured the local stresses and strains, which are possible to observe in the Table 37. Besides that, for a better understanding of these measured values, supplementary graphics are presented showing the variation of the stress and strain, along the interest line points as shown in Figure 29 and Figure 30, respectively.

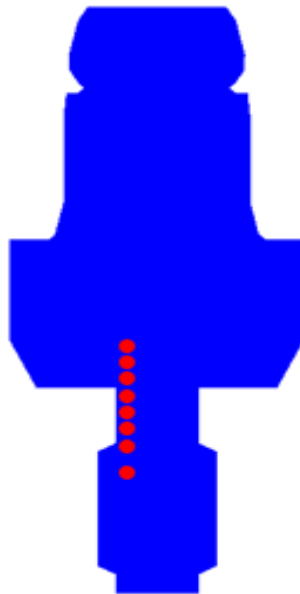


Figure 28: Line of interest point for analysis on MCD

Table 37: Obtained local values for the MMD at the interest points line for distinct nylon materials

y coord.	Method	σ_1	σ_2	σ_3	σ_{ef}	ϵ_1	ϵ_2	ϵ_3	ϵ_{ef}
-4,6296	FEM	2,93E-01	-2,92E-02	-3,66E-01	5,71E-01	3,61E-06	-6,39E-08	-3,91E-06	4,35E-06
	RPIM	3,92E-01	7,72E-04	-3,94E-01	6,81E-01	4,49E-06	1,19E-08	-4,50E-06	5,19E-06
	Dif.	3,40E-01	1,03E+00	7,73E-02	1,94E-01	2,41E-01	1,19E+00	1,51E-01	1,93E-01
-4,283	FEM	7,85E-01	-2,34E-01	-9,92E-01	1,54E+00	1,01E-05	-1,51E-06	-1,02E-05	1,18E-05
	RPIM	1,10E+00	7,33E-03	1,10E+00	1,91E+00	1,25E-05	7,67E-08	-1,26E-05	1,45E-05
	Dif.	4,00E-01	1,03E+00	1,12E-01	2,35E-01	2,39E-01	1,05E+00	2,40E-01	2,33E-01
-3,9497	FEM	1,37E+00	-2,34E-02	1,40E+00	2,39E+00	1,57E-05	-1,29E-07	-1,58E-05	1,82E-05
	RPIM	1,52E+00	7,45E-03	1,50E+00	2,61E+00	1,73E-05	9,24E-09	-1,72E-05	1,99E-05
	Dif.	1,11E-01	1,32E+00	7,28E-02	9,19E-02	9,68E-02	1,07E+00	8,70E-02	9,19E-02
-3,6163	FEM	1,36E+00	1,21E-01	1,30E+00	2,31E+00	1,51E-05	9,07E-07	-1,54E-05	1,76E-05
	RPIM	1,53E+00	1,84E-03	1,52E+00	2,64E+00	1,74E-05	7,99E-09	-1,74E-05	2,01E-05
	Dif.	1,19E-01	9,85E-01	1,69E-01	1,42E-01	1,54E-01	9,91E-01	1,33E-01	1,42E-01
-3,283	FEM	1,35E+00	-2,40E-01	1,51E+00	2,49E+00	1,65E-05	-1,68E-06	-1,62E-05	1,90E-05
	RPIM	1,56E+00	-3,56E-03	1,56E+00	2,70E+00	1,78E-05	-2,75E-08	-1,78E-05	2,06E-05
	Dif.	1,55E-01	9,85E-01	3,12E-02	8,72E-02	8,11E-02	9,84E-01	9,78E-02	8,65E-02
-2,9497	FEM	1,48E+00	1,31E-01	1,40E+00	2,50E+00	1,64E-05	9,19E-07	-1,65E-05	1,90E-05
	RPIM	1,58E+00	3,46E-03	1,57E+00	2,73E+00	1,80E-05	1,03E-09	-1,80E-05	2,08E-05
	Dif.	6,48E-02	9,74E-01	1,24E-01	9,30E-02	1,00E-01	9,99E-01	8,73E-02	9,28E-02
-2,6163	FEM	1,50E+00	1,29E-01	1,44E+00	2,54E+00	1,66E-05	9,84E-07	-1,69E-05	1,94E-05
	RPIM	1,67E+00	2,87E-03	1,67E+00	2,89E+00	1,91E-05	2,77E-08	-1,91E-05	2,20E-05
	Dif.	1,16E-01	9,78E-01	1,59E-01	1,36E-01	1,48E-01	9,72E-01	1,26E-01	1,36E-01
-2,283	FEM	7,52E-01	-6,08E-02	-8,78E-01	1,41E+00	9,08E-06	-2,04E-07	-9,53E-06	1,08E-05
	RPIM	1,04E+00	2,44E-03	1,07E+00	1,82E+00	1,19E-05	1,07E-07	-1,21E-05	1,39E-05
	Dif.	3,78E-01	1,04E+00	2,17E-01	2,91E-01	3,12E-01	1,53E+00	2,72E-01	2,91E-01

In general, for MCD, the differences for both methods are comprehended between 10% - 30% in exception for the principal stress σ_{22} and principal strain ϵ_{22} .

Another interesting fact, which is even more clearly in the Figure 29 and Figure 30, is that the values obtained with RPIM are a slightly higher than the ones obtained with FEM.

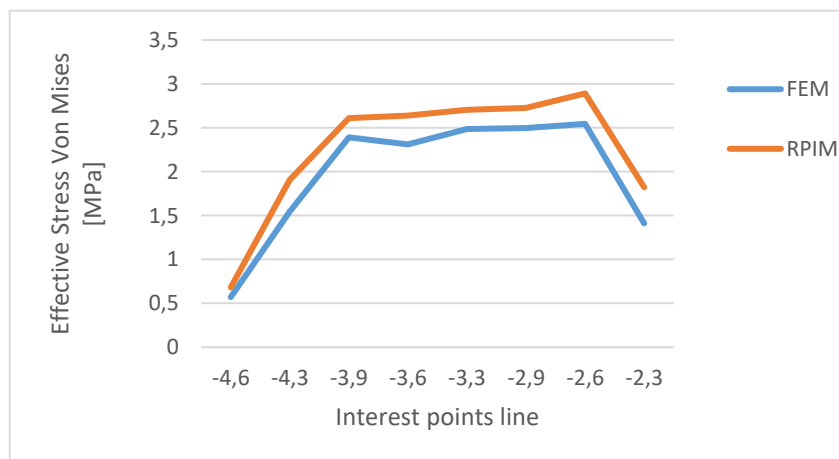
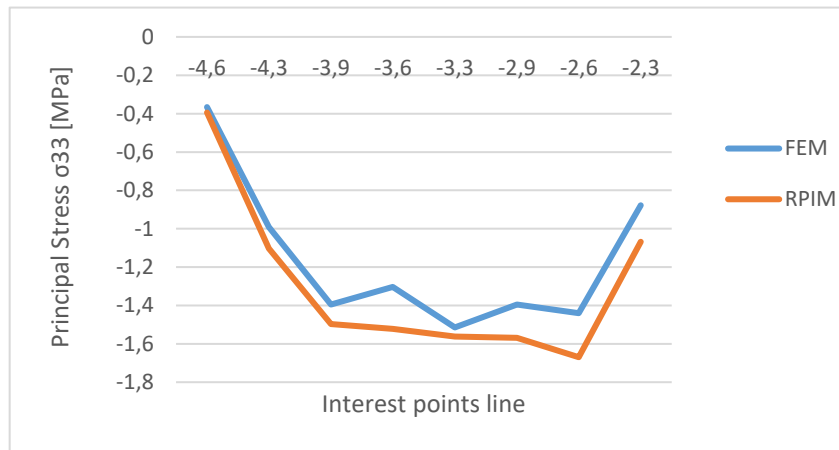
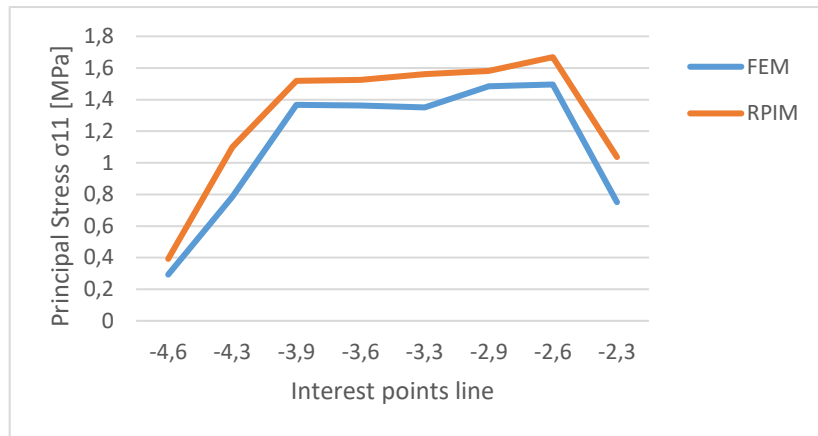


Figure 29: Principal Stress σ_{11} , Principal Stress σ_{33} and Effective Stress (Von Mises), respectively for MCD obtained with both numerical methods along the interest points line

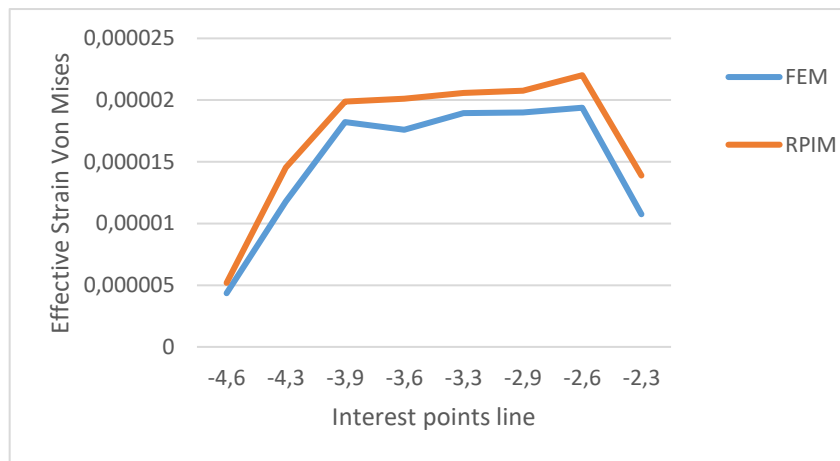
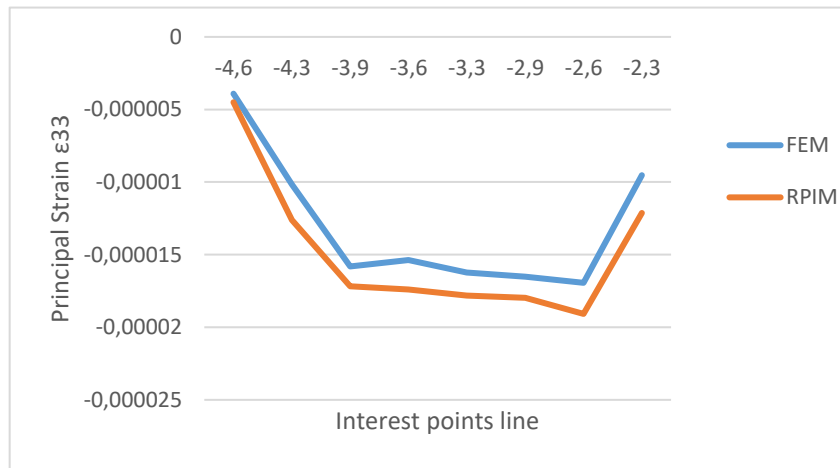


Figure 30: Principal Strain ϵ_{11} , Principal Strain ϵ_{33} and Effective Strain (Von Mises), respectively for MCD obtained with both numerical methods along the interest points line

6.5 Study on Distinct Materials

In this section, distinct nylon materials for the nylon sleeve will be studied. Thus, the model previously presented will be analysed with both FEM and RPIM formulations considering distinct nylon sleeves. The solutions will be compared.

The analyses were performed for two different cases. Firstly, it was performed for the MCC and only for the case which the load angle applied is 45° , see Table 6. Afterwards, the same analysis was done for MCD with the same procedures as explained in the section 6.4.

Additionally, in order to understand the effects of changing the material in the nylon sleeve, a point was specifically chosen inside the domain of the nylon sleeve, as Figure 31 shows. For comparison purposes, the displacements, stresses and strains values were obtained with both FEM and RPIM at point P10.

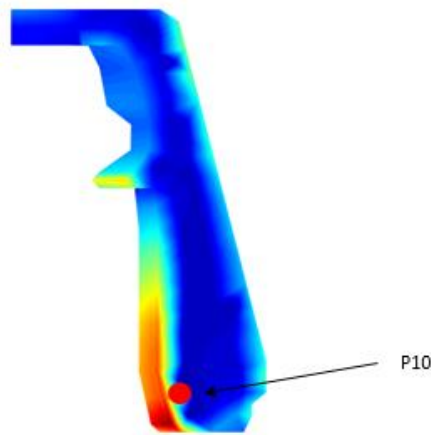


Figure 31: Interest point for analysis on nylon sleeve

6.5.1 Mechanical Case C

Following the same procedure as in section 6.3, the measured displacements, stresses and strains for the interest points (P1, P2, P3, P7, P8 and P9, Figure 23) regarding the case MCC, can be observed in Table 38, Table 39, Table 40, Table 41, Table 42 and Table 43, respectively.

Also, to show the stress and strain distribution in complete domain, stress and strain maps are presented, respectively, for the three distinct parts that constitute the dental implant, letting to visually compare the RPIM and FEM solutions for the different nylons. For the abutment, observe Table 45 and Table 46. For the nylon sleeve, see Table 47 and Table 48. And for the titanium sleeve, observe Table 49 and Table 50.

For the point 10, inside the domain of the nylon sleeve, the measured displacements, stresses and strain can be observed in Table 44.

Table 38: Obtained local values for the MMC at point 1 for distinct nylon materials.

Mat.	Method	ux	uy	uz	σ_1	σ_2	σ_3	σ_{ef}	ϵ_1	ϵ_2	ϵ_3	ϵ_{ef}
L20H	FEM	-2,70E-04	-9,16E-05	-1,30E-05	2,34E-01	6,87E-02	-6,99E-01	8,63E-01	3,72E-06	1,83E-06	-6,94E-06	6,60E-06
	RPIM	-3,53E-04	-1,13E-04	-1,68E-05	3,60E-01	1,70E-01	-8,21E-01	1,10E+00	4,88E-06	2,71E-06	-8,61E-06	8,38E-06
	Dif.	3,04E-01	2,38E-01	2,96E-01	5,38E-01	1,48E+00	1,74E-01	2,73E-01	3,12E-01	4,82E-01	2,40E-01	2,69E-01
GV5	FEM	-2,70E-04	-9,15E-05	-1,27E-05	2,17E-01	6,33E-02	-6,88E-01	8,39E-01	3,55E-06	1,80E-06	-6,78E-06	6,42E-06
	RPIM	-3,52E-04	-1,13E-04	-1,66E-05	3,51E-01	1,72E-01	-8,16E-01	1,09E+00	4,78E-06	2,74E-06	-8,55E-06	8,31E-06
	Dif.	3,04E-01	2,39E-01	3,09E-01	6,18E-01	1,72E+00	1,87E-01	2,99E-01	3,46E-01	5,25E-01	2,61E-01	2,94E-01
LV3H	FEM	-2,70E-04	-9,15E-05	-1,29E-05	2,26E-01	6,56E-02	-6,93E-01	8,50E-01	3,64E-06	1,81E-06	-6,86E-06	6,51E-06
	RPIM	-3,52E-04	-1,13E-04	-1,68E-05	3,59E-01	1,73E-01	-8,20E-01	1,10E+00	4,86E-06	2,74E-06	-8,61E-06	8,37E-06
	Dif.	3,04E-01	2,39E-01	3,02E-01	5,89E-01	1,64E+00	1,84E-01	2,92E-01	3,36E-01	5,14E-01	2,56E-01	2,87E-01
LKN	FEM	-2,70E-04	-9,16E-05	-1,29E-05	2,31E-01	6,75E-02	-6,97E-01	8,58E-01	3,69E-06	1,82E-06	-6,91E-06	6,57E-06
	RPIM	-3,52E-04	-1,13E-04	-1,68E-05	3,61E-01	1,72E-01	-8,21E-01	1,10E+00	4,88E-06	2,73E-06	-8,62E-06	8,39E-06
	Dif.	3,04E-01	2,39E-01	2,98E-01	5,60E-01	1,55E+00	1,78E-01	2,82E-01	3,22E-01	4,98E-01	2,47E-01	2,77E-01

Table 39: Obtained local values for the MMC at point 2 for distinct nylon materials.

Mat.	Method	ux	uy	uz	σ_1	σ_2	σ_3	σ_{ef}	ϵ_1	ϵ_2	ϵ_3	ϵ_{ef}
L20H	FEM	-7,30E-05	-3,71E-05	-5,14E-06	2,59E-02	-1,06E-01	-3,10E+00	3,06E+00	8,68E-06	7,17E-06	-2,70E-05	2,39E-05
	RPIM	-9,58E-05	-4,52E-05	-6,99E-06	2,86E-01	-1,04E-01	-4,00E+00	4,10E+00	1,33E-05	8,87E-06	-3,56E-05	3,19E-05
	Dif.	3,13E-01	2,17E-01	3,61E-01	1,01E+01	1,97E-02	2,90E-01	3,40E-01	5,36E-01	2,37E-01	3,18E-01	3,34E-01
GV5	FEM	-7,30E-05	-3,72E-05	-5,01E-06	2,74E-02	-1,06E-01	-3,10E+00	3,06E+00	8,70E-06	7,17E-06	-2,70E-05	2,39E-05
	RPIM	-9,58E-05	-4,52E-05	-6,91E-06	2,87E-01	-1,04E-01	-4,00E+00	4,11E+00	1,33E-05	8,87E-06	-3,56E-05	3,19E-05
	Dif.	3,12E-01	2,17E-01	3,80E-01	9,47E+00	1,66E-02	2,90E-01	3,40E-01	5,34E-01	2,37E-01	3,17E-01	3,33E-01
LV3H	FEM	-7,30E-05	-3,71E-05	-5,08E-06	2,67E-02	-1,06E-01	-3,10E+00	3,06E+00	8,69E-06	7,17E-06	-2,70E-05	2,39E-05
	RPIM	-9,58E-05	-4,52E-05	-6,96E-06	2,86E-01	-1,04E-01	-4,00E+00	4,10E+00	1,33E-05	8,87E-06	-3,56E-05	3,19E-05
	Dif.	3,12E-01	2,17E-01	3,70E-01	9,72E+00	1,85E-02	2,90E-01	3,40E-01	5,35E-01	2,38E-01	3,18E-01	3,34E-01
LKN	FEM	-7,30E-05	-3,71E-05	-5,12E-06	2,62E-02	-1,06E-01	-3,10E+00	3,06E+00	8,68E-06	7,17E-06	-2,70E-05	2,39E-05
	RPIM	-9,58E-05	-4,52E-05	-6,98E-06	2,86E-01	-1,04E-01	-4,00E+00	4,10E+00	1,33E-05	8,87E-06	-3,56E-05	3,19E-05
	Dif.	3,12E-01	2,17E-01	3,64E-01	9,93E+00	1,94E-02	2,90E-01	3,40E-01	5,36E-01	2,38E-01	3,18E-01	3,34E-01

Table 40: Obtained local values for the MMC at point 3 for distinct nylon materials.

Mat.	Method	ux	uy	uz	σ_1	σ_2	σ_3	σ_{ef}	ϵ_1	ϵ_2	ϵ_3	ϵ_{ef}
L20H	FEM	-4,13E-07	-9,01E-06	-3,40E-07	-4,64E-01	-5,96E-01	-2,45E+00	1,92E+00	3,95E-06	2,44E-06	-1,87E-05	1,57E-05
	RPIM	-7,78E-07	-1,18E-05	-5,71E-07	-4,75E-01	-8,27E-01	-3,35E+00	2,71E+00	6,83E-06	2,81E-06	-2,60E-05	2,20E-05
	Dif.	8,84E-01	3,14E-01	6,79E-01	2,50E-02	3,86E-01	3,67E-01	4,12E-01	7,27E-01	1,54E-01	3,88E-01	4,00E-01
GV5	FEM	-4,20E-07	-9,03E-06	-3,36E-07	-4,65E-01	-5,98E-01	-2,45E+00	1,93E+00	3,96E-06	2,44E-06	-1,88E-05	1,58E-05
	RPIM	-7,83E-07	-1,19E-05	-5,68E-07	-4,76E-01	-8,28E-01	-3,35E+00	2,72E+00	6,83E-06	2,81E-06	-2,60E-05	2,21E-05
	Dif.	8,65E-01	3,13E-01	6,91E-01	2,40E-02	3,84E-01	3,65E-01	4,10E-01	7,26E-01	1,53E-01	3,86E-01	3,99E-01
LV3H	FEM	-4,16E-07	-9,02E-06	-3,38E-07	-4,64E-01	-5,97E-01	-2,45E+00	1,92E+00	3,96E-06	2,44E-06	-1,87E-05	1,58E-05
	RPIM	-7,80E-07	-1,18E-05	-5,70E-07	-4,76E-01	-8,27E-01	-3,35E+00	2,71E+00	6,83E-06	2,81E-06	-2,60E-05	2,21E-05
	Dif.	8,74E-01	3,13E-01	6,84E-01	2,41E-02	3,85E-01	3,66E-01	4,11E-01	7,27E-01	1,53E-01	3,87E-01	3,99E-01
LKN	FEM	-4,14E-07	-9,01E-06	-3,39E-07	-4,64E-01	-5,97E-01	-2,45E+00	1,92E+00	3,95E-06	2,44E-06	-1,87E-05	1,58E-05
	RPIM	-7,79E-07	-1,18E-05	-5,70E-07	-4,75E-01	-8,27E-01	-3,35E+00	2,71E+00	6,83E-06	2,81E-06	-2,60E-05	2,21E-05
	Dif.	8,80E-01	3,14E-01	6,80E-01	2,46E-02	3,86E-01	3,67E-01	4,11E-01	7,27E-01	1,54E-01	3,87E-01	4,00E-01

Table 41: Obtained local values for the MMC at point 7 for distinct nylon materials.

Mat.	Method	ux	uy	uz	σ_1	σ_2	σ_3	σ_{ef}	ϵ_1	ϵ_2	ϵ_3	ϵ_{ef}
L20H	FEM	-2,34E-04	-3,48E-04	-7,08E-05	9,84E+01	4,00E+01	3,54E+01	6,08E+01	6,66E-04	-1,43E-06	-5,34E-05	5,45E-04
	RPIM	-3,08E-04	-4,42E-04	-8,94E-05	1,28E+02	5,19E+01	4,67E+01	7,90E+01	8,66E-04	-4,69E-06	-6,44E-05	7,09E-04
	Dif.	3,19E-01	2,69E-01	2,64E-01	3,03E-01	2,99E-01	3,19E-01	3,00E-01	3,02E-01	2,29E+00	2,06E-01	3,01E-01
GV5	FEM	-2,33E-04	-3,48E-04	-7,01E-05	9,82E+01	3,99E+01	3,54E+01	6,07E+01	6,65E-04	-1,53E-06	-5,33E-05	5,45E-04
	RPIM	-3,08E-04	-4,41E-04	-8,89E-05	1,28E+02	5,19E+01	4,67E+01	7,89E+01	8,66E-04	-4,69E-06	-6,43E-05	7,09E-04
	Dif.	3,20E-01	2,70E-01	2,69E-01	3,04E-01	3,00E-01	3,19E-01	3,00E-01	3,02E-01	2,06E+00	2,06E-01	3,02E-01
LV3H	FEM	-2,34E-04	-3,48E-04	-7,05E-05	9,83E+01	3,99E+01	3,54E+01	6,08E+01	6,65E-04	-1,48E-06	-5,34E-05	5,45E-04
	RPIM	-3,08E-04	-4,42E-04	-8,92E-05	1,28E+02	5,19E+01	4,67E+01	7,90E+01	8,66E-04	-4,68E-06	-6,44E-05	7,09E-04
	Dif.	3,20E-01	2,69E-01	2,66E-01	3,04E-01	3,00E-01	3,19E-01	3,00E-01	3,02E-01	2,16E+00	2,06E-01	3,01E-01
LKN	FEM	-2,34E-04	-3,48E-04	-7,07E-05	9,83E+01	4,00E+01	3,54E+01	6,08E+01	6,65E-04	-1,45E-06	-5,34E-05	5,45E-04
	RPIM	-3,08E-04	-4,42E-04	-8,94E-05	1,28E+02	5,19E+01	4,67E+01	7,90E+01	8,66E-04	-4,68E-06	-6,44E-05	7,09E-04
	Dif.	3,19E-01	2,69E-01	2,64E-01	3,03E-01	3,00E-01	3,19E-01	3,00E-01	3,02E-01	2,24E+00	2,06E-01	3,01E-01

Table 42: Obtained local values for the MMC at point 8 for distinct nylon materials.

Mat.	Method	ux	uy	uz	σ_1	σ_2	σ_3	σ_{ef}	ϵ_1	ϵ_2	ϵ_3	ϵ_{ef}
L20H	FEM	-2,14E-04	-3,27E-04	-6,80E-05	7,94E+01	3,31E+01	2,88E+01	4,86E+01	5,35E-04	5,93E-06	-4,39E-05	4,38E-04
	RPIM	-2,77E-04	-4,19E-04	-8,56E-05	9,84E+01	4,08E+01	3,65E+01	5,98E+01	6,61E-04	3,40E-06	-4,65E-05	5,41E-04
	Dif.	2,96E-01	2,79E-01	2,59E-01	2,39E-01	2,33E-01	2,69E-01	2,31E-01	2,36E-01	4,26E-01	5,69E-02	2,34E-01
GV5	FEM	-2,13E-04	-3,27E-04	-6,73E-05	7,93E+01	3,31E+01	2,87E+01	4,86E+01	5,34E-04	5,83E-06	-4,39E-05	4,38E-04
	RPIM	-2,77E-04	-4,18E-04	-8,51E-05	9,83E+01	4,08E+01	3,65E+01	5,98E+01	6,60E-04	3,40E-06	-4,64E-05	5,40E-04
	Dif.	2,97E-01	2,79E-01	2,64E-01	2,39E-01	2,34E-01	2,69E-01	2,31E-01	2,36E-01	4,17E-01	5,78E-02	2,35E-01
LV3H	FEM	-2,13E-04	-3,27E-04	-6,77E-05	7,94E+01	3,31E+01	2,87E+01	4,86E+01	5,34E-04	5,87E-06	-4,39E-05	4,38E-04
	RPIM	-2,77E-04	-4,19E-04	-8,54E-05	9,84E+01	4,08E+01	3,65E+01	5,98E+01	6,60E-04	3,41E-06	-4,64E-05	5,41E-04
	Dif.	2,97E-01	2,79E-01	2,62E-01	2,39E-01	2,34E-01	2,69E-01	2,31E-01	2,36E-01	4,19E-01	5,72E-02	2,35E-01
LKN	FEM	-2,14E-04	-3,27E-04	-6,79E-05	7,94E+01	3,31E+01	2,88E+01	4,86E+01	5,35E-04	5,91E-06	-4,39E-05	4,38E-04
	RPIM	-2,77E-04	-4,19E-04	-8,55E-05	9,84E+01	4,08E+01	3,65E+01	5,98E+01	6,61E-04	3,41E-06	-4,64E-05	5,41E-04
	Dif.	2,96E-01	2,79E-01	2,60E-01	2,39E-01	2,33E-01	2,69E-01	2,31E-01	2,36E-01	4,23E-01	5,70E-02	2,35E-01

Table 43: Obtained local values for the MMC at point 9 for distinct nylon materials.

Mat.	Method	ux	uy	uz	σ_1	σ_2	σ_3	σ_{ef}	ϵ_1	ϵ_2	ϵ_3	ϵ_{ef}
L20H	FEM	-1,95E-04	-3,10E-04	-6,54E-05	8,56E+01	3,69E+01	3,16E+01	5,16E+01	5,72E-04	1,54E-05	-4,53E-05	4,69E-04
	RPIM	-2,50E-04	-3,99E-04	-8,28E-05	9,23E+01	3,94E+01	3,40E+01	5,58E+01	6,18E-04	1,32E-05	-4,85E-05	5,06E-04
	Dif.	2,80E-01	2,88E-01	2,65E-01	7,78E-02	6,69E-02	7,55E-02	8,20E-02	8,00E-02	1,40E-01	6,88E-02	7,98E-02
GV5	FEM	-1,95E-04	-3,09E-04	-6,48E-05	8,55E+01	3,69E+01	3,16E+01	5,15E+01	5,71E-04	1,53E-05	-4,53E-05	4,68E-04
	RPIM	-2,50E-04	-3,99E-04	-8,23E-05	9,22E+01	3,94E+01	3,40E+01	5,58E+01	6,17E-04	1,32E-05	-4,84E-05	5,06E-04
	Dif.	2,81E-01	2,88E-01	2,70E-01	7,83E-02	6,76E-02	7,59E-02	8,23E-02	8,04E-02	1,35E-01	6,98E-02	8,02E-02
LV3H	FEM	-1,95E-04	-3,10E-04	-6,52E-05	8,56E+01	3,69E+01	3,16E+01	5,16E+01	5,72E-04	1,53E-05	-4,53E-05	4,68E-04
	RPIM	-2,50E-04	-3,99E-04	-8,26E-05	9,23E+01	3,94E+01	3,40E+01	5,58E+01	6,17E-04	1,32E-05	-4,84E-05	5,06E-04
	Dif.	2,81E-01	2,88E-01	2,67E-01	7,80E-02	6,73E-02	7,57E-02	8,21E-02	8,02E-02	1,37E-01	6,93E-02	8,00E-02
LKN	FEM	-1,95E-04	-3,10E-04	-6,54E-05	8,56E+01	3,69E+01	3,16E+01	5,16E+01	5,72E-04	1,53E-05	-4,53E-05	4,69E-04
	RPIM	-2,50E-04	-3,99E-04	-8,27E-05	9,23E+01	3,94E+01	3,40E+01	5,58E+01	6,18E-04	1,32E-05	-4,85E-05	5,06E-04
	Dif.	2,80E-01	2,88E-01	2,65E-01	7,79E-02	6,70E-02	7,55E-02	8,20E-02	8,01E-02	1,39E-01	6,89E-02	7,99E-02

Table 44: Obtained local values for the MMC at point 10 for distinct nylon materials

Mat.	Method	ux	uy	uz	σ_1	σ_2	σ_3	σ_{ef}	ϵ_1	ϵ_2	ϵ_3	ϵ_{ef}
L20H	FEM	-6,62E-04	-2,70E-04	-3,17E-05	-5,77E-02	-9,37E-02	-5,33E-01	4,59E-01	1,63E-06	-4,55E-06	-1,30E-05	1,13E-05
	RPIM	-8,60E-04	-3,41E-04	-4,20E-05	-1,75E-03	-6,03E-02	-3,93E-01	3,65E-01	4,02E-06	1,26E-06	-9,96E-06	8,83E-06
	Dif.	2,99E-01	2,62E-01	3,25E-01	9,70E-01	3,56E-01	2,63E-01	2,03E-01	1,47E+00	1,28E+00	2,35E-01	2,21E-01
GV5	FEM	-6,60E-04	-2,66E-04	-3,12E-05	-2,57E-02	-6,23E-02	-3,36E-01	2,94E-01	1,66E-06	7,44E-07	-5,64E-06	4,84E-06
	RPIM	-8,58E-04	-3,39E-04	-4,17E-05	-4,36E-04	-5,80E-02	-3,40E-01	3,15E-01	2,35E-06	7,31E-07	-6,02E-06	5,31E-06
	Dif.	3,01E-01	2,73E-01	3,36E-01	9,83E-01	6,92E-02	1,03E-02	6,97E-02	4,18E-01	1,74E-02	6,63E-02	9,68E-02
LV3H	FEM	-6,61E-04	-2,68E-04	-3,15E-05	-4,27E-02	-7,72E-02	-4,19E-01	3,60E-01	1,47E-06	9,96E-07	-8,29E-06	6,92E-06
	RPIM	-8,59E-04	-3,40E-04	-4,19E-05	-4,32E-03	-6,23E-02	-3,79E-01	3,49E-01	3,09E-06	1,00E-06	-8,13E-06	7,15E-06
	Dif.	3,00E-01	2,69E-01	3,30E-01	8,99E-01	1,93E-01	9,45E-02	2,94E-02	1,10E+00	7,56E-03	1,91E-02	3,29E-02
LKN	FEM	-6,62E-04	-2,70E-04	-3,16E-05	-5,25E-02	-8,76E-02	-4,90E-01	4,21E-01	1,46E-06	-7,51E-07	-1,06E-05	8,77E-06
	RPIM	-8,60E-04	-3,41E-04	-4,20E-05	-2,94E-03	-6,15E-02	-3,92E-01	3,64E-01	3,64E-06	1,18E-06	-9,34E-06	8,24E-06
	Dif.	2,99E-01	2,65E-01	3,26E-01	9,44E-01	2,98E-01	1,99E-01	1,36E-01	1,49E+00	2,57E+00	1,20E-01	6,03E-02

For the study regarding the different materials, the differences between the FEM and the RPIM still increase with the distance to the boundary condition. For points P1, P2 and P3, being closer to the clamped zone the difference values between FEM and RPIM increase despite the different type of material used on the nylon sleeve. However, there are some problems again with some values, such as, for P1 the principal stress σ_{22} , for P2 the principal stress σ_{11} and for P3 (the point closer the boundary condition mentioned before) the displacements u_x and u_z and the principal strain ε_{11} .

Relative to the points (P7, P8 and P9) near the simple supporter boundary condition the differences are around 25% for almost all the values, with exception for the principal strain ε_{22} .

We can note that changing the type of material on the nylon sleeve will not have a big influence in the abutment, where the points in study are located.

Therefore, for the point 10 (inside the domain of the nylon sleeve), the differences for both numerical methods continue around 30% and in some cases even less. However, for all the types of nylons used the principal stress σ_{11} has problems and also for the materials L20H and LKN the principal strains ε_{11} and ε_{22} .

Table 45: Stress distribution map on abutment for MCC regarding the distinct nylon materials. Effective stress (Von Mises), principal stress σ_{11} and principal stress σ_{33} , respectively. [MPa]

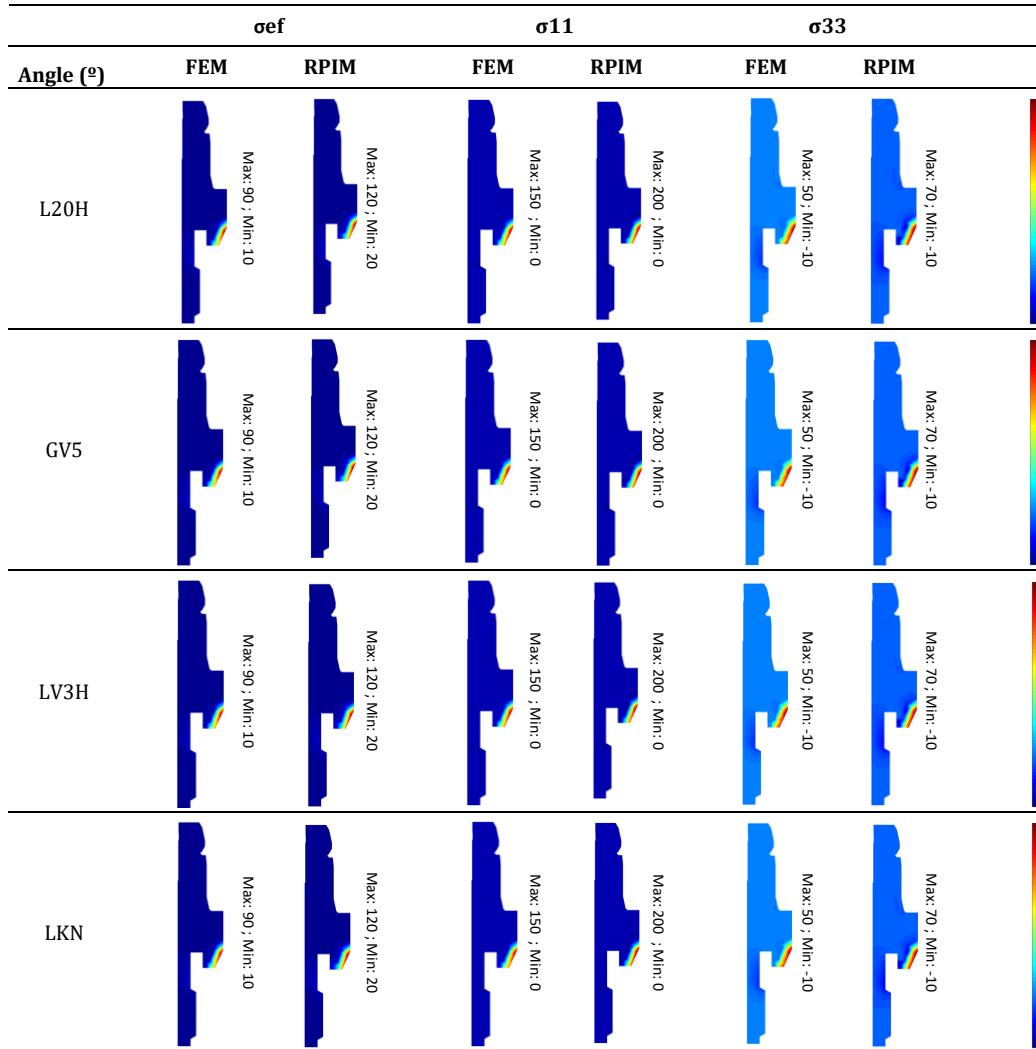


Table 46: Strain distribution map on abutment for MCC regarding the distinct nylon materials. Effective strain (Von Mises), principal strain ϵ_{11} and principal strain ϵ_{33} , respectively.

























Angle (°)	ϵ_{ef}		ϵ_{11}		ϵ_{33}	
	FEM	RPIM	FEM	RPIM	FEM	RPIM
L20H	 Max: 11E-4 ; Min: 1E-4	 Max: 8E-4 ; Min: 1E-4	 Max: 10E-4 ; Min: 1E-4	 Max: 12E-4 ; Min: 0E-4	 Max: 0E-5 ; Min: -12E-5	 Max: -2E-5 ; Min: -12E-5
GV5	 Max: 8E-4 ; Min: 1E-4	 Max: 12E-4 ; Min: 2E-4	 Max: 10E-4 ; Min: 1E-4	 Max: 12E-4 ; Min: 2E-4	 Max: -2E-5 ; Min: -12E-5	 Max: -2E-5 ; Min: -12E-5
LV3H	 Max: 8E-4 ; Min: 1E-4	 Max: 11E-4 ; Min: 1E-4	 Max: 10E-4 ; Min: 1E-4	 Max: 12E-4 ; Min: 2E-4	 Max: -2E-5 ; Min: -12E-5	 Max: -2E-5 ; Min: -12E-5
LKN	 Max: 8E-4 ; Min: 1E-4	 Max: 11E-4 ; Min: 1E-4	 Max: 10E-4 ; Min: 1E-4	 Max: 12E-4 ; Min: 0E-4	 Max: 0E-5 ; Min: -12E-5	 Max: -2E-5 ; Min: -12E-5

Table 47: Stress distribution map on nylon sleeve for MCC regarding the distinct nylon materials. Effective stress (Von Mises), principal stress σ_{11} and principal stress σ_{33} , respectively. [MPa]

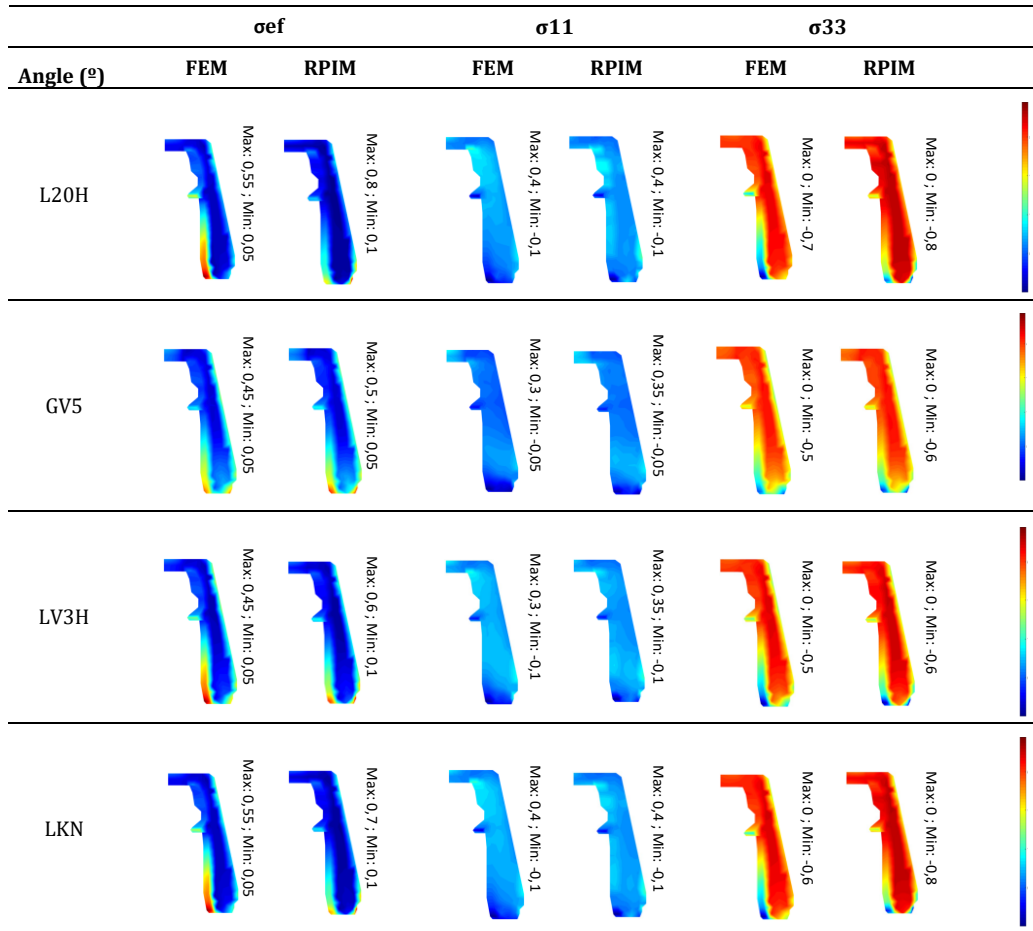


Table 48: Strain distribution map on nylon sleeve for MCC regarding the distinct nylon materials. Effective strain (Von Mises), principal strain ϵ_{11} and principal strain ϵ_{33} , respectively.

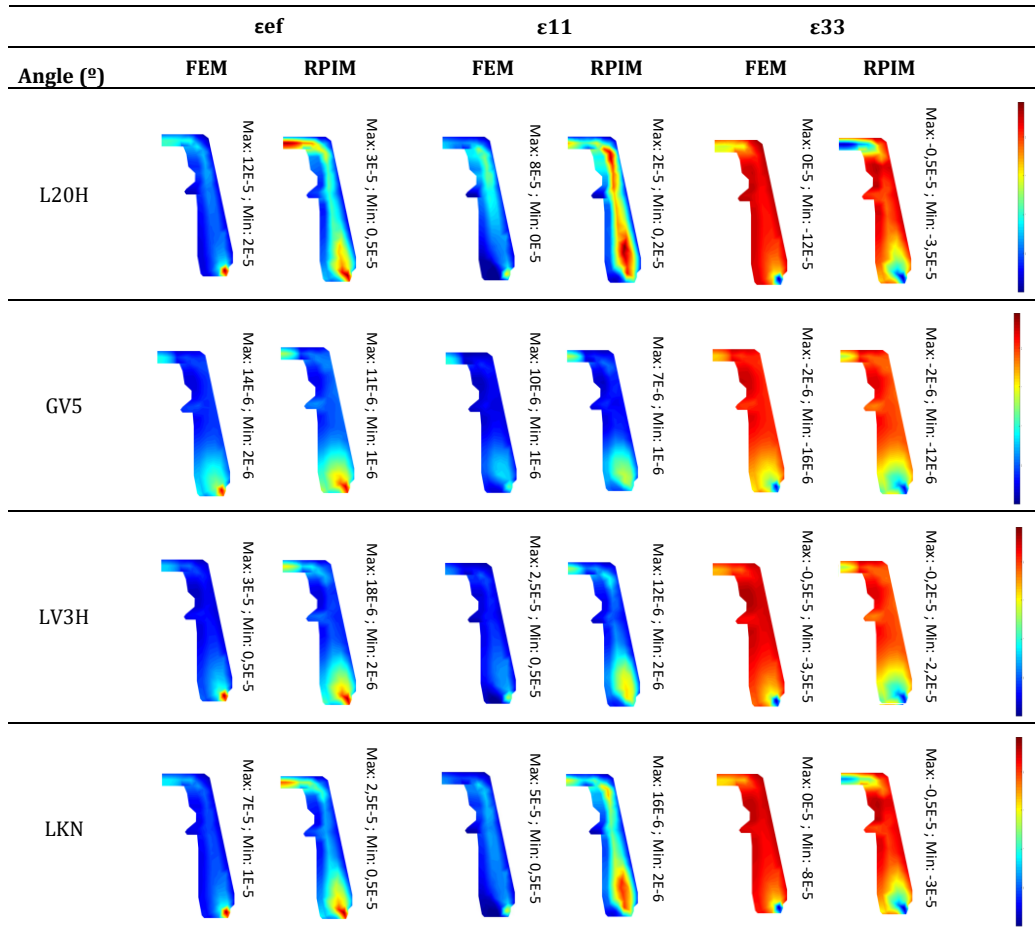


Table 49: Stress distribution map on titanium sleeve for MCC regarding the distinct nylon materials. Effective stress (Von Mises), principal stress σ_{11} and principal stress σ_{33} , respectively. [MPa]

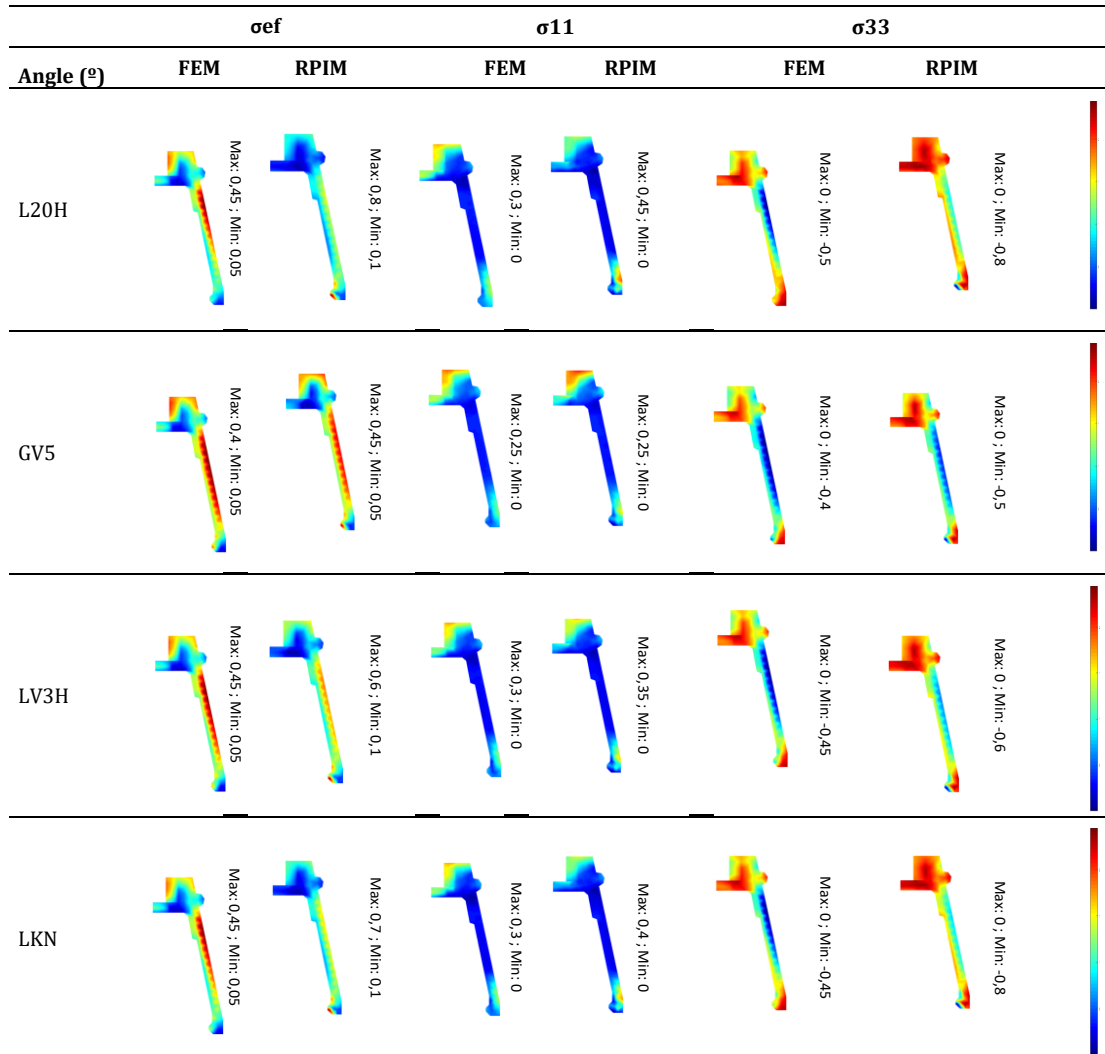
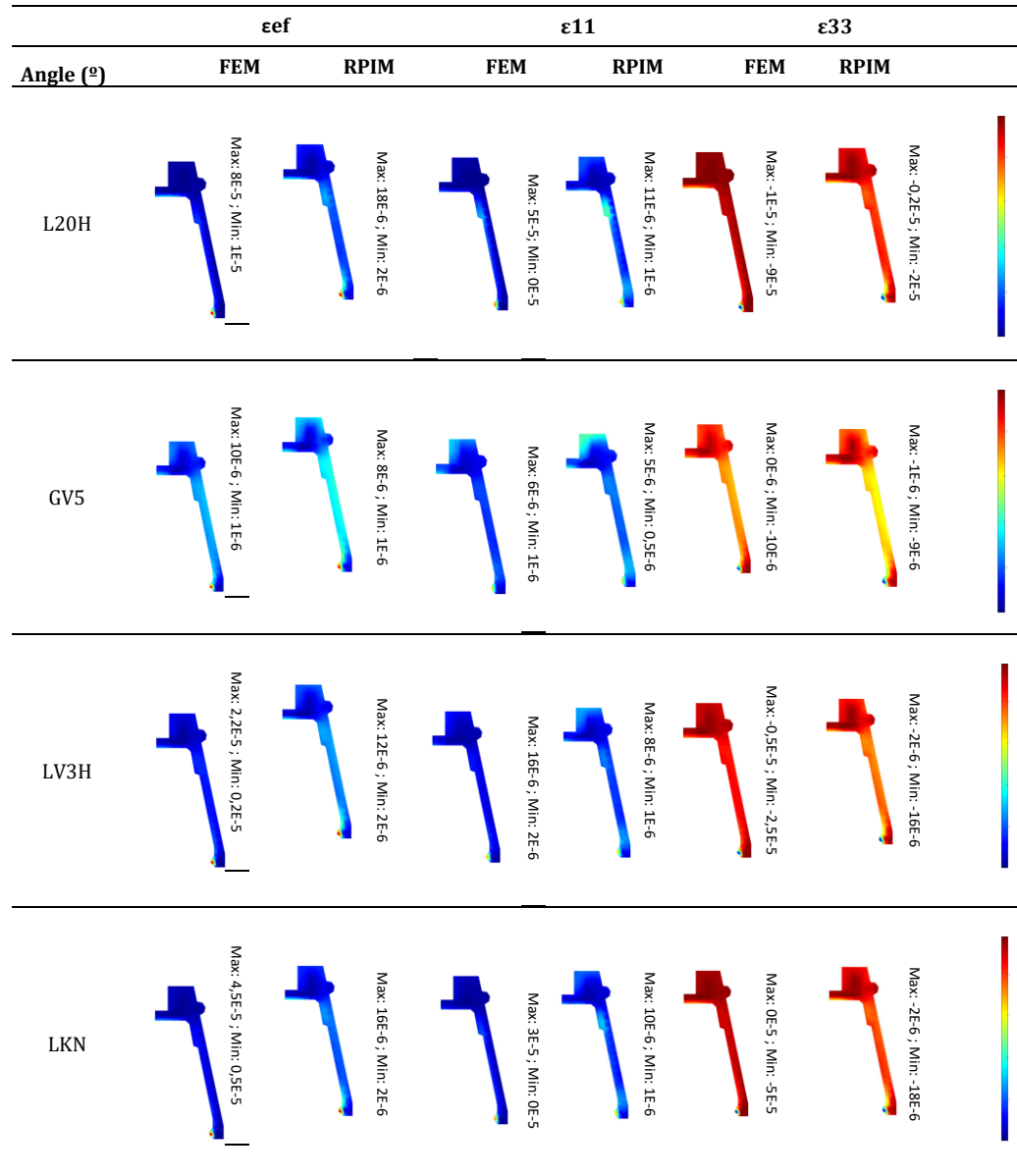


Table 50: Strain distribution map on titanium sleeve for MCC regarding the distinct nylon materials. Effective strain (Von Mises), principal strain ϵ_{11} and principal strain ϵ_{33} , respectively.



Despite the different types of nylon used, the more delicate zone for all the three parts that constitute the dental implant continues the same zone mentioned in section 6.3, showing an identical problem of the excessive values for stresses and strains.

For the nylon sleeve in specific, where the material is changed, the maximum effective stress von Mises obtained is 0.55 MPa, see Table 47. Knowing that for that case the yield stress is 40 MPa, see Table 4, and the angle applied is 45° we will assume that the applied masticatory load is about 60 N in this direction, therefore $0.55 \times 60 = 33 < 40$ MPa, meaning that the nylon sleeve will handle the loads. However, the value is really close to the yield stress.

The results also show that the higher the young modulus E , the lower the strains are, as it is possible to observe in the Figure 32.

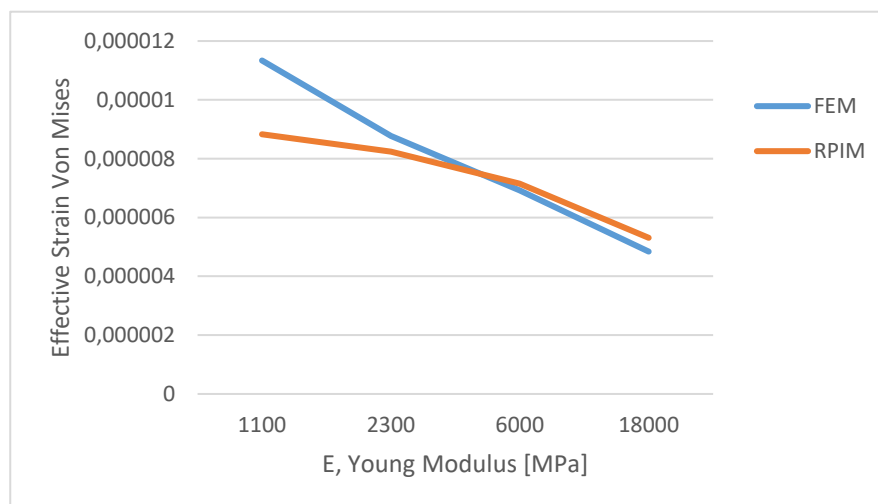


Figure 32: Effective Strain Von Mises trend, using different types of nylons

6.5.2 Mechanical Case D

For the different type of nylons, more precisely the *GV5*, *LV3H* and *LKN*, there were measured the local stresses and strains in the interest points line, which are possible to observe in Table 51, Table 52 and Table 53, respectively. Besides that, to better understand these measured values, supplementary graphics are presented, showing the variation of the stress and strain, along the interest line points for the all four types of nylons, as shown in Figure 33 and Figure 34 respectively.

For illustrating the stress and strain distribution in the complete domain, stress and strain maps are presented, respectively, permitting to visually compare the RPIM and FEM solutions for the different types of nylons and for all the three parts that constitute the dental implant. For the abutment, see Table 55 and Table 56. To the nylon sleeve observe Table 57 and Table 58. Observe Table 59 and Table 60 for the titanium sleeve.

For the point 10, inside the domain of the nylon sleeve, the measured stresses and strain can be observed in Table 44 and Table 54, respectively.

Table 51: Obtained local values for the MCD at the interest points line for nylon GV5

y coord.	Method	σ_1	σ_2	σ_3	σ_{ef}	ϵ_1	ϵ_2	ϵ_3	ϵ_{ef}
-4,6296	FEM	2,93E-01	-2,92E-02	-3,66E-01	5,71E-01	3,61E-06	-6,39E-08	-3,91E-06	4,35E-06
	RPIM	3,92E-01	7,71E-04	-3,94E-01	6,80E-01	4,48E-06	1,19E-08	-4,50E-06	5,18E-06
	Dif.	3,38E-01	1,03E+00	7,61E-02	1,93E-01	2,39E-01	1,19E+00	1,50E-01	1,92E-01
-4,283	FEM	7,85E-01	-2,34E-01	-9,92E-01	1,54E+00	1,01E-05	-1,51E-06	-1,02E-05	1,18E-05
	RPIM	1,10E+00	7,32E-03	-1,10E+00	1,90E+00	1,25E-05	7,66E-08	-1,26E-05	1,45E-05
	Dif.	3,99E-01	1,03E+00	1,11E-01	2,34E-01	2,37E-01	1,05E+00	2,39E-01	2,31E-01
-3,9497	FEM	1,37E+00	-2,34E-02	-1,40E+00	2,39E+00	1,57E-05	-1,29E-07	-1,58E-05	1,82E-05
	RPIM	1,52E+00	7,45E-03	-1,50E+00	2,61E+00	1,73E-05	9,23E-09	-1,72E-05	1,99E-05
	Dif.	1,10E-01	1,32E+00	7,16E-02	9,07E-02	9,56E-02	1,07E+00	8,58E-02	9,07E-02
-3,6163	FEM	1,36E+00	1,21E-01	-1,30E+00	2,31E+00	1,51E-05	9,07E-07	-1,54E-05	1,76E-05
	RPIM	1,52E+00	1,84E-03	-1,52E+00	2,64E+00	1,74E-05	7,98E-09	-1,74E-05	2,01E-05
	Dif.	1,18E-01	9,85E-01	1,67E-01	1,41E-01	1,53E-01	9,91E-01	1,32E-01	1,41E-01
-3,283	FEM	1,35E+00	-2,40E-01	-1,51E+00	2,49E+00	1,65E-05	-1,68E-06	-1,62E-05	1,90E-05
	RPIM	1,56E+00	-3,56E-03	-1,56E+00	2,70E+00	1,78E-05	-2,74E-08	-1,78E-05	2,06E-05
	Dif.	1,53E-01	9,85E-01	3,00E-02	8,60E-02	7,99E-02	9,84E-01	9,66E-02	8,53E-02
-2,9497	FEM	1,48E+00	1,31E-01	-1,40E+00	2,50E+00	1,64E-05	9,19E-07	-1,65E-05	1,90E-05
	RPIM	1,58E+00	3,46E-03	-1,57E+00	2,72E+00	1,80E-05	1,06E-09	-1,79E-05	2,08E-05
	Dif.	6,37E-02	9,74E-01	1,23E-01	9,18E-02	9,89E-02	9,99E-01	8,61E-02	9,16E-02
-2,6163	FEM	1,50E+00	1,29E-01	-1,44E+00	2,54E+00	1,66E-05	9,84E-07	-1,69E-05	1,94E-05
	RPIM	1,67E+00	2,87E-03	-1,67E+00	2,89E+00	1,90E-05	2,76E-08	-1,91E-05	2,20E-05
	Dif.	1,14E-01	9,78E-01	1,58E-01	1,35E-01	1,47E-01	9,72E-01	1,25E-01	1,35E-01
-2,283	FEM	7,52E-01	-6,07E-02	-8,77E-01	1,41E+00	9,08E-06	-2,03E-07	-9,53E-06	1,08E-05
	RPIM	1,03E+00	2,52E-03	-1,07E+00	1,82E+00	1,19E-05	1,07E-07	-1,21E-05	1,39E-05
	Dif.	3,76E-01	1,04E+00	2,16E-01	2,90E-01	3,10E-01	1,53E+00	2,70E-01	2,89E-01

Table 52: Obtained local values for the MCD at the interest points line for nylon LV3H

y coord.	Method	σ_1	σ_2	σ_3	σ_{ef}	ϵ_1	ϵ_2	ϵ_3	ϵ_{ef}
-4,6296	FEM	2,93E-01	-2,92E-02	-3,66E-01	5,71E-01	3,61E-06	-6,39E-08	-3,91E-06	4,35E-06
	RPIM	3,92E-01	7,71E-04	-3,94E-01	6,81E-01	4,48E-06	1,19E-08	-4,50E-06	5,18E-06
	Dif.	3,39E-01	1,03E+00	7,67E-02	1,93E-01	2,40E-01	1,19E+00	1,50E-01	1,92E-01
-4,283	FEM	7,85E-01	-2,34E-01	-9,92E-01	1,54E+00	1,01E-05	-1,51E-06	-1,02E-05	1,18E-05
	RPIM	1,10E+00	7,33E-03	-1,10E+00	1,91E+00	1,25E-05	7,66E-08	-1,26E-05	1,45E-05
	Dif.	4,00E-01	1,03E+00	1,11E-01	2,34E-01	2,38E-01	1,05E+00	2,39E-01	2,32E-01
-3,9497	FEM	1,37E+00	-2,34E-02	-1,40E+00	2,39E+00	1,57E-05	-1,29E-07	-1,58E-05	1,82E-05
	RPIM	1,52E+00	7,45E-03	-1,50E+00	2,61E+00	1,73E-05	9,23E-09	-1,72E-05	1,99E-05
	Dif.	1,11E-01	1,32E+00	7,22E-02	9,12E-02	9,61E-02	1,07E+00	8,64E-02	9,12E-02
-3,6163	FEM	1,36E+00	1,21E-01	-1,30E+00	2,31E+00	1,51E-05	9,07E-07	-1,54E-05	1,76E-05
	RPIM	1,52E+00	1,84E-03	-1,52E+00	2,64E+00	1,74E-05	7,98E-09	-1,74E-05	2,01E-05
	Dif.	1,19E-01	9,85E-01	1,68E-01	1,42E-01	1,53E-01	9,91E-01	1,32E-01	1,42E-01
-3,283	FEM	1,35E+00	-2,40E-01	-1,51E+00	2,49E+00	1,65E-05	-1,68E-06	-1,62E-05	1,90E-05
	RPIM	1,56E+00	-3,56E-03	-1,56E+00	2,70E+00	1,78E-05	-2,74E-08	-1,78E-05	2,06E-05
	Dif.	1,54E-01	9,85E-01	3,05E-02	8,65E-02	8,04E-02	9,84E-01	9,72E-02	8,58E-02
-2,9497	FEM	1,48E+00	1,31E-01	-1,40E+00	2,50E+00	1,64E-05	9,19E-07	-1,65E-05	1,90E-05
	RPIM	1,58E+00	3,46E-03	-1,57E+00	2,73E+00	1,80E-05	1,04E-09	-1,80E-05	2,08E-05
	Dif.	6,42E-02	9,74E-01	1,24E-01	9,24E-02	9,95E-02	9,99E-01	8,67E-02	9,22E-02
-2,6163	FEM	1,50E+00	1,29E-01	-1,44E+00	2,54E+00	1,66E-05	9,84E-07	-1,69E-05	1,94E-05
	RPIM	1,67E+00	2,87E-03	-1,67E+00	2,89E+00	1,90E-05	2,77E-08	-1,91E-05	2,20E-05
	Dif.	1,15E-01	9,78E-01	1,59E-01	1,36E-01	1,47E-01	9,72E-01	1,26E-01	1,35E-01
-2,283	FEM	7,52E-01	-6,08E-02	-8,77E-01	1,41E+00	9,08E-06	-2,03E-07	-9,53E-06	1,08E-05
	RPIM	1,04E+00	2,47E-03	-1,07E+00	1,82E+00	1,19E-05	1,07E-07	-1,21E-05	1,39E-05
	Dif.	3,77E-01	1,04E+00	2,17E-01	2,91E-01	3,11E-01	1,53E+00	2,71E-01	2,90E-01

Table 53: Obtained local values for the MCD at the interest points line for nylon LKN

y coord.	Method	σ_1	σ_2	σ_3	σ_{ef}	ϵ_1	ϵ_2	ϵ_3	ϵ_{ef}
-4,6296	FEM	2,93E-01	-2,92E-02	-3,66E-01	5,71E-01	3,61E-06	-6,39E-08	-3,91E-06	4,35E-06
	RPIM	3,92E-01	7,71E-04	-3,94E-01	6,81E-01	4,48E-06	1,19E-08	-4,50E-06	5,19E-06
	Dif.	3,40E-01	1,03E+00	7,70E-02	1,94E-01	2,40E-01	1,19E+00	1,51E-01	1,93E-01
-4,283	FEM	7,85E-01	-2,34E-01	-9,92E-01	1,54E+00	1,01E-05	-1,51E-06	-1,02E-05	1,18E-05
	RPIM	1,10E+00	7,33E-03	-1,10E+00	1,91E+00	1,25E-05	7,67E-08	-1,26E-05	1,45E-05
	Dif.	4,00E-01	1,03E+00	1,12E-01	2,35E-01	2,38E-01	1,05E+00	2,40E-01	2,32E-01
-3,9497	FEM	1,37E+00	-2,34E-02	-1,40E+00	2,39E+00	1,57E-05	-1,29E-07	-1,58E-05	1,82E-05
	RPIM	1,52E+00	7,45E-03	-1,50E+00	2,61E+00	1,73E-05	9,24E-09	-1,72E-05	1,99E-05
	Dif.	1,11E-01	1,32E+00	7,26E-02	9,16E-02	9,65E-02	1,07E+00	8,68E-02	9,16E-02
-3,6163	FEM	1,36E+00	1,21E-01	-1,30E+00	2,31E+00	1,51E-05	9,07E-07	-1,54E-05	1,76E-05
	RPIM	1,53E+00	1,84E-03	-1,52E+00	2,64E+00	1,74E-05	7,99E-09	-1,74E-05	2,01E-05
	Dif.	1,19E-01	9,85E-01	1,68E-01	1,42E-01	1,54E-01	9,91E-01	1,33E-01	1,42E-01
-3,283	FEM	1,35E+00	-2,40E-01	-1,51E+00	2,49E+00	1,65E-05	-1,68E-06	-1,62E-05	1,90E-05
	RPIM	1,56E+00	-3,56E-03	-1,56E+00	2,70E+00	1,78E-05	-2,74E-08	-1,78E-05	2,06E-05
	Dif.	1,54E-01	9,85E-01	3,09E-02	8,69E-02	8,08E-02	9,84E-01	9,76E-02	8,62E-02
-2,9497	FEM	1,48E+00	1,31E-01	-1,40E+00	2,50E+00	1,64E-05	9,19E-07	-1,65E-05	1,90E-05
	RPIM	1,58E+00	3,46E-03	-1,57E+00	2,73E+00	1,80E-05	1,03E-09	-1,80E-05	2,08E-05
	Dif.	6,46E-02	9,74E-01	1,24E-01	9,28E-02	9,99E-02	9,99E-01	8,71E-02	9,26E-02
-2,6163	FEM	1,50E+00	1,29E-01	-1,44E+00	2,54E+00	1,66E-05	9,84E-07	-1,69E-05	1,94E-05
	RPIM	1,67E+00	2,87E-03	-1,67E+00	2,89E+00	1,91E-05	2,77E-08	-1,91E-05	2,20E-05
	Dif.	1,15E-01	9,78E-01	1,59E-01	1,36E-01	1,48E-01	9,72E-01	1,26E-01	1,36E-01
-2,283	FEM	7,52E-01	-6,08E-02	-8,78E-01	1,41E+00	9,08E-06	-2,03E-07	-9,53E-06	1,08E-05
	RPIM	1,04E+00	2,45E-03	-1,07E+00	1,82E+00	1,19E-05	1,07E-07	-1,21E-05	1,39E-05
	Dif.	3,77E-01	1,04E+00	2,17E-01	2,91E-01	3,11E-01	1,53E+00	2,72E-01	2,91E-01

For the all four types of nylon used, the differences between the methods for the points in the interest line are around 10% - 25%. The exception, for all the cases, are the principal stress σ_{22} and principal strain ε_{22} , which does not possess a significant relevance in the design.

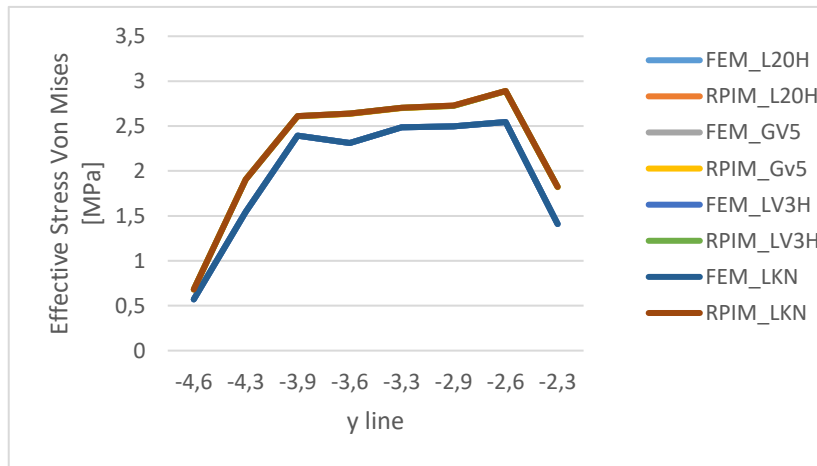
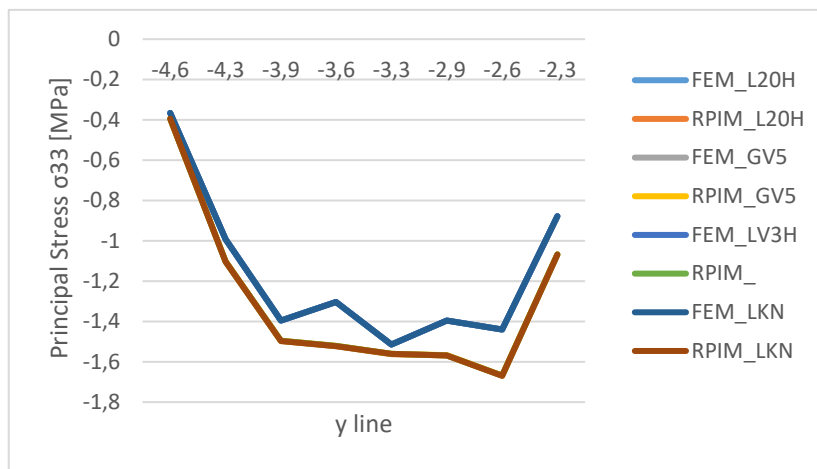
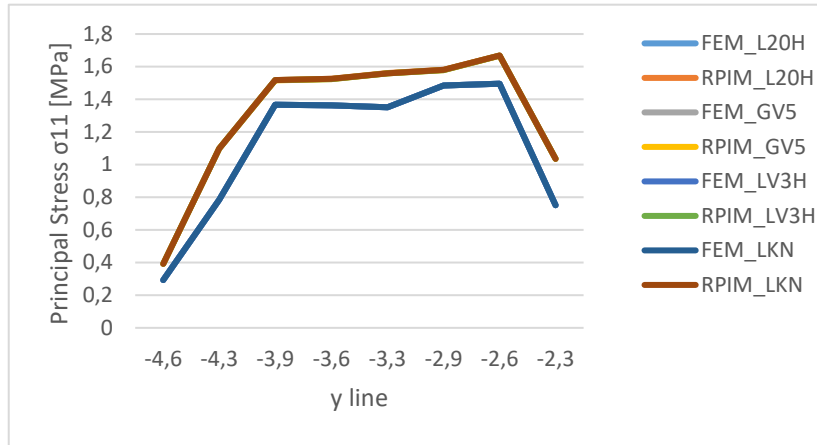


Figure 33: Principal Stress σ_{11} , Principal Stress σ_{33} and Effective Stress (Von Mises), respectively for MCD obtained with both numerical methods along the interest points line for the different nylon materials.

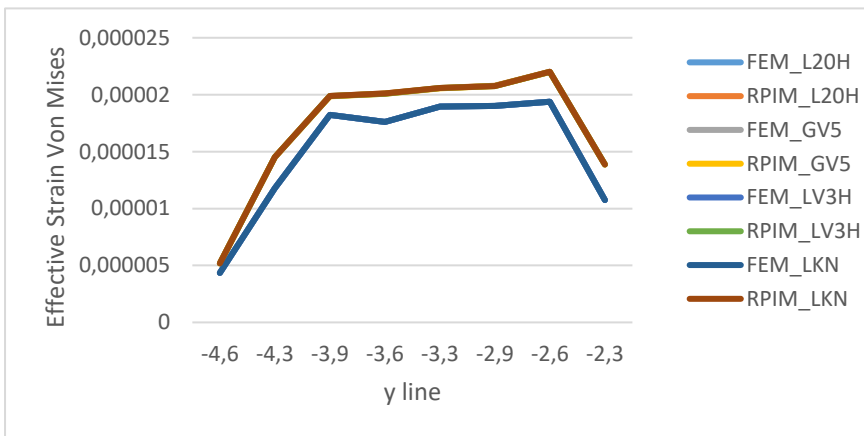
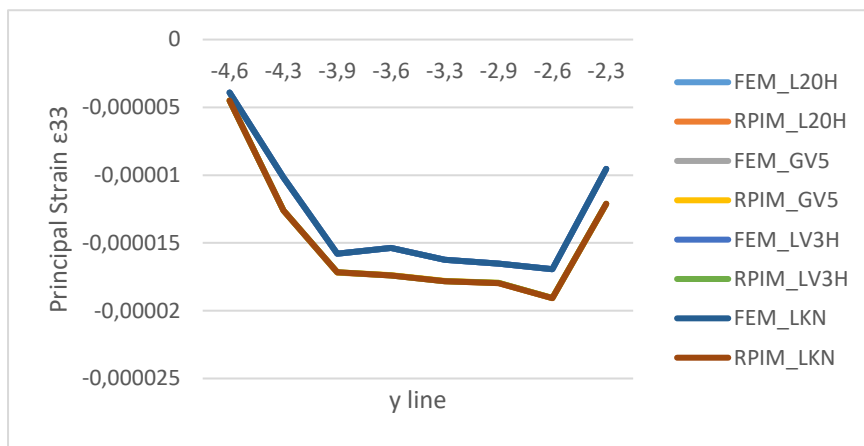
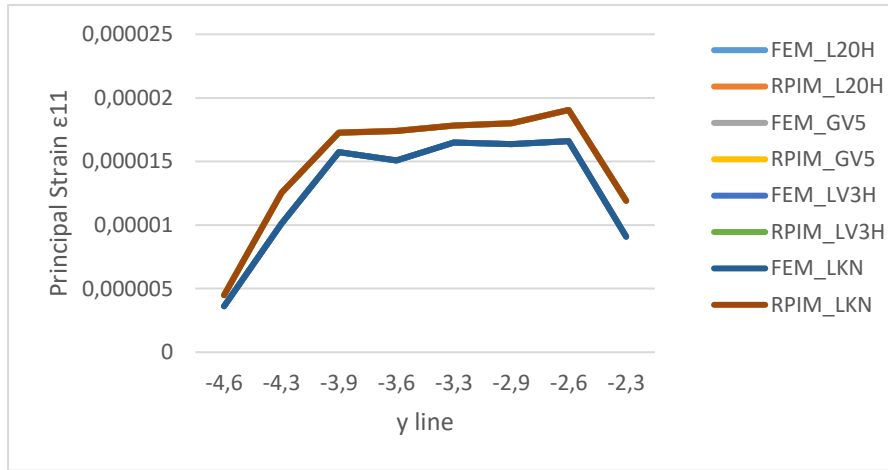


Figure 34: Principal Strain ϵ_{11} , Principal Strain ϵ_{33} and Effective Strain (Von Mises), respectively for MCD obtained with both numerical methods along the interest points line for the different nylon materials

The RPIM solutions and the FEM are all very similar, as Figure 33 and Figure 34 show. This means that the variation of the material properties of nylon do not affect the stress distribution on the titanium.

Table 54: Obtained local values for the MMD at point 10 for distinct nylon materials

Mat.	Method	σ_1	σ_2	σ_3	σ_{ef}	ϵ_1	ϵ_2	ϵ_3	ϵ_{ef}
L20H	FEM	4,03E-02	2,90E-03	-3,49E-02	6,52E-02	4,59E-06	-1,36E-07	-4,49E-06	5,24E-06
	RPIM	1,67E-02	2,11E-04	-1,36E-02	2,63E-02	6,54E-07	6,53E-08	-5,82E-07	7,17E-07
	Dif.	5,86E-01	9,27E-01	6,10E-01	5,96E-01	8,58E-01	1,48E+00	8,70E-01	8,63E-01
GV5	FEM	2,60E-02	1,50E-03	-2,34E-02	4,28E-02	6,56E-07	1,50E-08	-6,45E-07	7,51E-07
	RPIM	2,22E-02	-1,04E-03	-2,14E-02	3,78E-02	5,48E-07	1,95E-09	-5,40E-07	6,28E-07
	Dif.	1,46E-01	1,69E+00	8,60E-02	1,17E-01	1,66E-01	8,70E-01	1,63E-01	1,65E-01
LV3H	FEM	3,20E-02	2,05E-03	-2,82E-02	5,22E-02	1,25E-06	-4,43E-09	-1,22E-06	1,43E-06
	RPIM	2,13E-02	-5,53E-04	-1,95E-02	3,54E-02	6,69E-07	1,11E-08	-6,33E-07	7,52E-07
	Dif.	3,34E-01	1,27E+00	3,11E-01	3,22E-01	4,66E-01	3,50E+00	4,82E-01	4,74E-01
LKN	FEM	3,73E-02	2,58E-03	-3,25E-02	6,04E-02	2,50E-06	-6,14E-08	-2,43E-06	2,84E-06
	RPIM	1,90E-02	-1,02E-04	-1,63E-02	3,06E-02	6,83E-07	3,53E-08	-6,27E-07	7,58E-07
	Dif.	4,90E-01	1,04E+00	4,98E-01	4,93E-01	7,26E-01	1,57E+00	7,42E-01	7,34E-01

Despite the several different nylons used, the same effect verified in section 6.4 appear once again. The differences between the two methods are high for principal stress σ_{22} and principal strain ϵ_{22} . For the other values, the differences continue around 20% - 50%.

Table 55: Stress distribution map on abutment for MCD regarding the distinct nylon materials. Effective stress (Von Mises), principal stress σ_{11} and principal stress σ_{33} , respectively. [MPa]

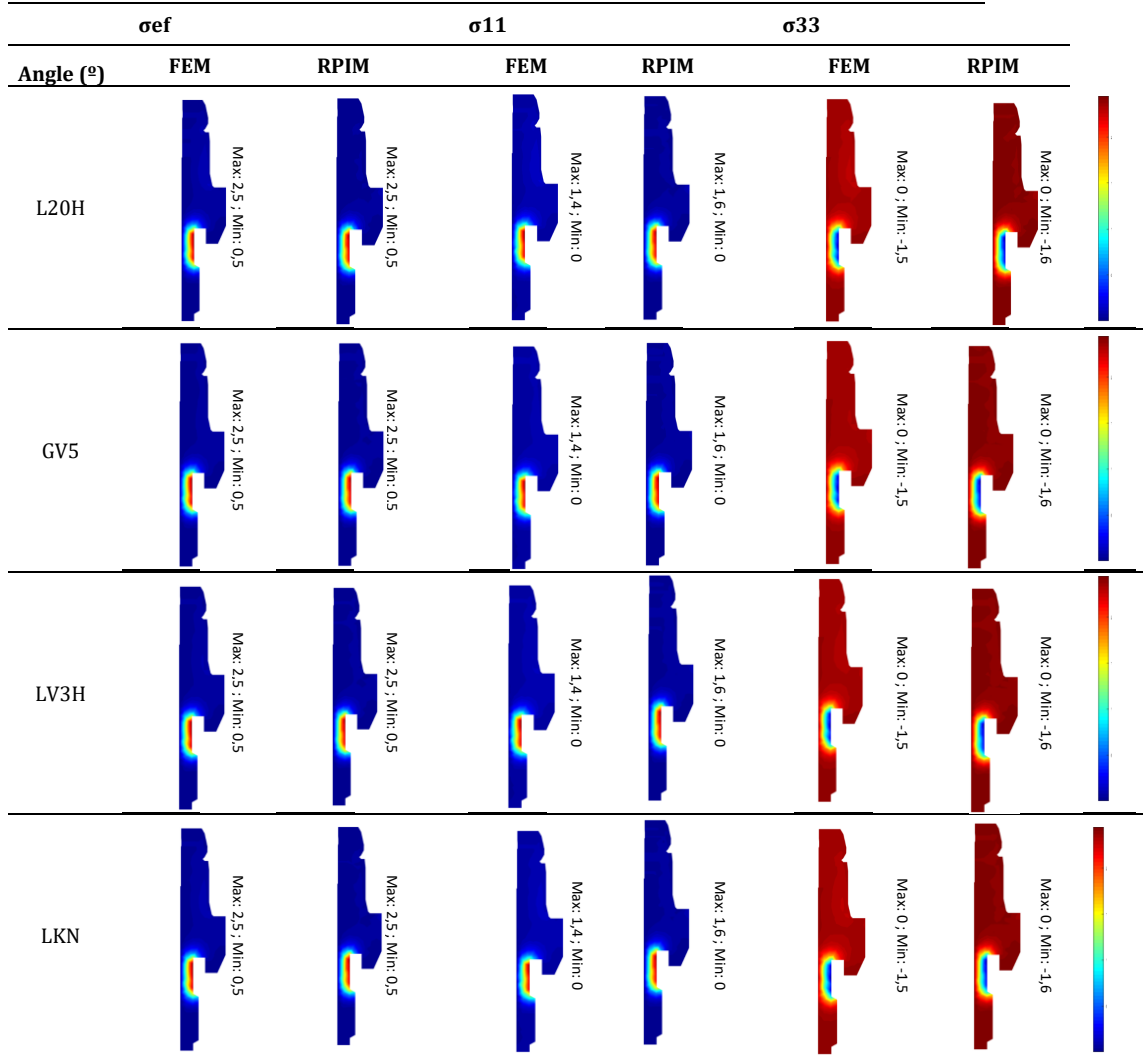


Table 56: Strain distribution map on abutment for MCD regarding the distinct nylon materials. Effective strain (Von Mises), principal strain ϵ_{11} and principal strain ϵ_{33} , respectively

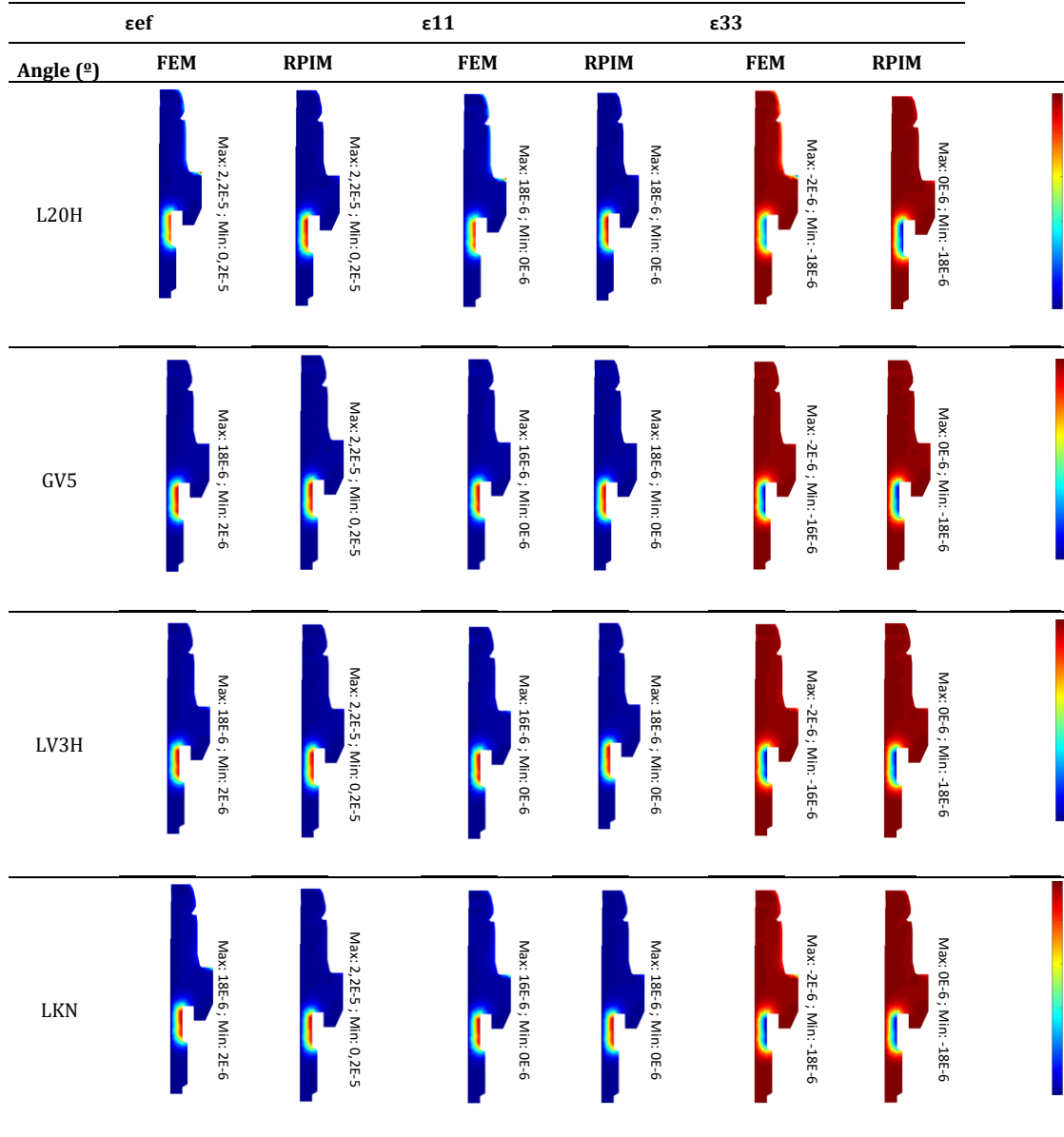


Table 57: Stress distribution map on nylon sleeve for MCD regarding the distinct nylon materials. Effective stress (Von Mises), principal stress σ_{11} and principal stress σ_{33} , respectively. [MPa].

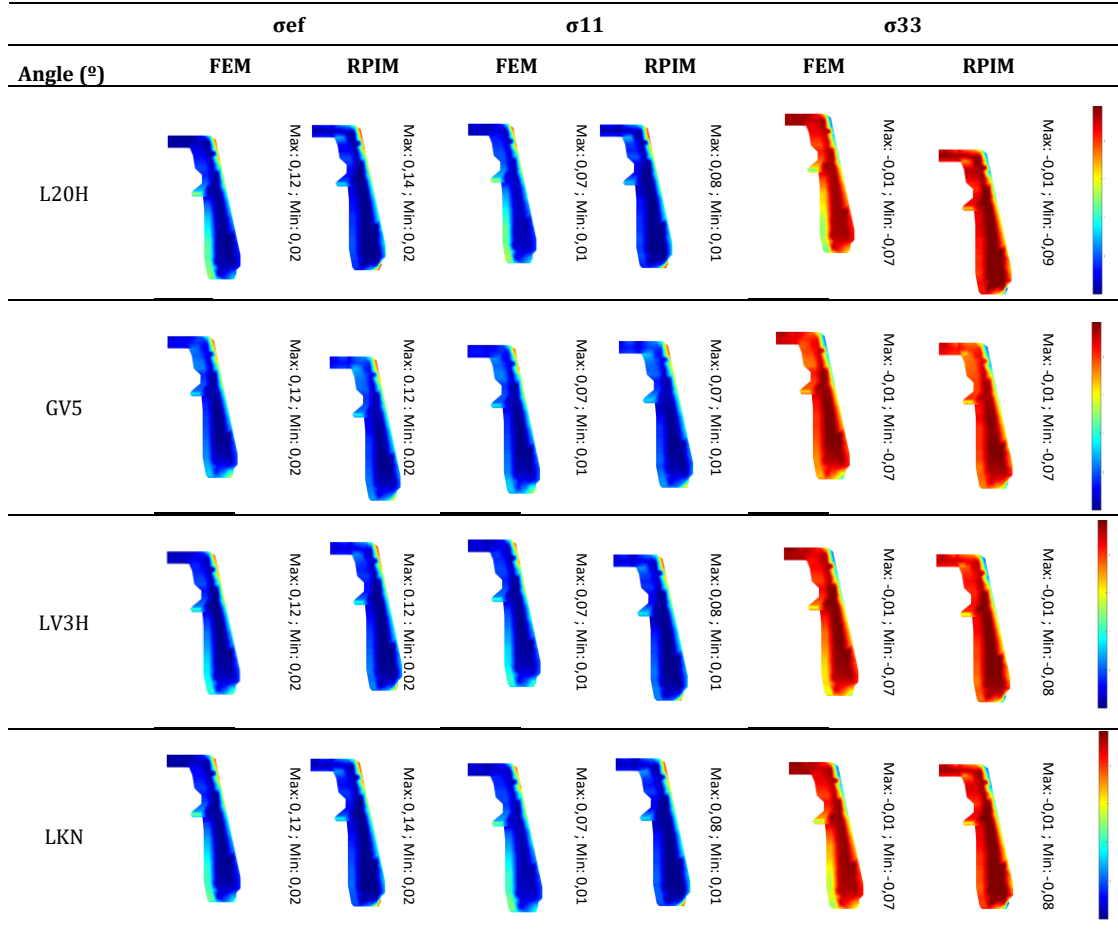


Table 58: Strain distribution map on nylon sleeve for MCD regarding the distinct nylon materials. Effective strain (Von Mises), principal strain ϵ_{11} and principal strain ϵ_{33} , respectively

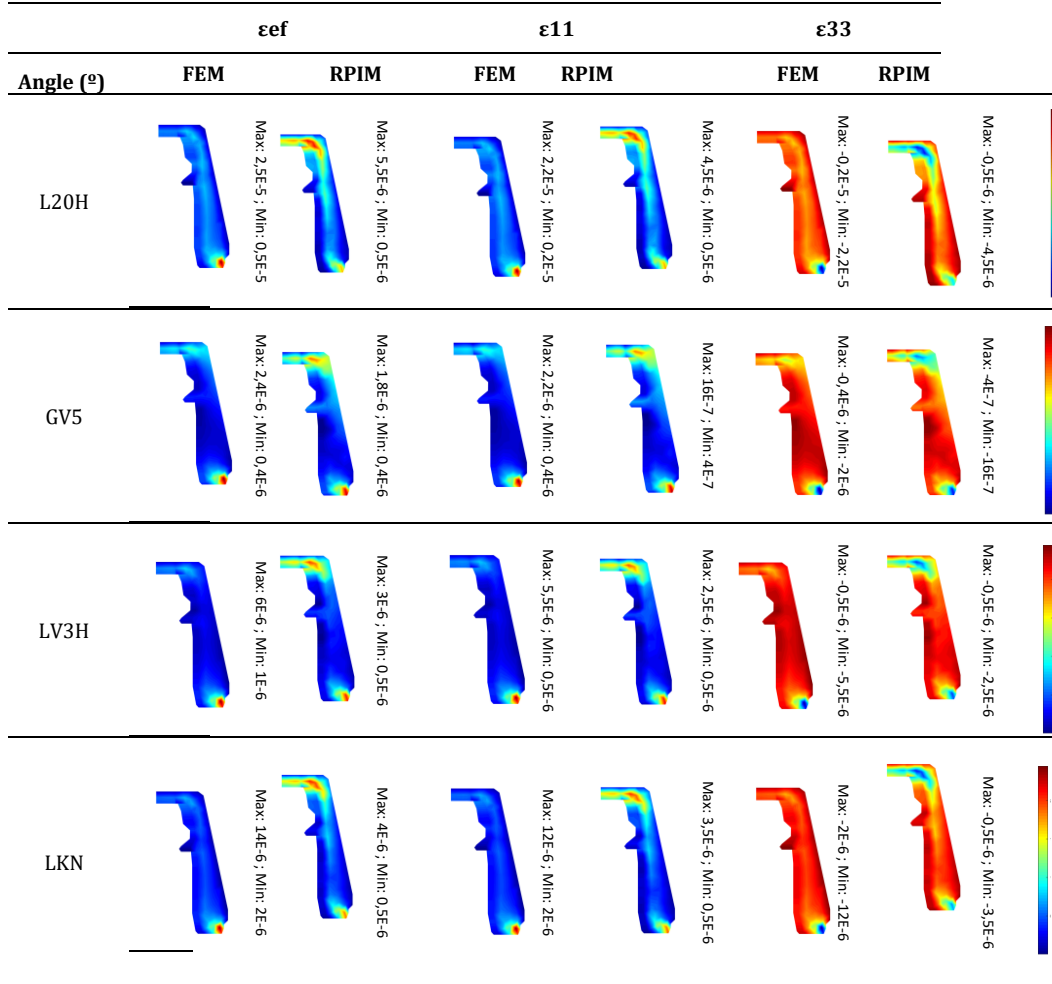


Table 59: Stress distribution map on titanium sleeve for MCD regarding the distinct nylon materials. Effective stress (Von Mises), principal stress σ_{11} and principal stress σ_{33} , respectively. [MPa].

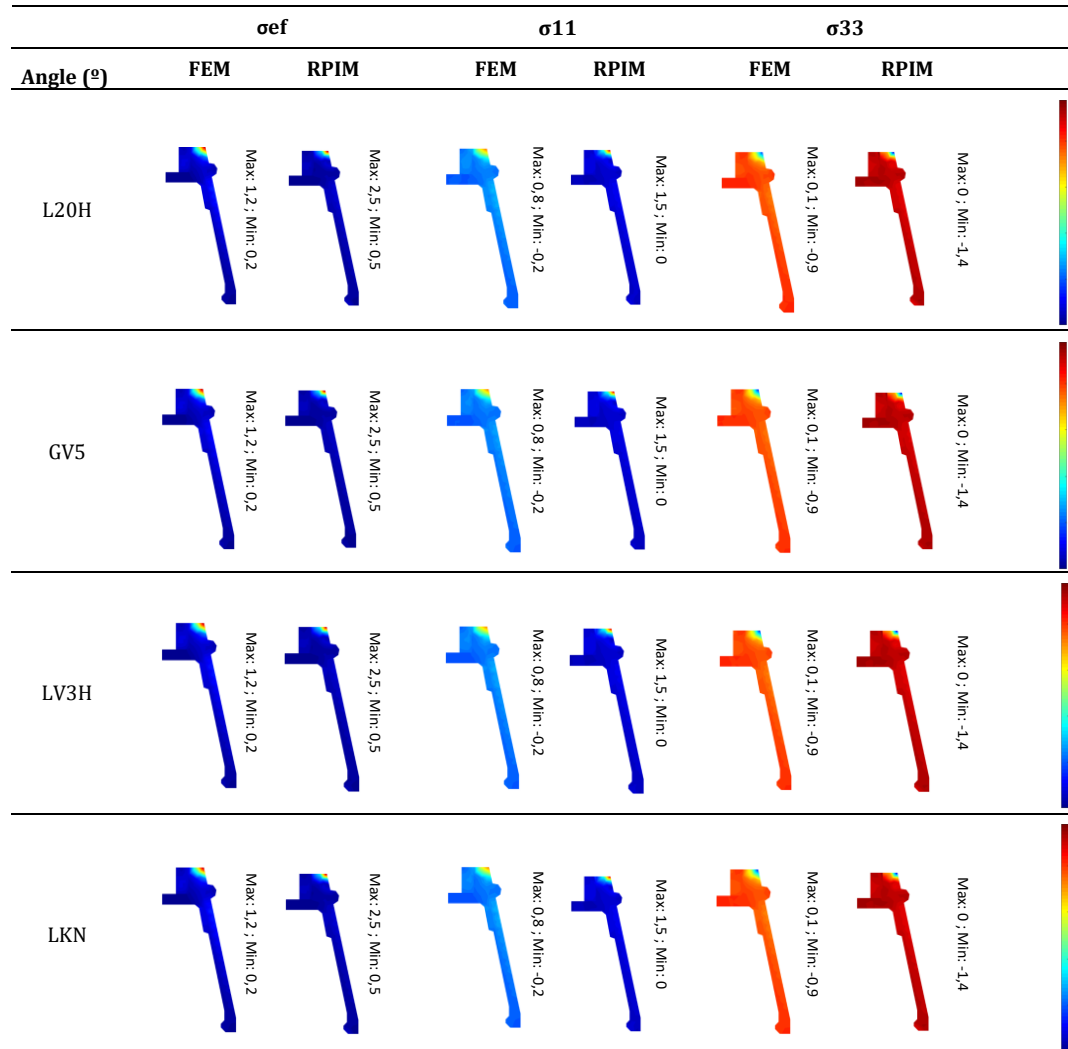
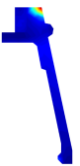

























Table 60: Strain distribution map on titanium sleeve for MCD regarding the distinct nylon materials. Effective strain (Von Mises), principal strain ϵ_{11} and principal strain ϵ_{33} , respectively

Angle (°)	ϵ_{ef}		ϵ_{11}		ϵ_{33}	
	FEM	RPIM	FEM	RPIM	FEM	RPIM
L20H	 Max: $9E-6$; Min: $1E-6$	 Max: $18E-6$; Min: $2E-6$	 Max: $14E-6$; Min: $2E-6$	 Max: $16E-6$; Min: $2E-6$	 Max: $-2E-6$; Min: $-14E-6$	 Max: $-2E-6$; Min: $-16E-6$
GV5	 Max: $9E-6$; Min: $1E-6$	 Max: $18E-6$; Min: $2E-6$	 Max: $8E-6$; Min: $1E-6$	 Max: $16E-6$; Min: $2E-6$	 Max: $-1E-6$; Min: $-8E-6$	 Max: $-2E-6$; Min: $-16E-7$
LV3H	 Max: $9E-6$; Min: $1E-6$	 Max: $18E-6$; Min: $2E-6$	 Max: $8E-6$; Min: $1E-6$	 Max: $16E-6$; Min: $2E-6$	 Max: $-1E-6$; Min: $-8E-6$	 Max: $-2E-6$; Min: $-16E-6$
LKN	 Max: $9E-6$; Min: $1E-6$	 Max: $18E-6$; Min: $2E-6$	 Max: $8E-6$; Min: $1E-6$	 Max: $16E-6$; Min: $2E-6$	 Max: $-1E-6$; Min: $-8E-6$	 Max: $-2E-6$; Min: $-16E-6$

7. Conclusions

7.1 Conclusions

The difference between the stress values obtained with the FEM and the meshless method can be explained with the low density of the discretization mesh.

Since no convergence test was performed in this work, no conclusions can be made regarding the best solution. However, the literature shows that meshless methods converge faster than the FEM, specially for tetrahedral element.

Notice that, due to hardware limitations, the computation is limited to a maximum number of 10000 nodes for 3D analyses, hindering further analysis using denser nodal discretisation.

The influence domain concept smooth the material properties of near nodes on the interface between distinct materials, such as the titanium/nylon interface. This undesirable effect leads to errors in the stress/strain fields on those interfaces.

Despite the impossibility to actually compare directly the RPIM and FEM results, the experience acquired with this work allows to affirm that meshless methods are useful tools to analyse complex biomechanical problems, allowing to discretize directly the problem domain from the CT images and to set automatically the material properties to each node. Nevertheless, these meshless techniques require much more computational power than FEM, therefore, its massive use is dependent on the technological evolution.

For all the points in all the mechanical analyses, the differences for both numerical studies were comprehended in general between 10% - 40%. The differences increased in all cases with the points which are closer to the zones where the boundary conditions are applied.

Regarding the materials applied in the dental implant for all the three parts, for the abutment and the titanium sleeve, the commercial titanium used will not cause any problem because titanium is capable to withstand the stresses produced by the loads applied. However, for the nylon sleeve, the stress values obtained for the considered loads were very close to the yield stresses of this material.

Nonetheless, there were a few barriers during the realization of the thesis, which are now enumerated:

- There was no full access to all the design drawings. Thus, as a simplification, the nylon sleeve was considered the space between the titanium sleeve and the abutment, although that does not actually correspond to the reality.
- Due to the computer performance and the non-commercial software (FEMAS) used (which is limited compared to other commercial software for numerical analysis), the number of nodes was 9202 which is a very low number to perform an adequate 3D analysis.
- The surrounding bone tissue was not considered. Therefore, the results obtained in this work are very conservative, because the boundary conditions simulating the bone tissue are much stiffer than the bone tissue itself. This simplification led to higher stresses near the essential boundary conditions.

7.2 Future works

For future works, it would be interesting to performance and test new kinds of approaches, such as:

- Perform all the same analysis, but for an inclined abutment;
- Compare the results obtained with similar ones obtained with experimental tests;
- Besides the FEM and RPIM, do all the analyses for the NNRPIM and then compare all the different numerical methods;
- Analyze the bone remodeling induced by the dental implant;
- Perform an elasto-plastic analysis (titanium and bone);
- Besides the different nylon materials used for the nylon sleeve, change the material for the abutment and the other sleeve using another type of titanium or other proper material;
- Analyze bar implants.

7.3 Computacional time

The computational time on average for each analysis is represented in the Figure 35.

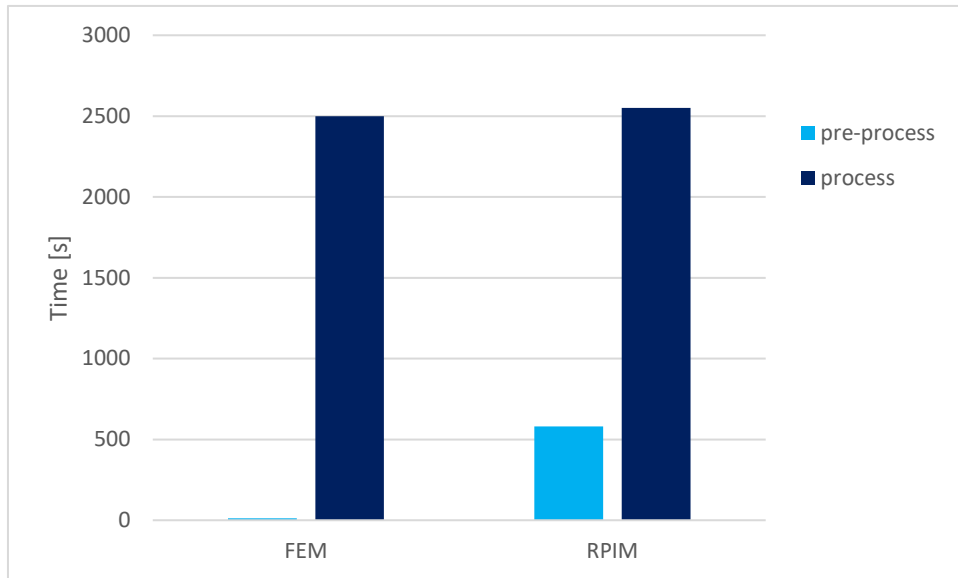


Figure 35: Computational time for both phase (pre-process and process) for each analysis

As it is possible to observe, due to the pre-processing phase, the computational time of the RPIM formulation is significantly higher than the computational cost of the FEM formulation. Although, it is known that if a coarser mesh had been used, this computational time would be lower for both FEM and RPIM.

For this thesis, it was performed 56 different analysis, distributed equally for FEM and RPIM. In total, around 60 hours of simulations were needed to have the results. Plus, the time required to obtain all the 1065 images for all the stress and strain maps which was on average 3 minutes per each.

8. References

1. Gobbo, P., *Dispositivo para a instalação de próteses dentárias suportadas por implantes*, UFP, Editor. 2017.
2. Dan Nitoi, S.M., Zoia Apostolescu, Andrei Dimitrescu, Oana Chivu, Marius Cornel Teodorescu *FEM of an implant Behaviour in a Healthy Bone*. Procedia Engineering, 2014.
3. H. M. S. Duarte, J.R.A., L. M. J. S. Dinis, R. M. Natal Jorge, J. Belinha *Numerical analysis of dental implants using a new advanced discretization technique*. Mechanics of Advanced Materials and Structures, 2015.
4. M. Doblaré, E.C., M. Calvo, M. A. Martínez, J. M. Garcia, J. Cegonino *On the employ of meshless methods in biomechanics*. Computer methods in applied mechanics and engineering, 2005.
5. Belinha, J., *Meshless Methods in Biomechanics: Bone Tissue Remodelling Analysis*. Vol. 16. 2014: Springer.
6. Belinha, J., *Meshless Methods: The Future of Computational Biomechanical Simulation*. Journal of Biometrics and Biostatistics, 2016.
7. R. C. Van Staden, H.G., Y. C. Loo, *Application of finite element method in dental implant research*. School of Engineering, Griffith University Gold Coast Campus, Australia.
8. Onate, E., *Structural Analysis with the Finite Element Method: Linear Statics*. Vol. 1. Springer.
9. Lai, S.A.V.H.C., *Overview of Meshless Methods*.
10. Gingold, R.A. and J.J. Monaghan, *Smoothed particle hydrodynamics: theory and application to non-spherical stars*. Monthly notices of the royal astronomical society, 1977. **181**(3): p. 375-389.
11. Libersky, L. and A. Petschek, *Smooth particle hydrodynamics with strength of materials*. Advances in the free-Lagrange method including contributions on adaptive gridding and the smooth particle hydrodynamics method, 1991: p. 248-257.
12. Belytschko, T., Y.Y. Lu, and L. Gu, *Element-free Galerkin methods*. International journal for numerical methods in engineering, 1994. **37**(2): p. 229-256.
13. Lancaster, P. and K. Salkauskas, *Surfaces generated by moving least squares methods*. Mathematics of computation, 1981. **37**(155): p. 141-158.
14. Nayroles, B., G. Touzot, and P. Villon, *Generalizing the finite element method: diffuse approximation and diffuse elements*. Computational mechanics, 1992. **10**(5): p. 307-318.
15. Fasshauer, G.E., *Meshfree Methods*.
16. Liu, W.K., et al., *Reproducing kernel particle methods for structural dynamics*. International Journal for Numerical Methods in Engineering, 1995. **38**(10): p. 1655-1679.
17. Atluri, S.N. and T. Zhu, *A new meshless local Petrov-Galerkin (MLPG) approach in computational mechanics*. Computational mechanics, 1998. **22**(2): p. 117-127.
18. Vinh Phu Nguyen, T.R., Stéphane Bordas, Marc Duflot, *Meshless methods: A review and computer implementation aspects*. Mathematics and Computers in Simulation, 2008.

19. Liu, G.-R. and Y. Gu, *A point interpolation method for two-dimensional solids*. International Journal for Numerical Methods in Engineering, 2001. **50**(4): p. 937-951.
20. Wang, J., G. Liu, and Y. Wu, *A point interpolation method for simulating dissipation process of consolidation*. Computer Methods in Applied Mechanics and Engineering, 2001. **190**(45): p. 5907-5922.
21. Wang, J. and G. Liu, *A point interpolation meshless method based on radial basis functions*. International Journal for Numerical Methods in Engineering, 2002. **54**(11): p. 1623-1648.
22. Wang, J. and G. Liu, *On the optimal shape parameters of radial basis functions used for 2-D meshless methods*. Computer methods in applied mechanics and engineering, 2002. **191**(23): p. 2611-2630.
23. Belinha, J.A.O.P., *The natural neighbour radial point interpolation method: solid mechanics and mechanobiology applications*. 2012.
24. Wong, K.C., et al., *Meshfree implementation of individualized active cardiac dynamics*. Computerized Medical Imaging and Graphics, 2010. **34**(1): p. 91-103.
25. Chen, T., et al., *Object-constrained meshless deformable algorithm for high speed 3D nonrigid registration between CT and CBCT*. Medical physics, 2010. **37**(1): p. 197-210.
26. Chen, G., et al., *A new approach for assigning bone material properties from CT images into finite element models*. Journal of biomechanics, 2010. **43**(5): p. 1011-1015.
27. Piqueiro, L., *A 2D Stress Analysis of Zirconia Dental Implants: a comparison study*. 2016, FEUP.
28. Cerrolaza, M., *Computational bioengineering: Current trends and applications*. 2004: World Scientific.
29. P. Bicudo, J.R., A. M. Deus, L. Reis, M. F. Vaz *Performance evaluation of dental implants: An experimental and numerical simulation study*. Theoretical and Applied Fracture Mechanics, 2016.
30. Hemmings, K. and Z. Harrington, *Replacement of missing teeth with fixed prostheses*. DENTAL UPDATE-LONDON-, 2004. **31**(3): p. 137-141.
31. Palmer, R., *Introduction to dental implants*. 1999: Brithish Dental Journal.
32. Gulsahi, A., *Bone quality assessment for dental implants*. 2011: INTECH Open Access Publisher.
33. Catherine, D., et al., *A dentist's guide to implantology, The Association of Dental Implantology, 2012*.
34. Babbush, C.A., et al., *Dental implants: the art and science*. 2010: Elsevier Health Sciences.
35. Abraham, C.M. *A Brief Historical Perspective on Dental Implants, Their Surface Coatings and Treatments*. The Open Dentistry Journal, 2014.
36. Sonick, M., *Implant Dentistry: Evolution and Current Trend - The Times They are A-Changin'*. 2006.
37. Rajan Rajput, Z.C., Monica Sindhu, Sowmya, Sundararajan, Ravi Raj Singh Chouhan *A Brief Chronological Review of Dental Implant History*.
38. P. Bicudo, J.R., A. M. Deus, L. Reis, M. F. Vaz *Mechanical behaviour of dental implants*. 2016.
39. Pye, A., et al., *A review of dental implants and infection*. Journal of Hospital infection, 2009. **72**(2): p. 104-110.

40. Zitzmann, N.U., E. Hagmann, and R. Weiger, *What is the prevalence of various types of prosthetic dental restorations in Europe?* Clinical Oral Implants Research, 2007. **18**(s3): p. 20-33.
41. Joel Ferreira Santiago Junior, E.P.P., Fellippo Ramos verri, Paulo Sérgio Perri de Carvalho *Stress analysis in bone tissue around single implants with different diameters and veneering materials: a 3-D finite element study.* Materials Science and Engineering C, 2013.
42. Luigi Baggi, I.C., Franco Maceri, Giuseppe Vairo *Stress-based performance evaluation of osseointegrated dental implants by finite-element simulation.* Simulation Modelling Practice and Theory, 2008.
43. F.J. de Cos Juez, F.S.L., P.J Garcia Nieto, A. Alvarez-Arenal *Non-linear numerical analysis of a double- threaded titanium alloy dental by FEM.* Applied Mathematics and Computation, 2008.
44. F. Lofaj, J.K., D. Németh, L. Kvetková *Finite element analysis of stress distributions in mono- and bi-cortical dental implants.* Materials Science and Engineering C, 2015.
45. Hardy, R.L., *Theory and applications of the multiquadric-biharmonic method 20 years of discovery 1968–1988.* Computers & Mathematics with Applications, 1990. **19**(8-9): p. 163-208.
46. Liu, G., *A point assembly method for stress analysis for two-dimensional solids.* International journal of solids and structures, 2002. **39**(1): p. 261-276.
47. Moreira, S.F., *Elastoplastic analysis using the Natural Neighbour Radial Point Interpolation Method.* 2013.
48. Timoshenko, S., *Strength of Materials.* Vol. Elementary Theory and Problems. 1930.
49. Gomes, J.S., *Mecânica dos sólidos e Resistência dos materiais.* 2004.
50. G. R. Liu, S.S.Q., *The Finite Element Method: A Practical Course.* 2 ed. 2013.
51. Reddy, J.N., *An introduction to the finite element method.* Vol. 2. 1993: McGraw-Hill New York.
52. Belinha, J., *Manual for FEMAS M-15.1.*
53. Noronha, J.P., *The Numerical Analysis of Airplane Windshields due to Bird Strike: A Static Study.* 2016, FEUP.